Impact of Disease-associated Missense Mutations on Protein Interaction Networks in Ciliopathies

Dissertation

der Mathematisch-Naturwissenschaftlichen Fakultät

der Eberhard Karls Universität Tübingen

zur Erlangung des Grades eines

Doktors der Naturwissenschaften

(Dr. rer. nat.)

vorgelegt von

Tobias Leonhard

aus Stuttgart

Tübingen

2023

Gedruckt mit Genehmigung der Mathematisch-Naturwissenschaftlichen Fakultät der Eberhard Karls Universität Tübingen.

Tag der mündlichen Qualifikation:	23.05.2023
Dekan:	Prof. Dr. Thilo Stehle
1. Berichterstatter:	Prof. Dr. Dirk Schwarzer
2. Berichterstatter:	Prof. Dr. Marius Ueffing

Danksagungen

Mein Dank gilt an erster Stelle Herrn Prof. Dr.rer.nat. Marius Ueffing, für die Möglichkeit meine Doktorarbeit in seiner Arbeitsgruppe anzufertigen.

Mein besonderer Dank gilt Dr rer.nat. Tina Beyer und Dr.rer.nat. Karsten Boldt für die Unterstützung und Betreuung im Rahmen meiner Arbeit.

Herrn Prof. Dr.rer.nat. Dirk Schwarzer danke ich, dass er sich als Betreuer und Begutachter zur Verfügung gestellt hat.

Felix Hoffmann, Isabel Stehle, Franzi Wörz, Shibu Anthony und Tobias Meisinger danke ich für die gegenseitige Unterstützung und den regen wissenschaftlichen Austausch in den letzten Jahren.

Des Weiteren danke ich allen weiteren Mitgliedern der AG Ueffing, für ihre Unterstützung in den vergangenen Jahren, die vielen gemeinsamen Erlebnisse und die angenehme Arbeitsatmosphäre.

Weiterhin danke ich meiner Mutter Angelika für ihre fortwährende Unterstützung während meines Studiums.

Meinen Freunden danke ich für die Unterstützungen und den privaten Ausgleich insbesondere in den Jahren während der Doktorarbeit.

Vielen Dank Euch allen!

Table of content

List of figures

List of tables

Abbreviations

A	Absorption
ACN	Acetonitrile
AMP	Adenosine 5‘-monophosphate
AP	Affinity purification
APS	Ammonium persulfate
ARPE	A retinal pigment epithelium
ATP	Adenosine 5‘-triphosphate
BBS	Bardet Biedl Syndrome
bp	Base pair
BSA	Bovine serum albumin
Cas9	CRISPR associated protein 9
CMV	Cytomegalovirus
CRISPR	Clustered regularly interspaced palindromic repeats
Da	Dalton
DNA	Desoxyribonucleic acid
ddH_20	Ultra-pure water
dH_2O	Deionized water
DMEM	Dulbecco’s modified Eagle medium
DMSO	Dimethylsulfoxid
DTT	Dithioreitol
***E**.coli*	*Escherichia coli*
e.g.	For example
ECL	Enhanced chemoluminescence
EDTA	Ethylendiaminetetraacetic acid
EtOH	Ethanol
FBS	Fetal bovine serum
FDR	False discovery rate
HCD	Higher energy collision induced dissociation
HEK293	Human embryonic kidney 293 cells
HEPES	N-(2-hydroxyethyl)piperazin-N‘-(2-ethansulfonicacid)
HPLC	High-performance liquid chromatography
HRP	Horseradish peroxidase
hTERT	Human telomerase reverse transcriptase

IAA	2-iodacetamide
IFT	Intraflagellar transport
IFT-A	Intraflagellar transport complex A
IFT-B	Intraflagellar transport complex B
IgG	Immunoglobulin G
IP	Immunoprecipitation
kb	Kilobase
kDa	Kilodalton
KO	Knockout
LB	Luria-Bertani
LC	Liquid chromatography
LCA	Leber congenital amaurosis
LC-MS/MS	Liquid chromatography-tandem mass spectrometry
LFQ	Label free quantification
M	Molarity
m/z	Mass to charge ratio
MeOH	Methanol
min	Minute
MS	Mass spectrometry
MS/MS	Tandem mass spectrometry
NaCl	Sodium chloride
NP-40	Nonident P-40
p	Value of probability
PAGE	Polyacrylamide gel electrophoresis
PBS	Phosphate-buffered saline
PEI	Polyethylenimine
PFA	Paraformaldehyde
PVDF	Polyvinylidene difluoride
RPE	Retinal pigment epithelium
rpm	Round per minute
RT	Room temperature
SDS	Sodium dodecyl sulfate
S.O.C.	Super Optimal Broth with glucose
StageTips	Stop-and-go extraction tips
TBS	Tris-buffered saline
TBST	Tris-buffered saline Tween
TEMED	N,N,N‘,N‘-tetramethylethylene-diamine
TFA	Trifluoroacetic acid

Tris	Tris(hydroxymethl)aminomethane
v/v	Volume per volume
w/v	Weight per volume
WB	Western blot
WT	Wildtype
ε	Decadic extinction coefficient

Summary

Cilia are antenna-shaped organelles protruding from the cellular surface of most eukaryotic cells [1–3]. They are highly conserved through evolution not only in vertebrates but also e.g. in *chlamydomonas*. They can be subdivided into two main groups: primary cilia, which are commonly immotile and serve as signaling hubs, and secondary (motile) cilia, e.g. in the respiratory epithelial cells, which facilitate the movement of extracellular fluid [1,4–8]. They consist of five main components, which serve different functional purposes. The basal body is formed by the centrosome in the S phase of the cell cycle. It is the nucleation point for the axoneme, a microtubule structure along the cilium, which serves as tracks for transport of cargo such as proteins within the cilium. At the base of the axoneme Y-shaped transition fibers form the ciliary gate, which serves as a diffusion barrier that restricts the entry of biomolecules and enables the distinct lipid and protein composition of the cilium [9,10]. Since cilia are biosynthetically inactive, all proteins and lipids have to be targeted to the cilium and actively transported along the axoneme. This so called intraflagellar transport (IFT) occurs bidirectional along the axoneme and is facilitated by motor proteins in conjunction with large protein complexes, which serve as binding hubs for cargo. Transport in anterograde direction is achieved by kinesin-2 in combination with the IFT-B protein complex. The retrograde transport of cargo in the opposite direction towards the ciliary base is facilitated by dynein-2 and the IFT-A protein complex [2,11,12]. At the distal end of the cilium the ciliary tip is located, where the transported cargo is used for elongation and disassembly of the axoneme. The cilium is surrounded by a lipid bilayer called the ciliary membrane, which shows a distinct lipid and protein composition and contains a variety of transmembrane receptors and ion channels [2,13,14]. Due to the important role of cilia in many cellular processes defects in genes coding for ciliary components are associated with a variety of severe diseases, which are commonly referred to as ciliopathies [5,7,13,15]. Since cilia serve many different functions depending on tissue and developmental stage, ciliopathies can vary widely in type and severity of the disease. The spectrum ranges from isolated retinal dystrophies to renal disease, liver fibrosis, cerebral anomalies, diabetes, infertility and skeletal defects [7,15–17]. Mutations in a single locus can be phenotypically heterogeneous, while at the same time mutations in different genes can lead to similar clinical manifestations [18,19]. So far more 35 ciliopathies have been reported, which often show similarities in the observed clinical phenotype [7,15].

The impact of disease-associated mutations on protein-protein interactions (PPIs) is not fully understood yet. One lead hypothesis is the concept of edgetic mutations, meaning that a mutation in a protein leads to the loss of specific interactions, represented by loss of an edge in a protein network, rather than a full loss of the protein, which would mean the loss of a node in the network [20–22]. In addition, it was hypothesized that missense mutations are hypomorph and have a quantitative effect on the native protein function. This would mean that they cause

loss of function to varying degree, which may influence type and severity of the disease. The study presented here investigated the effect of missense mutations in genes coding for components of the IFT-A complex on protein interaction networks. The main goal was to understand why mutations in a single gene lead to clinical defects that vary in type and severity as well as to assign pathogenic mechanisms to specific disease-related mutations [18,23–26].

To illuminate these questions missense mutations from previous publications were selected in four (IFT43, IFT121, IFT122 and IFT140) of the six components of the IFT-A protein complex. IFT-A mainly facilitates retrograde transport of cargo within the cilium, but also is required e.g. for the ciliary entry of several proteins [11,27,28]. Affinity purification in combination with LC-MS/MS analysis was used to investigate the protein interactome of the wildtype proteins as well as the changes induced by disease-associated missense mutations.

The generated data creates valuable new insights into the protein interactions of the wildtype forms of IFT43, IFT121, IFT122 and IFT140. The comparison of 37 mutants with the corresponding wildtype conditions revealed a variety of specific perturbations in protein interaction networks caused by the disease-associated missense mutations. In no case a total loss of all wildtype PPIs was observed. This further strengthens the concept of edgetic effects of disease-associated mutation via perturbation of specific PPIs (edges) in protein interaction networks.

In addition, the analysis of the mutants revealed quantitative effects on specific PPIs, causing loss of binding to interaction partners to a varying degree. In the work presented here, IFT140 represents the most convincing example to observe the quantitative effects of in total 24 analysed missense mutations. A subset of missense mutations reduced the abundance of IFT-A components to varying degree. This indicates a quantitative effect of these missense mutations on the integrity of the IFT-A protein complex, impairing its composition to a certain extent, that depends on the specific missense mutation.

To exclude stochastic and non-significant effects the alterations in PPIs induced by single nucleotide polymorphisms (SNP) were analysed. For IFT140 the effect of six SNPs leading to the exchange of a single amino acid was assessed analoguously to the analysis of the disease-associated missense mutations. Six SNPs were selected from the gnomAD database. They are located in all three domains of IFT140 and each SNP needed to show a high allele frequency and occur as homozygotes in at least one healthy individual. The analysis of the mass spectrometric data revealed that, in contrast to disease-associated missense mutations, the SNPs did not impair complex integrity of IFT-A. This further strengthens the disease-relevance of the previously observed perturbations in PPIs caused by ciliopathy-associated missense mutations.

Eight patients of our cohort affected by ciliopathies harbour missense mutations in IFT140 on both alleles for which mass spectrometric data was obtained. The extent to which each mutation disrupts IFT-A complex integrity, the allelic combination and the reported clinical features of each individual were analysed. This revealed a correlation between the severity of the clinical phenotype and the disruption of IFT-A complex integrity. While patients harbouring two undisruptive or mildly disruptive mutations on both alleles show milder phenotypes such as isolated retinal dystrophy, the inclusion of one disruptive mutation on one allele was associated with more severe forms of diseases. Patients harbouring two strongly disruptive mutations on both alleles showed the most severe clinical outcome, leading to systemic disease such as Mainzer Saldino and Jeune syndrome. This indicates a correlation between genotype and phenotype in the analysed patients and further strengthens the relevance of the quantitative effect on PPIs for clinical outcome.

To examine effects of different isoforms the protein-interaction networks of full length IFT140 and a shorter isoform, which is reported in human, were compared. This isoform is characterized by the loss of both of the N-terminal WD40 domains as well as parts of the TPR domain, which is important for mediating contact with the other components of the IFT-A protein complex [29,30]. However, the main part of the TPR domain is retained in this isoform. Affinity purification coupled with LC-MS/MS analysis revealed that the shorter isoform of IFT140 itself is not able to bind to all components of IFT-A. This makes it unlikely that the short isoform itself is able to ensure integrity of the IFT-A protein complex.

For functional analysis of IFT140 a CRISPR/Cas9-mediated knockout of IFT140 in hTERT-RPE1 cells was generated. Successful biallelic insertion of one bp in exon 4, leading to an early stop in the same exon, was confirmed via Sanger sequencing. Western blot analysis confirmed the loss of functional IFT140 on the protein level. Immunofluorescence microscopy of IFT140 and ARL13B, a primary cilia marker [31,32], in wildtype hTERT-RPE1 cells showed a co-localization of ARL13B and IFT140 at the primary cilium, which is consistent with previous publications [16,26,33]. In the IFT140 knockout cells both the ARL13B and the IFT140 specific signal were lost, further indicating successful knockout and the loss of functional IFT140.

The mass spectrometric analysis revealed the ciliary protein TULP3 as interactor of IFT140, that is affected by a subset of missense mutations in IFT140. TULP3 was reported to link the IFT-A complex to membrane-bound cargo [34–36] and the binding of TULP3 to IFT-A was lost in eight out of 12 mutants in IFT140 for which a quantification was possible. Since TULP3 was shown to be involved in the negative regulation of Sonic hedgehog signaling via the transmembrane receptor GPR161 [32,35–37], the effect of IFT140 on the hedgehog signaling pathway was examined using hTERT-RPE1 wildtype and IFT140 knockout cells. Consistent with our expectation real-time PCR revealed that the expression of the hedgehog target gene

GLI1 [5,38,39] is increased in IFT140 knockout cell as compared to the wildtype in absence of stimulation of the hedgehog signaling pathway. Due to the importance of hedgehog signaling in tissue development and homeostasis defects in this crucial pathway can lead to skeletal abnormalities and kidney disease among other effects [36–38,40]. This is consistent with some of the defects observed in ciliopathy-affected patients harbouring mutations in IFT140, hinting towards a potential disease mechanism in some of these patients. Since hedgehog signaling can be pharmacologically targeted this may create a rationale for future treatment.

Zusammenfassung

Zilien sind antennenartige Ausstülpungen auf der Oberfläche der meisten eukaryotischen Zellen [1–3]. Es handelt sich um evolutionäre hochkonservierte Organellen welche man nicht nur in *Vertebrata,* sondern beispielsweise auch in *Chlamydomonas* findet. Zilien unterteilen sich in zwei Hauptkategorien: primäre Zilien, die meist als Plattformen für Signalwege dienen, und sekundäre (bewegliche) Zilien, welche z.B. extrazelluläre Flüssigkeiten bewegen [1,4–8]. Sie bestehen aus fünf Hauptkomponenten mit verschiedenen Funktionen. Der Basalkörper wird vom Zentrosom in der S Phase des Zellzyklus gebildet. Er dient als Nukleationspunkt für das Axonem, eine aus Mikrotubuli bestehende Struktur im Zilium, die wie Schienen für den Transport von Biomolekülen wie Proteinen innerhalb des Ziliums dienen. An der Basis des Axonems bilden y-förmige Übergangsfasern eine Diffusionsbarriere. Dies ermöglicht dem Zilium eine spezifische Zusammensetzung an Proteinen und Lipiden zu erhalten, die sich vom Rest der Zelle unterscheidet [9,10]. Da Zilien keine Synthese von Biomolekülen betreiben, müssen sämtliche Proteine und Lipide zielgerichtet zum Zilium gebracht und aktiv entlang des Axonems transportiert werden. Dieser sogenannte intraflagellare Transport (IFT) ist bidirektional und erfolgt mit Hilfe von Motorproteine in Verbindung mit Proteinkomplexen, welche als Bindungsstellen für zu transportierende Ladung dienen. Der Transport in anterograder Richtung wird durch Kinesin-2 in Verbindung mit dem IFT-B Proteinkomplex ermöglicht. Der Transport in die entgegengesetzte Richtung hingegen wird durch Dynein-2 und IFT-A bewerkstelligt [2,11,12]. Am distalen Ende des Ziliums wird die transportierte Ladung genutzt um das Axonem zu verlängern oder abzubauen. Das Zilium ist von einer Lipidmembran umgeben. Diese ziliäre Membran hat eine andere Lipidzusammensetzung als die Plasmamembran und enthält eine große Anzahl an Transmembranrezeptoren und Ionenkanälen [2,13,14].

Aufgrund der zentralen Rolle von Zilien in einer Vielzahl von zellulären Prozessen können Defekte in ziliären Proteinen zu einer Vielzahl von Krankheiten führen, welche als Ziliopathien bezeichnet werden [5,7,13,15]. Da Zilien verschiedene Funktionen in Abhängigkeit des Gewebes- und Entwicklungsstandes haben handelt es sich bei Ziliopathien um eine äußerst heterogene Gruppe an Krankheiten. Sie reicht von isolierten Retinadystophien über Nierenerkrankungen, Leberfibrose, Diabetes, Infertilität bis zu skelettalen Defekten [7,15–17]. Mutationen in einem einzelnen genetischen Lokus können phänotypisch heterogen sein, während Mutationen in verschiedenen Genen zu ähnlichen klinischen Erscheinungen führen können [18,19]. Bisher wurden 35 Ziliopathien in der Literatur beschrieben, welche häufig eine teilweise Überlappung in der klinischen Ausprägung zeigen [7,15].

Der Effekt von krankeitsassoziierten Mutationen auf Protein-Interaktionsnetzwerke ist noch nicht vollständig verstanden. Eine der führenden Theorien ist das Konzept von edgetic-

Mutationen. Dieses beschreibt die Idee, dass Mutationen in einem Protein zum Verlust einer spezifischen Interaktion führen, was in einem Interaktionsnetzwerk den Verlust einer Verbindung (edge) verursachen würde. Das Gegenstück hierzu wäre ein kompletter Funktionsverlust des Proteins, was den Verlust des Knotens im Netzwerk bedeuten würde [20–22]. Außerdem wurde die Hypothese aufgestellt, dass Missense-Mutationen hypomorph sind und die Proteinfunktion nur in einem gewissen Umfang beeinträchtigen. Dies könnte auch die Art und Schwere der Erkrankung beeinflussen. Die vorliegende Arbeit untersucht den Effekt von Missense-Mutationen auf die Proteininteraktionen von IFT-A Proteinen. Das Hauptziel war ein besseres Verständnis der Gründe weshalb Mutationen in einem spezifischen Gen zu klinischen Effekten führen, die sich in Art und Ausprägung stark voneinander unterscheiden [18,23–26]. Außerdem sollten einzelnen Mutationen spezifische pathogene Mechanismen zugeordnet werden.

Um diese Fragen zu beantworten wurden Missense-Mutationen aus früheren Publikationen in vier von sechs Komponenten des IFT-A Komplexes ausgewählt (IFT43, IFT121, IFT122 und IFT140), welcher hauptsächlich am retrograden Transport im Zilium beteiligt ist [11,27,28]. Eine Affinitätsaufreinigung in Kombination mit einer massenspektrometrischen Analyse und einer labelfree-Quantifizierung wurde durchgeführt. Durch die statistische Auswertung von mindestens sechs biologischen Replikaten wurde ein robuster Datensatz gewonnen. Die erhaltenen Daten eröffnen interessante neue Einsichten in die Proteininteraktionen der Wildtyp-Formen von IFT43, IFT121, IFT122 und IFT140. Der Vergleich der insgesamt 37 Mutanten mit dem jeweiligen Wildtyp offenbarte ein breites Spektrum an Störungen spezifischer Proteininteraktionen, die durch krankheitsassoziierte Missense-Mutationen verursacht werden. In keinem Fall wurde ein kompletter Verlust sämtlicher Proteininteraktionen des Wildtyps beobachtet. Diese Erkenntnisse untermauern das Konzept von edgetic-Effekten auf spezifische Protein-Interaktionen durch Mutationen.

Bei der Analyse zeigten sich außerdem quantitative Effekte von einigen Mutanten aus spezifische Proteininteraktionen. Diese führten zum Verlust der Bindung einzelner Proteine in einem begrenzten Umfang, der sich zwischen verschiedenen Mutanten unterscheidet. Am deutlichsten wurde dies im Fall von IFT140, wo insgesamt 24 krankheitsassoziierte Missense-Mutationen untersucht wurden. Eine Gruppe von Mutationen reduzierte den Level von IFT-A Komponenten in verschiedenem Ausmaß. Dies deutet auf einen quantitativen Effekt auf die Integrität des IFT-A Proteinkomplexes in Abhängigkeit von der jeweiligen Mutation hin.

Um stochastische und nicht signifikante Effekte auszuschließen wurde der Effekt von single nucleotide Polymorphismen (SNPs) auf Proteininteraktionen untersucht. Für IFT140 wurden sechs SNPs untersucht, die zum Austausch einer einzelnen Aminosäure führen. Analog zu den krankheitsassoziierten Missense-Mutationen wurden die Proteininteraktionen untersucht.

Die analysierten SNPs in IFT140 wurden über die gnomAD Datenbank gesucht. Es wurden SNPs aus allen drei Domänen von IFT140 ausgewählt die mit hoher Allelfrequenz auftreten und in mindestens einem gesunden Individuum homozygote auftreten. Die Analyse der massenspektrometrischen Daten zeigt, dass die untersuchten SNPs im Unterscheid zu einigen krankheitsassoziierten Missense-Mutatonen keinen Einfluss auf die Integrität des IFT-A Komplexes haben. Dies unterstützt die Hypothese, dass die durch krankheitsassoziierte Missense-Mutationen verursachten Störungen von Proteininteraktionen relevant für den beobachteten klinischen Phänotyp sind.

Acht Patienten unserer Kohorte mit Ziliopathien verursacht durch Mutationen in IFT140 haben auf beiden Allelen Missense-Mutationen, für die im Rahmen dieser Studie massenspektrometrische Daten erhoben wurden. Der Einfluss des disruptiven Effekts auf die Integrität des IFT-A Komplexes wurde für jede dieser Mutationen untersucht und mit der allelischen Kombination und dem klinischen Phänotyp der jeweiligen Patienten verglichen. Patienten mit zwei Mutationen ohne oder mit mildem Effekt auf die Integrität des IFT-A Komplexes zeigen in Relation mildere klinische Phänotypen, z.B. isolierte Dystrophie der Retina. In Fällen mit einer stärker disruptiven Mutation auf einem Allel ist auch der beobachtete klinische Phänotyp schwerer. Die schwerwiegendsten klinischen Auswirkungen treten in Patienten auf, die stark disruptive Mutationen auf beiden Allelen ausweisen, z.B. Mainzer Saldino oder Jeune Syndrom. Diese Ergebnisse weisen auf eine Korrelation zwischen dem Genotyp und dem klinischen Phänotyp in den untersuchten Patienten hin und untermauern die Bedeutung der beobachteten quantitativen Effekte für die klinische Ausprägung.

Für IFT140 ist auch eine kürzere Isoform im Menschen bekannt. Dieser Isoform fehlen die N-terminalen WD40-Domänen sowie Teile der TPR Domäne, welche wichtig für den Kontakt mit den anderen Komponenten des IFT-A Komplexes ist [29,30]. Affinitätsaufreinigung in Verbindung mit massenspektrometrischer Analyse zeigte, dass die kürzere Isoform nicht in der Lage ist alle Komponenten des IFT-A Komplexes zu binden. Es ist daher unwahrscheinlich, dass die kurze Isoform allein die Integrität des IFT-A Komplexes sicherstellen kann.

Für die funktionelle Analyse von IFT140 wurde ein Knockout von IFT140 in hTERT-RPE1 Zellen unter Nutzung des CRISPR/Cas9-Systems generiert. Die erfolgreiche biallelische Insertion von einem Basenpaar in Exon 4 wurde durch Sequenzierung bestätigt. Diese Insertion führt zu einem frühen Stoppcodon im selben Exon. Eine Analyse mittels Western Blot bestätigte den Verlust von IFT140 auf Proteinebene. Immunofluoreszenz-Mikroskopie von IFT140 und ARL13B, einem Marker für primäre Zilien [31,32], in Wildtyp hTERT-RPE1 Zellen zeigte eine Ko-Lokalisation von ARL13B und IFT140, welche bereits früher beobachtet wurde [16,26,33]. In den IFT140 Knockout-Zellen war weder ein spezifisches Signal für ARL13B noch für IFT140 sichtbar. Dies ist ein weiterer Hinweis für den erfolgreichen Knockout von IFT140.

In der massenspektrometrischen Analyse zeigte sich, dass das ziliäre Protein TULP3 ein Interaktionspartner von IFT140 ist, dessen Bindung durch einen Teil der Missense-Mutationen in IFT140 beeinträchtigt wird. Frühere Publikationen berichten, dass TULP3 den IFT-A Komplex mit Ladung in der ziliären Membran verbindet [34–36]. Die Bindung von TULP3 ging in acht von 12 Mutanten in IFT140 für die eine Quantifizierung möglich war verloren. Da TULP3 an der negative Regulation des Sonic Hedgehog Signalweges mittels des Transmembranrezeptors GPR161 beteiligt ist [32,35–37] wurde der Effekt von IFT140 auf den Hedgehog Signalweg in hTERT-RPE1 Wildtyp und IFT140 Knockout-Zellen untersucht. In Übereinstimmung mit den Erwartungen zeigte eine Analyse mittels Real-Time PCR, dass die Expression des Hedgehog-Zielgens [5,38,39] *GLI1* in IFT140 Knockout-Zellen im Vergleich zum Wildtyp erhöht ist. Aufgrund der Bedeutung des Hedgehog-Signalwegs für die Entwicklung und den Erhalt von Gewebe können Defekte zu verschiedenen Krankheiten führen. Dazu gehören u.a. Missbildungen der Niere und der Knochen [36–38,40]. Diese Defekte stimmen überein mit einem Teil der beobachteten Krankheitsbilder in Patienten mit Ziliopathien, verursacht durch Mutationen in IFT140. Dies weist auf einen potenziellen Krankheitsmechanismus hin. Da der Hedgehog-Signalweg pharmakologisch beeinflusst werden kann könnte diese Erkenntnis eine Behandlungsoption für diese Patienten in der Zukunft ermöglichen.

Introduction

Cilia

Cilia are antenna-like structures protruding from the surface of most polarised eukaryotic cells [1–3]. It is an evolutionary highly conserved organelle found not only in vertebrates but also e.g. in *chlamydomonas* and has important functions in cellular sensing, signaling as well as motility [1,4,5]. Cilia can be distinguished into two main groups based on their structure and function: Primary cilia, which are usually immotile and have important signaling functions and Secondary (motile) cilia, which e.g. facilitate the movement of extracellular fluid [6–8].The proper function of cilia is crucial for a broad variety of cellular processes. This includes neurosensory functions such as vision and hearing, reproduction and tissue development and homeostasis. Primary cilia usually serve as signaling platforms e.g. for hedgehog signaling pathway among others. Secondary cilia are usually motile and are crucial for processes like mucus clearance or the propulsion of sperm [2,6,13,15].

Structure of cilia

Cilia protrude from the cellular surface and are surrounded by a lipid bilayer. The ciliary structure is defined by several main compartments, which are shared by primary and secondary cilia. The basal body originates from the mother centriole. It has a cylindrical shape and consists of nine microtubule triplets formed by γ-tubulin, which are arranged in a radial pattern [13,15]. It is the nucleation point for the axoneme, which is the starting point for trafficking of cargo along the cilium, serving as tracks for active transport [41–43]. The axoneme is formed by a set of nine microtubule heterodimers, consisting of α- and β-tubulin subunits forming a circular structure [3,7] In the case of secondary (motile) cilia the nine peripheral microtubule duplets are arranged in a circular pattern around a central pair of single microtubules [15,44,45]. The axoneme of secondary cilia exhibits auxiliary dynein arms and radial spokes, which enable the active movement of the motile cilium necessary e.g. for mucus clearance in epithelial cells, propulsion of sperm flagella or during embryonic development for left-right determination [9,46].

The transition zone consists of Y-shaped transition fibres and is located at the basal body [47]. It acts as selective barrier, regulating the entry and exit of proteins by limiting diffusion, ensuring the integrity of the distinct ciliary environment [3,10]. At the distal end of the cilium the ciliary tip is located, where transported cargo is used for assembly or disassembly of the cilium [10,43]. The ciliary membrane is the outer boundary of the cilium. While connected to the plasma membrane the ciliary membrane nevertheless has a distinct lipid and protein composition [14]. This includes transmembrane receptors as well as ion channels among others, which enables the cilium to fulfil its crucial role in sensory functions such as photo- or mechano-sensation and sensing of extracellular signals like Sonic hedgehog [3,5,9,14,48,49].

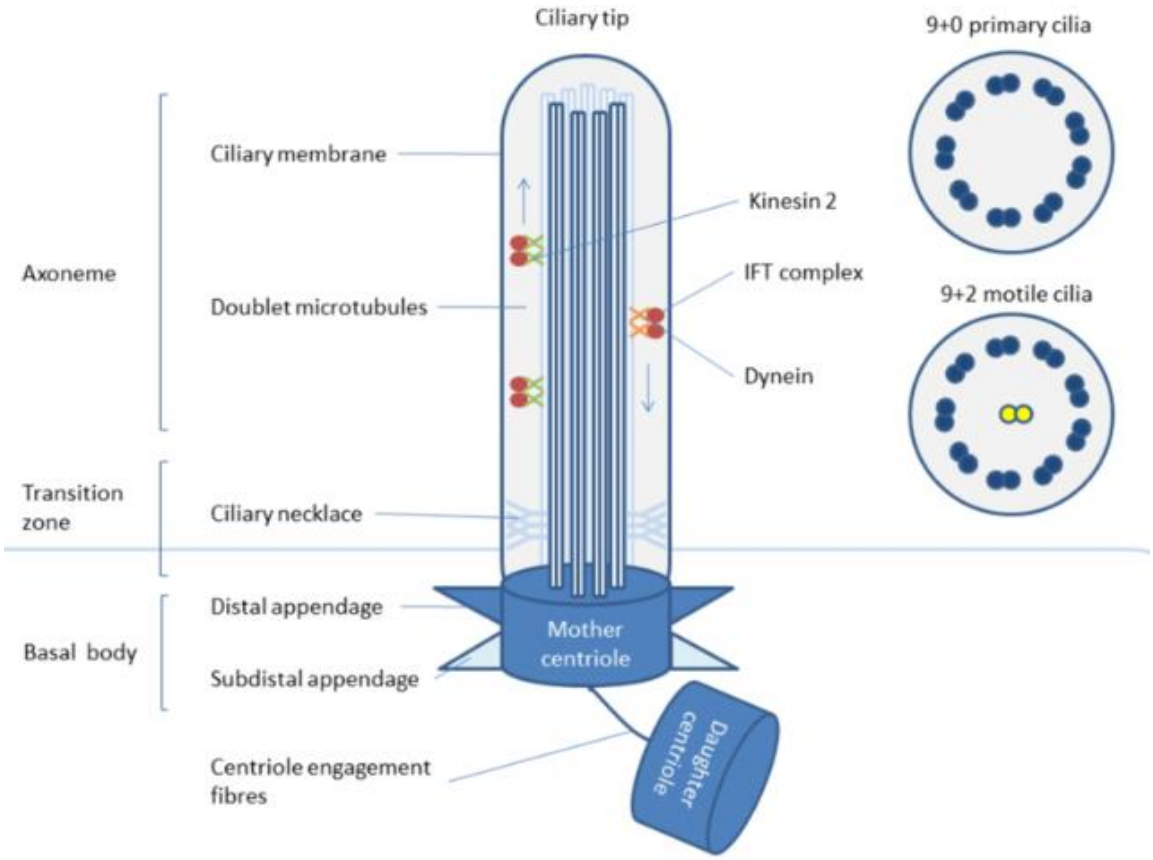

Figure 1: Structure of cilia. A schematic view of a cilium is shown. *The mother centriole forms the basal body, from which the ciliary axoneme arises. Along the axoneme cargo is actively transported in distal direction towards the ciliary tip and backwards to the basal body region. The transition fibres form the ciliary necklace, which acts as a selective barrier. The cilium is surrounded by the ciliary membrane The microtubule arrangement of the axoneme is shown for primary and motile cilia. Taken from* [50].

Retinal cilia

The vertebrate retina is a thin layer of neural tissue which converts light into an electrical stimulus, enabling vision through its light sensitive photoreceptor cells [51]. Photosensation is achieved by photoreceptor cells, specialised neuroepithelial cells present in the retina [52–54]. In the human retina two different types of photoreceptors are found: cones and rods [54,55]. Rods are extremely sensitive and can detect a single photon, facilitating light detection also in weak light conditions [56]. Cones require a stronger stimulus to generate an electrical output. In humans three different classes of cones are known, which react to different wavelengths, enabling colour vision [57]. Both rods and cones consist of an outer and an inner segment, which are linked by the connecting cilium. The outer segment is a modified sensory cilium originating from the basal body. It contains stacks of membrane discs containing rhodopsin, a chromophore, covalently bound to the transmembrane protein opsin [12,53,58]. The connecting cilium functions as a transition zone, connecting the metabolic active inner segment with the light sensitive outer segment [52,55,59]. All proteins necessary for the function and maintenance

of the outer segment need to be actively transported via the connecting cilium from the inner segment [60]. The high turnover of rhodopsin in the outer segment requires a high-throughput transport through the connecting cilium [51]. Defects in ciliary genes can lead to severe defects in tissue development and homeostasis that can lead to blindness [5,12,61].

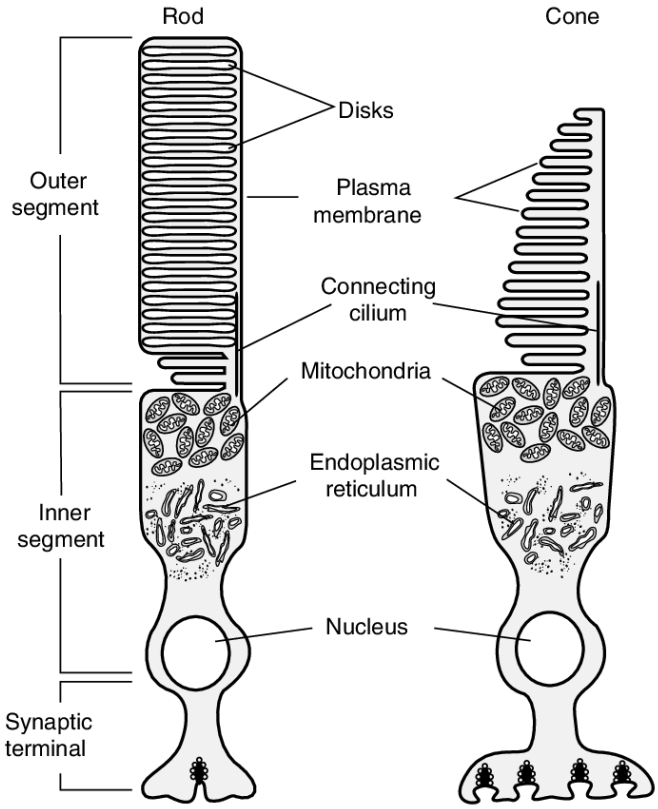

Figure 2: Structure of photoreceptor cells. *A schematic view of a rod (left) and cone (right) photoreceptor cell is shown. The outer segment contains the membrane disks in which rhodopsin facilitates light perception. It is linked to the biosynthetically active inner segment via the connecting cilium, along which cargo is actively transported between the two segments. Modified after* [62].

Ciliogenesis and cilia disassembly

Cilia are formed in a process called ciliogenesis. It is initiated by the migration of a mother centriole to the cellular surface and its attachment at the plasma membrane after fusion with a ciliary vesicle in the G_1 phase of the cell cycle [1,8,63]. Due to the necessity of a centriole tight coordination of cilia formation and cell cycle progression is crucial [2,64]. The basal body is anchored to the ciliary membrane at its distal point by the transition fibres and serves as the nucleation point for the axoneme [65,66]. Together they form the ciliary gate, a selective barrier that regulates entry of proteins and vesicles to the biosynthetically inactive cilium, enabling its discrete protein and lipid composition [10,44,65]. The transition fibres also serve as binding interface for intraflagellar transport (IFT) complexes, a specific bidirectional transport system for cargo within the cilium [42,67]. At the basal body the Bardet-Biedl Complex is located, an eight

protein complex which is crucial for targeting of proteins to cilia [42,68]. Tubulin-α and –β nucleation leads to the formation of the axoneme. Further elongation of the axoneme requires fusion of ciliary vesicles with secondary vesicles in order to generate the ciliary membrane [69,70]. In the G_0 phase the ciliary assembly and disassembly are balanced and the mature cilium is formed. Following re-entry of the cell cycle in the G_1 phase cilia start to disassemble.

In proliferating cells disassembly of cilia usually occurs before entering mitosis in the M phase, since the centrioles that form the basal body of the cilium are the same structures that are required to form the MTOC and spindle poles during mitosis [66,71,72]. The shortening of the cilium requires the depolymerisation of the axonemal microtubules as well as the reduction and retrieval of the ciliary membrane and the dissociation of protein complexes [27,44,66]. This requires several changes on the molecular level to enable cilia disassembly, including protein methylation and –ubiquitination as well as deacetylation of tubulin in a highly regulated process [1,66]. Ciliary disassembly is orchestrated by noncanonical Wnt5 signaling. Upon phosphorylation of DVL2, it forms a complex with PLK1, which subsequently stabilizes HEF1, an activator of Aurora kinas A [66,73,74]. Following its activation Aurora kinase A phosphorylates the histone-deacetylase HDAC6, which leads to the deacetylation of axonemal tubulin and the shortening of the cilium [27,72,75].

Intraflagellar transport

Cilia contain more than 500 distinct proteins, which are necessary for their proper function. Since cilia contain no machinery for protein synthesis of their own, cargo needs to be actively selected and transported into the cilium [2,45]. The precise mechanisms of targeting cargo to the cilium and its entry are not yet understood. Once cargo is selected and enters the cilium, the transport of proteins and membrane vesicles occurs along the microtubule axoneme and is called intraflagellar transport (IFT) [7,34,41,48]. It involves motor proteins as well as protein complexes, which enable specific cargo selection through several protein-protein interaction (PPI) motifs [11,12]. Functional IFT is crucial for the proper assembly and function of most eukaryotic cilia, such as the outer segments of photoreceptor rods and cones in the retina [6,7]. The broad variety of ciliary functions and the complex dynamics of ciliary assembly, maintenance and disassembly stresses the necessity of tight regulation of IFT.

Anterograde transport from the ciliary base to the tip region, e.g. of tubulin subunits for ciliary assembly and elongation, is driven by the heteromeric kinesin-II motor protein [30,67]. The contact to the cargo is mediated by a protein complex called IFT-B, which consist of 16 distinct proteins [1,12]. IFT-B can be further divided into a core and peripheral complex. The stable core complex is made up of nine distinct proteins (IFT22, -25, -27, -46, -52, -70, -74, -81 and -88) and is also called IFT-B1. It can be further distinguished into two subcomplexes and the interaction between both subcomplexes is mediated via the IFT74-IFT81 and the IFT46-IFT52

heterodimers. It interacts with the peripheral complex consisting of six proteins (IFT20, -38, -54, -57, -80 and -172) via the connecting tetramer consisting of IFT52 and -88 from the core complex and IFT38 and -57 from the peripheral complex [12,66,67,76]. IFT-B also mediates the contact to the BBSome, an eight protein complex that regulates recruitment and import of ciliary membrane proteins [68,76].

The contact between the IFT-A and IFT-B protein complexes is mainly mediated by the interaction between the IFT144-IFT122 heterodimer in IFT-A core complex and IFT-46, -52 and-88 in the IFT-B core [30,67,76]. It remains unknown why more than 20 distinct subunits are necessary to form both complexes, but the high degree of evolutionary conservation of the IFT particles in eukaryotic cells hints towards a critical role of each single component for the proper function of cilia.

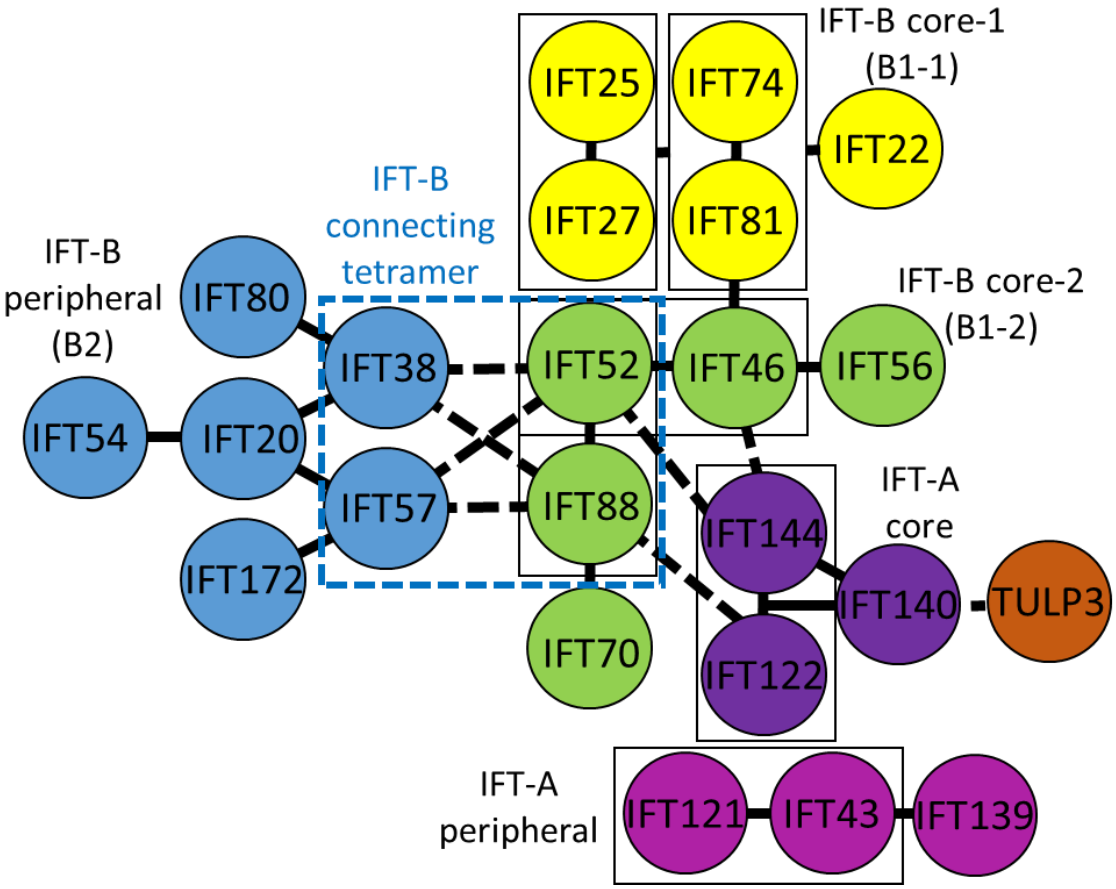

Figure 3: Structure of the IFT complexes and interplay between its components. *IFT-B consists of 16 components and can be subdivided into the IFT-B core-1 (IFT22, -25, -27, -74, -81) and the IFT-B core-2 (IFT46, -52, -56, -70, -80) as well as the IFT-B peripheral complex (IFT20, -38, -54, -57, 80, -172). The interaction between the IFT-B peripheral complex and the IFT-B core-2 is mediated by the IFT-B connecting tetramer consisting of IFT38 and -57 in the peripheral and IFT52 and -88 in the IFT-B core-2 complex. They are connected via the IFT-B core-2 to the IFT-A core complex (IFT122, -140, -144), which in turn interacts with the IFT-A peripheral complex (IFT43, -121, -139) and the protein TULP3. Modified after* [30].

Retrograde transport from the ciliary tip to the basal body, e.g. of turnover products and IFT-B or during ciliary disassembly, is achieved by active transport via dynein-2. Cargo contact is mediated by the IFT-A complex, which consists of six proteins [11,12,27,67]. The complex can be further distinguished into two subcomplexes, with IFT140, IFT122 and IFT144 forming a core complex, which is attached to a peripheral subcomplex consisting of IFT43, IFT121 and IFT139. The interaction between both subcomplexes is mediated via IFT122 in the core complex and IFT121 and IFT43 in the peripheral complex [30,35,76]. The contact between the components of the complex is mainly mediated by tetratricopeptide repeats (TPR) in several proteins of the IFT-A complex, while several WD40 domains serve as binding interface for interaction partners [29,30,34]. Due to the large size of some of the subunits and the sensitivity of the complex to stoichiometric changes, elucidating the precise role and function of several of these components has proven challenging in the past. IFT-A also has functions in the anterograde transport, e.g. by linking heterotrimeric kinesin to its corresponding IFT particle, which enables its transport from the ciliary base to the ciliary tip [34,77,78]. This also is the case for other ciliary proteins, such as TULP3 and the G-protein coupled receptors SSTR3 and MCHR1 [35].

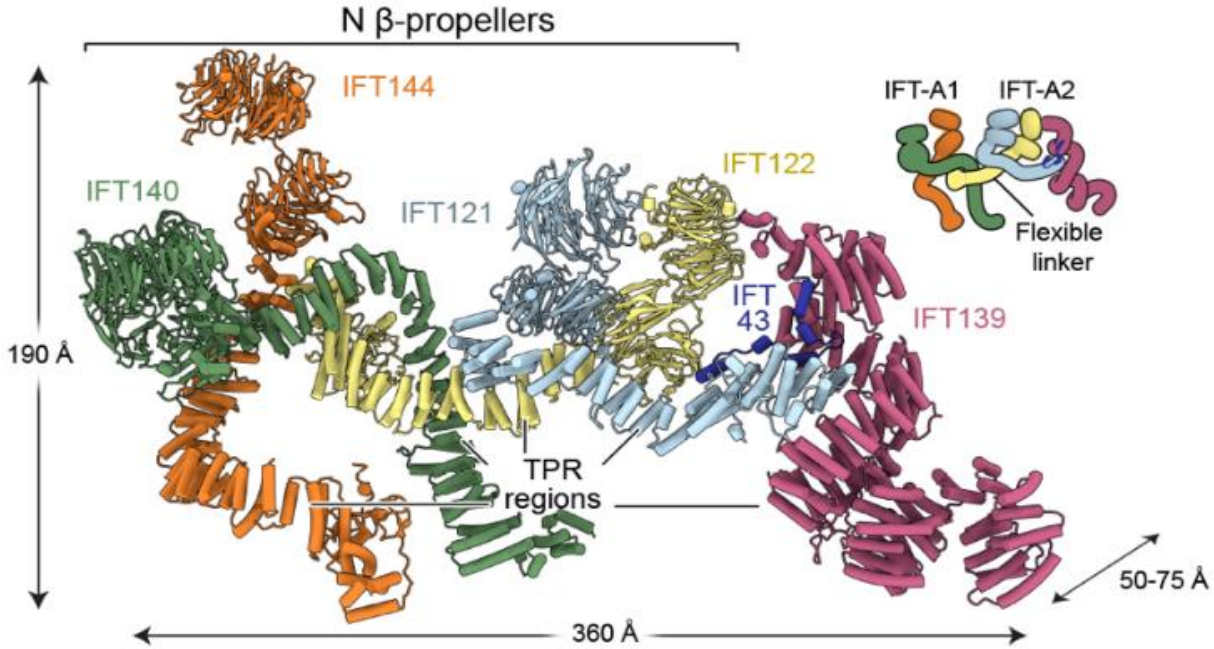

Figure 4: Structure of the IFT-A complex. *A structure prediction for all six components of IFT-A in the complex is shown. The core complex (IFT122, -140 and 144) on the left and the peripheral complex (IFT43, -121 and -139) on the right-hand side. IFT121, 122, 140 and 144 share a similar structure, with two N-terminal ß-propellers (WD40 domains) facing outward and serving as binding interfaces for other proteins. The TPR regions are facing inward and partially intertwind, mediating the contact between the different components of the complex. IFT139 and IFT43 consist of mainly α-helices. Taken from [29].*

Ciliary signaling

Primary cilia are major signaling hubs and crucial for the initiation and regulation of signaling pathways [9,79]. The ciliary membrane contains a high number of transmembrane receptors as well as ion channels, which enable the cell to sense signals from its extracellular environment. Among the receptors in the ciliary membrane are several G protein-coupled receptors important for signaling pathways such as TGF-β, Hippo, Notch, Wnt and Sonic hedgehog [2,8,13,24]. Sonic hedgehog is the best studied example in the cilia-dependent context. Hedgehog is a crucial pathway for tissue development and homeostasis, with defects leading to neural tube closure defects and skeletal anomalies among others [7,9,80].

In the hedgehog-unstimulated state the membrane-bound receptor Patched1 (PTCH1) inhibits the localization of Smoothened (SMO) to the ciliary membrane [31,39]. Within the cilium the IFT-A complex in combination with tubby-like protein 3 (TULP3) mediates the ciliary entry and transport of the transmembrane protein GPR161 [34,81,82]. In the ciliary membrane GPR161 activates the adenylate cyclase (AC), which in turn leads to the generation of cyclic-AMP (cAMP) in the cytosol. This regulates the activity of protein kinase A (PKA), which is a tetrameric holoenzyme consisting of two catalytic and two regulatory subunits [36,81,83]. After binding of cAMP the regulatory subunit dissociates from the catalytic subunit, releasing it to its active state [24,35,81,83]. The activated form of the catalytic subunit phosphorylates GPR161, increasing its activity and creating a feedback loop [36,81,84]. The activated catalytic subunit in combination with the glycogen synthase kinase 3β (GSK3β) also leads to the proteolytic cleavage of the full length forms of the transcription factors GLI2 and GLI3 into their repressor forms, which ultimately prevents the transcription of target genes of the hedgehog signaling pathway [85–87].

After binding of hedgehog (Hh) ligand to PTCH1 the receptor is removed from the cilium, which enables the localization of hedgehog components like Smo to the ciliary membrane at the tip region. This also includes the glioma associated oncogene (GLI1) and the suppressor of Fused (SuFu) [38,81,87]. GPR161 is removed from the cilium and Smo inhibits the activity of AC, leading to decreasing cytosolic levels of cAMP, which in turn inhibits the activity of PKA [36,81,83]. The ciliary enrichment of Smo also triggers the release of Sufu from full length Gli transcription factors, which leads to their phosphorylation and subsequently the formation of Gli transcriptional activator (GliA). GliA translocates to the nucleus and activates the transcription of hedgehog target genes [85–87].

The regulation of hedgehog signaling is highly regulated and dependent on the primary cilium. This includes e.g. the negative regulation mediated by GPR161 in the primary cilium in the hedgehog-off state, which requires the interaction with TULP3 attached to IFT-A [2,3,13,81].

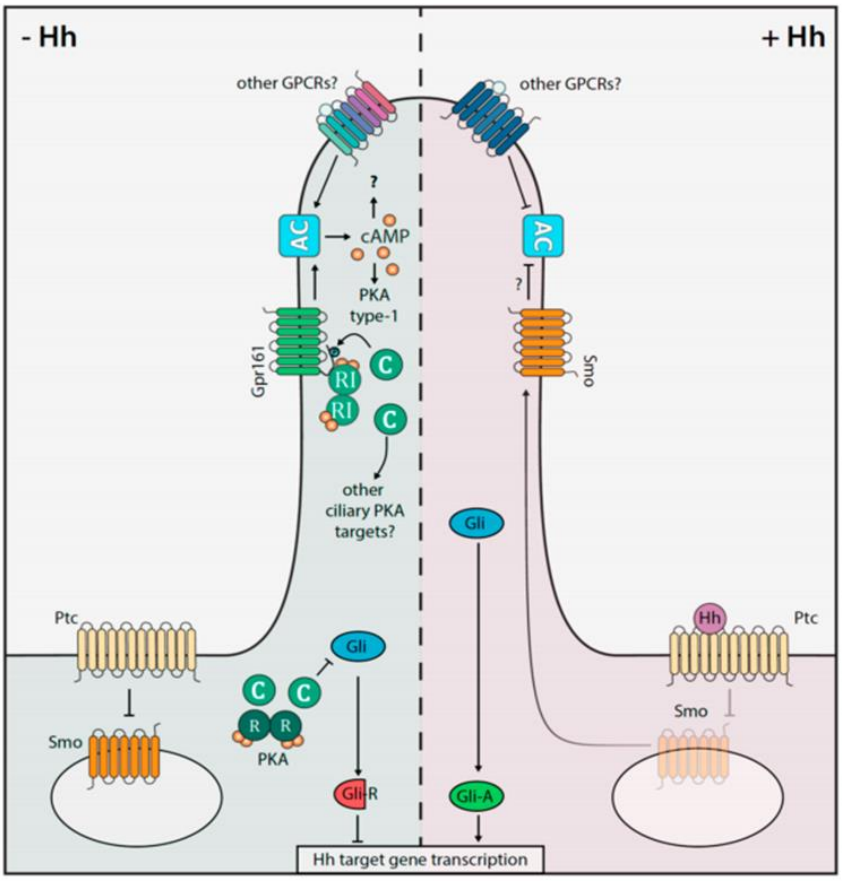

Figure 5: Hedgehog signaling in the primary cilium. *A schematic view of a primary cilium is shown. On the left the hedgehog off-state is shown in the absence of stimulation. Patch1 (Ptc) inhibits SMO. Gpr161 in the primary cilium activates adenylate cyclase (AC) which in turn generated cAMP. PKA-1 is activated by cAMP and phosphorylates GPR161, creating a feedback-loop, as well as transforming GLI into its repressor form, which inhibits the expression of hedgehog target genes. Upon binding of hedgehog ligand to Patch1, SMO localizes to the cilium and inhibits adenylate cyclase, which leads to the transformation of GLI into its activator form and the transcription of hedgehog target genes. Taken from* [81].

Ciliopathies

Due to the crucial role of cilia in a broad variety of cellular processes, defects in one of the over 500 genes coding for ciliary components are associated with several diseases, which are commonly referred to as ciliopathies [7,15]. Since cilia are found in many different tissues and have changing function depending on the developmental stage, ciliary dysfunction can lead to a vast spectrum of diseases, varying in type and severity. This spectrum ranges from isolated retinal dystrophies to renal disease, liver fibrosis, cerebral anomalies, diabetes, infertility and skeletal defects [7,15–17]. The onset and type of disease can also vary depending on the type of mutation and even between individuals harbouring the same genetic defects [12,18,19,88]. Ciliopathies can not only be caused by defects in ciliary genes itself but also by non-ciliary proteins that are crucial for proper ciliary function. So far more than 35 ciliopathies have been reported which often show similarities in the observed clinical phenotype [7,15].

Retinal dystrophies are a heterogeneous group of disorders, which all share the progressive loss of photoreceptor cells, leading to increasing vision impairment. Retinitis pigmentosa is a specific form of retinal dystrophy, with a prevalence of about 1 in 4,000 individuals [23,89]. It is characterized by the primary degeneration of the rod photoreceptor, causing night blindness and increasing visual field loss, that can progress up to legal blindness within decades [59,90]. The onset of retinal dystrophies varies widely from congenital forms to late onset forms. Leber congenital amaurosis is a form of hereditary retinal dystrophy that can lead to photoreceptor death and blindness at an early age. It can be caused by mutations in at least 15 genes, which do not exclusively code for ciliary proteins. It shows a large variation in the phenotype, with patients showing only mild retinal vessel attenuation to maculopathy or white retinal spots, indicating gene specific clinical presentation [12,91,92].

More severe forms of ciliopathies include Jeune syndrome, also referred to as Jeune asphyxiating thoracic dysplasia (JATD). It is mainly characterized by shortened ribs, that lead to a long and narrow thorax, causing respiratory problems or failure. It can additionally be accompanied by liver fibrosis and kidney failure, polydactyly and retinal dystrophy [25,93,94]. Mainzer Saldino is also called cono-renal syndrome and mainly manifests in the form of chronic kidney disease (nephronophtisis) that progresses over time and cone-shaped ends at the epiphyses in the phalangites. In addition, patients often display retinal dystrophies, hepatic fibrosis or other skeletal defects such as craniosynostosis [7,26,33,93]. Sensenbrenner, also called cranioectodermal dysplasia, leads to skeletal anomalies such as a narrow thorax and syndactylism with additional ectodermal defects like teeth malformations. Patients may also display kidney problems and liver fibrosis as well as retinal dystrophies [17,95–97].

Aim of the study

Cilia are antenna-shaped organelles protruding from the cellular surface of most eukaryotic cells [1–3]. They are a cellular organelle highly conserved through evolution and can be subdivided in two main groups: primary (immotile) cilia, which serve as signaling hubs and secondary (motile) cilia, which exhibit active movement [1,4–8]. Due to the crucial role of primary cilia in signaling pathways such as Notch, Wnt, Hippo, mTOR and hedgehog [3,5,7,82,98,99] defects in genes coding for ciliary components are associated with a variety of severe diseases which are commonly referred to as ciliopathies [5,7,13,15]. Ciliopathies vary considerably regarding the affected tissue as well as the type and severity of the clinical phenotype. Mutations in a single locus can be phenotypically heterogeneous, while at the same time mutations in different genes can lead to similar clinical manifestations [18,19]. In this study the effect of disease-associated missense mutations in components of the IFT-A complex is to be investigated. IFT-A is important for the active transport of cargo within the cilium, the so called intraflagellar transport (IFT). While transport in anterograde direction is achieved by kinesin-2 in combination with the IFT-B protein complex cargo is transported in the retrograde direction by dynein-2 and the IFT-A protein complex [2,11,12].

The main hypothesis for this work is that disease-associated missense mutations in components of the IFT-A complex lead to distinct changes in protein-protein interactions (PPIs). This idea is known as the edgetic concept. Core point is the idea that a mutation in a protein leads to the loss of specific interactions, represented by loss of an edge in a protein network, rather than a full loss of the protein, which would mean the loss of a node in the network [20–22]. By analysing the specific changes induced by missense mutations in IFT-A, the mechanisms underlying ciliopathies will be examined and pathogenic mechanisms assigned to specific disease phenotypes. The generated insights will illuminate general principles of genetic diseases and are not limited to ciliopathies.

The first aim of this study is to identify the wildtype interactomes of four components of the IFT-A complex (IFT43, IFT121, IFT122 and IFT140) as well as a shorter isoform of IFT140. Protein complex analysis using affinity purification will be used to investigate wildtype protein interaction. By generation of robust datasets and stringent statistical analysis a list of bona fide interaction partners will be obtained. The generated data will create valuable new insights into the protein interactions of the wildtype forms of IFT43, IFT121, IFT122 and IFT140 and lead to the discovery of novel interactions partners. This will generate insights into the cellular process in which IFT-A is involved. The analysis of the short isoform of IFT140 will reveal if it is able to bind to the whole IFT-A complex and therefore might ensure the integrity of the IFT-A protein complex.

The second aim is to assess the changes in the wildtype interactome induced by missense mutations in the IFT-A components. The comparison of in total 37 mutants with the corresponding wildtype conditions will reveal the effect of disease-associated missense mutations on protein interaction networks. The effect of these mutations will be compared to the effect of single nucleotide polymorphisms (SNPs).

The third aim is to fit the generated insights into known concepts. The analysis of the effect of the disease-associated missense mutations will allow to identify potential edgetic effects, with missense mutations leading to specific changes in distinct PPIs rather than a total loss of all protein interactions observed in the corresponding wildtype. To validate the hypothesis that missense mutations are hypomorph and have a quantitative effect on the native protein function, it will be assessed whether missense mutations in IFT-A components lead to a quantitative disruption of PPIs.

Fourth aim is to examine if the effects that are observed for missense mutations on PPIs show a correlation to the disease severity in patients harbouring these mutations. Therefore, the clinical phenotype will be assessed for patients harbouring mutations on both alleles for which mass spectrometric data can be obtained. By comparing the severity of the effect of missense mutations with the allelic combination and clinical phenotype in patients it will be analysed if a genotype-phenotype correlation can be observed.

As a fifth aim a functional validation of the effects of IFT-A on signaling pathways will be analysed. For functional analysis of IFT140 a CRISPR/Cas9-mediated knockout will be generated in hTERT-RPE1 cells. The relevance of primary cilia and IFT-A for hedgehog signaling is well established [5,36,81,98]. To investigate the effect of IFT140 on the hedgehog signaling pathway the generated knockout cell line will be used for analysis of the expression of the hedgehog target gene GLI1. Via qPCR it will be examined if hedgehog signal is overactivated in the absence of functional IFT140.

The insight generated in this study will enable a better understanding of the role of IFT-A in cellular processes. The analysis of the effect of missense mutations on protein interaction networks will allow an examination of the edgetic hypothesis and reveal potential quantitative effects. This will lead to a better understanding of disease mechanisms and of the genotype-phenotype correlation in affected patients. The functional analysis of IFT-A will generate further insights into its role in cellular signaling and hopefully lead to a therapeutic approach in the future.

Material

Equipment

Analytical balance ABJ 120-4M	Kern & Sohn GmbH, Germany
Autoclave DX-150	Systec, Germany
CO_2-Incubator HeraCell 150i	Heraeus, Germany
Compartment dryer T20	Heraeus, Germany
Developer Curix 60	Agfa, Belgium
Freezer (-80°C) Forma 900 Series	Thermo Fisher Scientific, USA
Freezer Liebherr Comfort	Liebherr, Switzerland
Gene Ruler 1 kb Plus	Thermo Fisher Scientific, USA
Ice machine AF200	Scotsman, USA
Imaging camera Fusion FX	Vilber, France
Incubator INB 300	Memmert, Germany
IntelliMixer	NeoLab, Germany
Laboratory balance S72	Kern & Sohn GmbH, Germany
Laboratory hood model 854006.1	Wesemann, Germany
Laminar flow MSC 12	Thermo Fisher Scientific, USA
Magnetic stirrer and heater MR Hei-Standard	Heidolph, Germany
Megafuge 16	Heraeus, Germany
Microplate reader Spark	Tecan, Switzerland
Microscope PrimoVert	Zeiss, Germany
Microwave	Siemens, Germany
Multifuge X3R	Heraeus, Germany
NanoDrop ND-1000 Spectrophotometer	PeqLab, Germany
PageRuler Prestained Protein Ladder (170 kDa)	Thermo Fisher Scientific, USA
pH meter PB-11	Sartorius, Germany
Platform shaker Duomax 1030	Heidolph, Germany
Refrigerated Vapor Trap RVT400-230	Thermo Fisher Scientific, USA
Roller Mixer RM5	Assistant, Germany
Rotating incubator Infors HAT	Ecotron, Germany
Speedvac Concentrator SPD111V-230	Thermo Fisher Scientific, USA
Tabletop centrifuge Mini Star	VWR, Germany
Thermoblock MBT 250	ETG, Germany
Thermomixer Univortemp	Universal Labortechnik, Germany
Transluminator Fluo Link (312 nm)	Bachofer, Germany
Ultrapure water purification system Nanopure	Thermo Fisher Scientific, USA
Vacuum pump 2522Z-02	Welch, USA

Consumables

Amersham Hyperfilm ECL	GE Healthcare, USA
Baffeled flask 250/500 mL	Neolab, Germany
Blue rack for 6/12 Tubes	GLW Storing Systems, Germany
Box for pipette tips	Gilson, USA
Chip for automated cell counting	Tecan, Switzerland
Cell culture dish, 6 well	BD Bioscienes, USA
Cell scraper	Sarstedt, Germany
Centrifugation tubes 15/50 ml	Greiner bio-one, Austria
Cryo Tube Rack	Nunc, USA
Cryobox 0.5/1.5/2.0 ml tubes	Carl-Roth, Germany
Culture tube 14 ml	BD Biosciences, USA
Cuvette 1.5 ml	Sarstedt, Germany
Cuvette 0.7 ml quartz	Carl-Roth, Germany
Drigalski spatula	Carl-Roth, Germany
Gel loading tips	Carl-Roth, Germany
Glas plate with 0.75mm spacer	Bio-Rad, USA
Gloves purple nitrile	Kimberly-Clark, USA
Gloves soft nitrile	Paul Hartmann, Germany
Graduated measuring glass	Duran Group, Germany
Hybond-P PVDF Transfer membrane	GE Healthcare, USA
Hypercassette	GE Healthcare, USA
Hyperscreen	GE Healthcare, USA
Icebath	Neolab, Germany
Inlays for Cryobox for 0.5/1.7/2.0 ml tubes	Carl-Roth, Germany
Inoculation loop	Carl-Roth, Germany
Laboratory bottles, 50-2000 ml	Neolab, Germany
MicroSpin Columns	GE Healthcare, USA
Multiwell plate, 96wells	Greiner Bio-One, Austria
Parafilm sealing foil	Brand, Germany
Pasteur capillary pipette	VWR International, USA
Petridish 90 x 14.2 mm	VWR International, USA
Pipettes 2/10/20/200/1000 µl	Gilson, USA
Pipette tips 1-10/1-200/101-1000 µl	Sarstedt, Germany
Pipettes (serological) 2/5/10/25/50 ml	BD Biosciences, USA
Polypropylen insert with bottom spring	Sigma-Aldrich, USA
Reaction tube 0.2 ml	Eppendorf, Germany
Reaction tube (safelock) 0.5/1.5/2.0 ml	Eppendorf, Germany
Reaction tube 15 ml	Sarstedt, Germany

Reaction tube 50 ml	BD Biosciences, USA
Short plate	Bio-Rad, USA
Spin Columns, 3MWCO, 30MWCO	GE Healthcare, USA
Stage Tips C-18, 200 µl	Thermo Fisher Scientific, USA
Sterilfilter Millex 0.22 µm	Merck, Germany
Tissue Dishes, 10 cm, Nunclon Surface	Nunc, USA
Tissue Dishes, 14 cm, Nunclon Surface	Nunc, USA

Chemicals

1,4-Dithiothreitol (DTT)	Merck, Germany
2-Iodacetamide (IAA)	Merck, Germany
2-Mercaptoethanol	Sigma-Aldrich, USA
2-Propanol LC grade	Merck, Germany
2-Propanol p.a.	Merck, Germany
Acetic acid	Merck, Germany
Acetonitrile LC-MS CHROMASOLV®, ≥99.9%	Sigma-Aldrich, USA
Acetone	Merck, Germany
Agar-Agar	Carl-Roth, Germany
Agarose	Lonza, Switzerland
Ammonium Bicarbonate	Sigma-Aldrich, USA
Ammonium Persulfate	Merck, Germany
Ampicillin Sodium Crystalline	Carl-Roth, Germany
Bis-Acrylamid/Acrylamid (37.5:1:30%)	Serva Elektrophoresis, Germany
Chloroform p.a.	Merck, Germany
Dimethyl Sulfoxide (DMSO)	Applichem, Germany
EDTA Disodium Salt Dihydrate	Applichem, Germany
Ethanol p.a.	Merck, Germany
Ethidiumbromide	Applichem, Germany
Formaldehyde Solution (37%)	Sigma-Aldrich, USA
Glycerol	Carl-Roth, Germany
Glycine	Carl-Roth, Germany
HEPES	Sigma-Aldrich, USA
Hydrochloric Acid p.a.	Merck, Germany
Kanamycin Sulfate	Carl-Roth, Germany
Magnesium Chloride	Sigma-Aldrich, USA
Methanol LC-MS grade	Merck, Germany
Methanol LC-MS grade	VWR International, USA
Methanol p.a.	Merck, Germany
Nonidet P40	Roche, Germany

Polyethylenimine, Linear (MW 25,000)	Polysciences, USA
RapiGest SF Surfactant	Waters, USA
Sodium Chloride p.a.	Merck, Germany
Sodium Dodecylsulfate, Pellet	Sigma-Aldrich, USA
Sodium Dodecylsulfate, 20%	Applichem, Germany
Sodium Hydroxide pellets p.a.	Carl-Roth, Germany
Sodium Thiosulfate Pentahydrate, supra pure	Merck, Germany
TEMED p.a.	Merck, Germany
Trifluoroacetic Acid, for protein seq.	Merck, Germany
Tris(hydroxymethyl) Aminomethane (Tris ultrapure)	Sigma-Aldrich, USA
Trypsin from porcine pancreas, proteomics grade	Sigma-Aldrich, USA
Tryptone/ Peptone from Casein	Carl-Roth, Germany
Tween® 20	Sigma-Aldrich, USA
Water, HPLC grade	Merck, Germany
Water bath stabilizer, AKASOLV Aqua Care	Carl-Roth, Germany
Yeast Extract	Carl-Roth, Germany

Special reagents

ANTI-FLAG®-M2 Affinity Gel	Sigma-Aldrich, USA
BioRAD reagent (5x Bradford concentration)	BioRad, USA
Blotting Grade milk, nonfat dry	Bio-Rad, USA
Bovine Serum Albumin (BSA)	PAA, Austria
Coomassie Brilliant Blue	Merck, Germany
dNTP mix 10 mM	Promega, USA
Dream Taq Green Buffer (10x)	Thermo Fisher Scientific, USA
Dulbecco's Modified Eagle Medium	Sigma-Aldrich, USA
Dulbecco's PBS	Sigma-Aldrich, USA
ECL plus Western Blotting Substrate	Thermo Fisher Scientific, USA
ECL Western Blotting Substrate	Thermo Fisher Scientific, USA
FastDigest buffer	Thermo Fisher Scientific, USA
FastDigest Bbsl (10U/µl)	Thermo Fisher Scientific, USA
Fetal Bovine Serum (FBS)	Sigma-Aldrich, USA
FLAG peptide	Sigma-Aldrich, USA
Fluoromount-G®	Southern Biotech, USA
GeneRuler™1kb Plus DNA ladder	Thermo Fisher Scientific, USA
Geneticindisulfat (G418) CELLPURE® 50 mg/ml	Carl-Roth GmbH, Germany
Normal Goat Serum	Merck, Germany
M-MLV RT 5x buffer	Promega, USA
Penicillin/ Streptomycin	Life Technologies, USA

Phosphatase Inhibitor Cocktail 2	Sigma-Aldrich, USA
Phosphatase Inhibitor Cocktail 3	Sigma-Aldrich, USA
Phusion High Fidelity buffer	Thermo Fisher Scientific, USA
PNK buffer (10x)	New England BioLabs, USA
Puromycin (10 mg/ml)	Life Technologies, USA
Protease Inhibitor Cocktail Complete	Roche, Germany
Protein Assay Dye Reagent	Bio-Rad, USA
Random Primers	Promega, USA
S.O.C. medium	Invitrogen, USA
SSO Advanced SYBR® Green	BioRad, USA
Strep Tactin Superflow (50% suspension)	IBA, Germany
Step Elution Buffer (10x)	IBA, Germany
TriFast	VWR, USA
Trypsin EDTA	Life Technologies, USA

Buffers, solutions and media

In this study, deionized water is described as dH_2O, while ddH_2O refers to ultra-pure water.

E.coli culture

LB-Medium	1 % (w/v) Tryptone/ Peptone from Casein
	0.5 % (w/v) Yeast Extract
	1 % (w/v) NaCl
	adjust to pH 7.0 using NaOH
	in dH_2O
LB-Agar	1 % (w/v) Tryptone/ Peptone from Casein
	0.5 % (w/v) Yeast Extract
	1 % (w/v) NaCl
	1 % (w/v) Agar-Agar
	in dH_2O

Mammalian cell culture

Cryo Medium	90 % FBS
	10% DMSO
Growth Medium	Dulbecco's Modified Eagle Medium
	10 % FBS
	0.5 % Penicillin/ Streptomycin

Starvation Medium	Dulbecco's Modified Eagle Medium 0.5 % Penicillin/ Streptomycin
PEI Transfection Reagent	1 mg/ml Polyethylenimine (PEI) in dH_2O

SDS-PAGE and Western blot analysis

Blocking Solution	5 % BSA or 5% milk in TBST (1x)
Laemmli buffer (5x)	250 mM Tris-HCl pH 6.8 5 % SDS 50 % Glycerol 500 mM 2-Mercaptoethanol 0.05 % (w/v) Bromphenol Blue in ddH_2O
Running buffer (10x)	2 M Glycine 250 mM Tris 1 % (w/v) SDS in dH_2O
Separation Gel	25 % Tris-HCl pH 8.8 12 % Acrylamide 0.1 % SDS 0.2 % TEMED 0.05 % Ammonium Persulfate (APS) in ddH_2O
Stacking Gel	14 % Tris-HCl pH 6.8 4.2 % Acrylamide 0.1 % SDS 0.4 % TEMED 0.1 % Ammonium Persulfate (APS) in ddH_2O

TBST (10x)	300 mM Tris 1.5 M NaCl 1 % Tween® 20 in dH_2O adjust pH to 7.4 using HCl
Western buffer (10x)	1.92 M Glycine 250 mM Tris in dH_2O
Western buffer (1x)	10 % Western buffer (10x) 20 % MeOH In dH_2O

Affinity purification

FLAG-Peptide (25x)	5 mg/ml Flag-Peptide in TBS (1x)
Strep Elution Buffer (10x)	10% in TBS
Lysis Buffer	0.55 % Nonidet P40 2 % Protease Inhibitor Cocktail Complete (PIC) 1 % Phosphatase Inhibitor Cocktail 2 1 % Phosphatase Inhibitor Cocktail 3 in TBS (1x)
TBS (10x)	300 mM Tris 1.5 M NaCl in dH_2O adjust pH to 7.4 using HCl
Washing Buffer	0.12 % Nonidet P40 1 % Phosphatase Inhibitor Cocktail 2 1 % Phosphatase Inhibitor Cocktail 2 in TBS (1x)

Kits

Bio-Rad Protein Assay Kit	Bio-Rad, USA
Enhanced Chemiluminescence Kit, ECL	GE Healthcare, USA,
EZ-PCR Mycoplasma Detection Kit	Sartorius, Germany
Lipofectamine ™ 3000 Transfection Kit	Thermo Fisher Scientific, USA
Monarch® Plasmid Miniprep kit	New England BioLabs, USAS
PureYield™ Plasmid Midiprep Kit	Promega, USA

Enzymes

BP Clonase II Enzyme Mix, with proteinase K	Invitrogen, USA
LR Clonase II Enzyme Mix, with proteinase K	Invitrogen, USA
DpnI Restriction enzyme	Invitrogen, USA
Dream Taq DNA.Polymerase 5 U/µl	Thermo Fisher Scientific, USA
M-MLV polymerase	Promega, USA
Phusion High Fidelity polymerase	Thermo Fisher Scientific, USA
T4 DNA Ligase (1U/µl)	Roche AG, Switzerland
T4 polynucleotide kinase (PNK; 10 U/µl)	New England BioLabs, USA
Trypsin NB sequencing grade	Serva Electrophoresis GmbH, Germany

Antibodies for immunofluorescence staining

Primary Antibody	**Species**	**Dilution**	**Vendor**
Anti-Arl13b	Mouse (monoclonal)	1:100	Proteintech, USA
Anti-IFT140	Rabbit (monoclonal)	1:100	Proteintech, USA
Secondary Antibody	**Species**	**Dilution**	**Vendor**
Anti-mouse IgG	goat (polyclonal)	1:350	Molecular Probes, USA
Anti-rabbit IgG	goat (polyclonal)	1:350	Molecular Probes, USA

Antibodies for Western blotting

Primary Antibody	**Species**	**Dilution**	**Vendor**
Anti-IFT140	Rabbit (polyclonal)	1:100 (BSA)	Proteintech, USA
Anti-TULP3	Rabbit (polyclonal)	1:100 (milk)	Proteintech, USA
Anti-GAPDH	Rabbit (monoclonal)	1:10,000 (milk)	Cell Signaling, USA
Anti-FLAG-HRP	Mouse (monoclonal)	1:2,500 (milk)	Sigma-Aldrich, USA
Secondary Antibody	**Species**	**Dilution**	**Vendor**
Anti-rabbit IgG	goat (polyclonal)	1:350	Molecular Probes, USA

Instruments

Axio Imager Z1 ApoTome microscope	Carl Zeiss, Germany
BioRad T100™ Thermal Cycler	BioRad, USA
BioRad CFX96 Real-Time System	BioRad, USA
Orbitrap Fusion Tribrid	Thermo Fisher Scientific, USA
Ultimate 3000 Nano-RSLC	Thermo Fisher Scientific, USA
µ-Precolumn Acclaim PepMap100 C18 (300µm i.d. x 5mm)	Dionex, USA

Software

Adobe Illustrator	Adobe System Inc., USA
BioRad	BioRad, USA
Mendeley	Elsevier, Netherlands
MaxQuant 1.6.1.0 [100]	MPI of Biochemistry, Germany
Microsoft Office 365	Microsoft, USA
Perseus 1.6.5.0	MPI of Biochemistry, Germany
R	R core team, Austria
SparkControl 2.2	Tecan Group AG
XCalibur 2.07	Thermo Fisher Scientific, USA
ZEN 3.0 (blue edition)	Carl Zeiss Microscopy GmbH

Databases

CCTop	www.crispr.cos.uni-heidelberg.de
Ensembl	www.ensembl.org
GnomAD	www.gnomad.broadinstitute.org/
IntAct	www.ebi.ac.uk/intact/
Multalin	www.multalin.toulouse.inra.fr
NCBI Protein	www.ncbi.nlm.nih.gov/
NCBI PubMed	www.ncbi.nlm.nih.gov/
STRING	www. string-db.org/
Swiss-Prot	www.expasy.ch/sprot/
UniProt	www.uniprot.org/

Methods

Cloning and bacterial cell culture

Plasmids and Gateway cloning

For Gateway cloning a pDONR201 vector with a kanamycin resistance (Invitrogen, USA) and pDEST vector with a pcDNA 3.0 backbone and ampicillin resistance (Invitrogen, USA; modified with N-terminal Strep/FLAG [101] or HA tag) were used [78]. To 1 µL of a DNA solution (~100 ng/µL) containing pDEST plasmid with the Strep/FLAG sequence upstream of the DNA 1 µL of a DNA solution (~100 ng/µL) containing an entry vector with the sequence that is to be introduced was added. After incubation for 1 hour at 25 °C with 2 µL of Elution buffer (from Monarch® Plasmid Miniprep kit) and 1 µL of LR clonase II the resulting vector was introduced into *E.coli* through transformation.

Polymerase chain reaction

For amplification of specific DNA fragments a polymerase chain reaction (PCR) was performed using a BioRad T100™ Thermal Cycler. The pipetting scheme and the cycler setting are shown below.

Table 1: Pipetting scheme for PCR.

Ingredient	Volume per sample in µl
GC rich buffer (10x)	2
dNTP (10mM)	0.2
Phusion Polymerase	0.3
Primer reverse (1:10)	1
Primer forward (1:10)	1
ddH_2O	14.5
Template DNA	1
Total	20

Table 2: Thermocycle condition for Phusion polymerase.

Time	Temperature (°C)	Cycles
5 min	95	
30sec	95	x 30
40sec	Depending on primer pair	
1 min per 1000bp	72	
5 min	72	

Site-directed mutagenesis

Mutant constructs were generated using primers carrying the desired mismatch to obtain the specific mutation [102]. Following PCR a Dpn1 digest was performed for 1h at 37°C to digest methylated template DNA [78]. The constructs were transformed into DH5α cells and bacteria grown in kanamycin selection conditions. DNA was isolated using a PureYield™ Plasmid Midi Preparation Kit and gateway cloning with a destination vector harbouring a N-terminal Strep/FLAG-tag was performed as described below. Constructs were transformed into DH5α cells and bacteria grown in ampicillin selection conditions prior to DNA isolation as described below [78]. All expression constructs were verified via sequencing.

Table 3: DNA oligomers used for generation of missense mutation constructs. *Site-directed mutagenesis primers for each missense mutation in IFT-A genes. Overhangs are highlighted in blue, base pairs coding for the targeted amino acid change in red with the exact position of the missense mutation indicated in bold letters.*

IFT43

Mutation	Forward Primer	Reverse primer
p. W179R	GATGTCGGC**A**GGGACTGGG	GTCCCAGTCCC**T**GCCGAC

IFT121

Mutation	Forward Primer	Reverse primer
p. S168R	CATGGTCTGCGGACAG**A**AAAG	GTAAGACTTT**T**CTGTCCGCAG
p. D841V	CTATATGTTAGAGG**T**TTATGAAG	CTAACCCTTCATAA**A**CCTCTAAC
p. Y971C	GTCAAGAAGCTCTGT**G**TACTG	CTGACAGTACA**C**AGAGCTTC
p. W1153C	CTGAGTATCAATTCTG**C**ATGTG	CATACACTGCACAT**G**CAGAATTG

IFT122

Mutation	Forward Primer	Reverse primer
p.W7C	CGTGTTGACGTG**T**AGAGATAAAG	GGCTTTATCTCT**A**CACGTCAAC
p. S373F	GAGCAGAACT**T**CTGGGTGTG	GTCCACACCCAG**A**AGTTCTG
p. V442L	TGCAAAGAGCTT**C**TCAAGAAG	CAATCTTCTTG**A**GAAGCTCTTTG
p. V553G	CCTGAAGATCTTCG**G**GGACAATC	GAGATTGTCC**C**CGAAGATCTTC
p. G546R	GGGCTGAAGAAT**C**GACAGATC	CAGGATCTGTC**G**ATTCTTCAG
p. F621C	GACATGCTCTGCT**G**CTCGG	CTCCCGAG**C**AGCAGAGCATG
p. G623V	CTGCTTCTCGG**T**AGGAGGCTAC	GAGGTAGCCTCCT**A**CCGAGAAG
p. L763P	GGCCGCCAAAC**C**GTACAAG	CCTCTTGTAC**G**GTTTGGCG

IFT140

Mutation	Forward Primer	Reverse primer
p. P71L	GTGCTGGCACCTGACGCGG	CACCAGCCGCGTCAGGTGC
p. V108M	GACATCACCATGCTCCGTTGG	GGGCTCCAACGGAGCATGGTG
p. G140R	CGAGTGCAACGGACGCCTCTGCTG	GTTTCAGCAGAGGCGTCCGTTGC
p. G212R	GTCTGATGGACCGGACAGTG	CATAGTGCACTGTCCGGTCCATC
p. I233M	GCAGACAGCACGATGCAGATG	CAGCATCTGCATCGTGCTGTC
p. E267G	GCAAAGCAGAAGGAGTGATGAAG	CTTGACCTTCATCACTCCTTCTGC
p. V292M	GCAGCCTTCTCATGATGGCCGTC	CCCCGACGGCCATCATGAGAAG
p. Y311C	GAACGAGGAGAGAATTGTATACTG	CTGGACTCAGTATACAATTCTCTCC
p. C329R	GGAGAGAATATGAACCGTGTGTGTTACTG	CTTTACAGTAACACACACGTTCATATTC
p. C333Y	GTGTGTGTTACTATAAAGTCAAAGG	GAAGACCTTTGACTTTATAGTAACAC
p. A341T	GTCTTCTGGCCACTGGTACCGACAG	CTCTGTCGGTACCAGTGGCCAG
p. A418P	CACCAGCAAGTGCCCGCCATG	CTGCATGGCGGGCACTTGCTG
p. L440P	CACACAGCCCGCGCACCGACATG	GTGCATGTCGGTGCGCGGGCTG
p. T484M	CTTGTGTGAGATGCCTGTGTTAG	CATTGCTAACACAGGCATCTCACAC
p. G522E	GAGACTGAGGAGAATCCCTG	GAAGCAGGGATTCTCCTCAG
p. C663W	GCCCCGGCTGTTTGTATGGGAAG	GCACGGCTTCCCATACAAACAGCC
p. E664K	GCTGTTTGTATGCAAAGCCGTG	CCTGCACGGCTTTGCATACAAAC
p. E790K	GGAGACATGGACAAAGCCTTCAAATCC	CTTGATGGATTTGAAGGCTTTGTCCATG
p. R871C	GAAGTGCAAGTGCCACGACCTC	CAGGAGGTCGTGGCACTTGCAC
p. S939P	CAGGATGCTGCCGGAGGACCTG	CGGCAGGTCCTCCGGCAGCATC
p. A974V	GATGGACGCCGTGCTGCACTAC	GTAGTAGTGCAGCACGGCGTC
p. E1065K	GCTGAGCTCCCCCAAGGACATG	CGATCATGTCCTTGGGGGAGC
p. C1360R	GAGTCCATCAAGCAGCGTGAGCTG	CAGGAGCAGCTCACGCTGCTTGATGG
p. L1399P	GCCTACAGATTCCCGGAGGAGATG	CGCCGCATCTCCTCCGGGAATCTG

CRISPR/Cas9-mediated knockout

The CRISPR/Cas9 system was used to generate specific IFT140 knockout cell lines in exon 4 according to previous publications [103]. Designing sgRNAs was conducted using CCTop software and predicted targets were chosen according to their gene location. Also, off-targets were taken into consideration and the overall CRISPR/Cas9 efficiency score. Top and bottom strands were annealed and subsequently cloned into the Cas9 vector (pSpCas9(BB)-2A-Puro (PX459) V2.0; Addgene; USA), followed by transformation into competent *E.coli* DH5α bacterial cells via heat shock and plated onto ampicillin supplemented LB-Agar dishes. Colonies were picked and transferred to selective LB-medium followed by DNA isolation according to the PureYield™ Plasmid Midiprep protocol. Cells were transiently transfected according to Lipofectamine™ 3000 reagent protocol prior to selection treatment followed by clonal selection with puromycin. Genomic DNA was extracted and purified. For verification of successful KO generation, the region of interest was amplified by PCR, the product purified and sent in for Sanger sequencing.

Table 4: sgRNAs for CRISPR/Cas9-mediated knockout of IFT140.

sgRNA forward	sgRNA reverse
CACCGGGCCTCTCGACGTGTGTATC	AAACGATACACACGTCGAGAGGCCC

RNA Isolation

RNA was isolated from hTERT-RPE1 cells at 80% to 100% confluency in a 6-well plate. All steps were performed with filter tips, on ice and under the hood. After washing cells with 1 mL PBS in total 1 mL of TriFast was added per well, pipetted up and down and incubated for 5 min at RT. Cells were scratched and transferred into a 1.5 mL Eppendorf tube before adding 200 µL Chloroform. The mixture was vortexed strongly and incubated for 5 min at RT. Samples were centrifuged for 5 min at 12,000 g and 4°C before transferring the upper phase in a new 1.5 mL Eppendorf tube and adding 500 µL isopropanol to precipitate the RNA. The solution was vortexed strongly prior to incubation for 10 min on ice and centrifugation for 10 min at 12,000 g and 4°C. Subsequently the supernatant was discarded and the pellet washed twice with 1 ml 75% Ethanol with centrifugation steps in between at 12,000 g at 4°C for 10 min. After air drying the pellet under laminar flow at RT the pellet was resuspended with 30 µL nuclease-free water and incubated at 56°C for 10 min at 300 rpm. The RNA concentration of the samples was measured using a NanoDrop ND-1000 Spectrophotometer and the final concentration of 0.1 µg/µL was calculated for cDNA synthesis.

cDNA synthesis

All steps for cDNA synthesis were performed with filter tips and at RT. To each sample 7 µL nuclease free water, 1 µL random primers (500 µg/mL) and 20 µL RNA (0.1 µg/µL) were added and incubated at 70°C for 5 min before being transferred onto ice for 5 min. After short centrifugation 10 µL M-MLV RT 5x Buffer, 2.5 µL dNTPs, 8.5 µL nuclease-free water and 1 µL M-MLV polymerase were added to each sample. The synthesis of cDNA was performed in several subsequent steps: 10 min at 23°C, 50 min at 50°C and 15 min at 70°C before storage of cDNA at -80°C.

Real-time PCR (qPCR)

Expression level of a gene of interest was quantified using real time PCR (qPCR). A mastermix with SYBR® Green and qPCR conditions was prepared according to table 5. The PCR was performed on a BioRad CFX96 Real-Time System with biological triplicates. Analysis and quantification was done using the BioRad software. For a relative quantification of the results the housekeeping gene *GAPDH* (Glycerinaldehyd-3-Phosphat Dehydrogenase) was used for normalization of values due to its constant expression level in cells.

Table 5: Pipetting scheme for qPCR.

Ingredient	Volume per sample in µl
SSO Advanced SYBR Green	7.5
Primer reverse (1:10)	2.25
Primer forward (1:10)	2.25
Nuclease-free water	1.5
cDNA	1.5
Total	15

Table 6: Cycler settings for qPCR.

Time	Temperature (°C)	Cycles
1 min	95	
10sec	95	
30sec	59-60	x 40
5 sec, 0.5°C/cycle	65	Melting curve
5 sec, 0.5°C/cycle	95	
Hold	4	

Transformation of chemical competent *E.Coli*

5 µL of plasmid DNA were added to 50 µL chemically competent *E.coli* DH5α bacterial cells. After incubation on ice for 45 min cells were heat shocked for 45s at 42°C and subsequently cooled for 2 min on ice. 250 µL S.O.C. medium was added and incubated for 50 min at 37°C while shaking before 150 µL of the mixture were added onto a LB agar plate and incubated overnight at 37°C. A single colony was transferred into a 500 mL baffled flask containing LB medium and selection antibiotic (100 µg/mL ampicillin) added prior to incubation overnight at 37°C while shaking at 180 rpm.

DNA isolation from *E.coli* and Measurement of DNA concentration

DNA isolation was performed using a PureYield™ Plasmid Midiprep System according to protocol. All buffers were prepared according to the protocol. After pelleting bacterial cells using 50 mL Falcon tubes and centrifugation at 5,000 g (RT) for 10 min the pellet was resuspended in 3 mL Resuspension Solution. 6 mL Lysis solution were added and inverted five times prior to incubation for 3 min at RT. 10 mL of neutralisation Solution were added to the sample and inverted five times prior to centrifugation at 15,000 g (RT) for 15 min. A column stack was assembled on a vacuum manifold according to protocol, placing the clearing column on top of the binding column. The supernatant was poured onto the column stack and the clearing column discarded after all liquid passed through. The binding column was washed with 5 mL of endotoxin removal wash followed by 20 mL of column wash solution. After drying the membrane by applying a vacuum for 1 min it was incubated with 500 µL of water for 1min and the DNA eluted by applying a vacuum.

DNA concentration was determined using a Nanodrop system. HPLC water was used as blank and the absorption of 1 µL purified DNA at a wavelength of 260 nm (nucleic acids) and 280 nm (proteins) was measured. The DNA-concentration was calculated from the absorption using the formula of Lambert-Beer:

$$A = \varepsilon \times c \times d$$

Purity of the DNA was estimated using the ratio of Absorption at 260 nm and at 280 nm (A_{260}/A_{280}). A ratio ≥ 1.8 was required for the DNA to be used in further experiments.

Glycerol stock

To 500 µL of bacteria culture in LB medium 500 µL glycerol were added in a cryotube prior to storage at -80 °C. To grow bacteria part of the glycerol stock was transferred into a cell culture flask containing LB medium and the corresponding selection antibiotic prior to incubation overnight at 37 °C while shaking at 180 rpm.

Mammalian cell culture

Maintenance and growth of cells

For maintenance cells were incubated at 37°C and 5% CO_2. For immunoprecipitation and affinity purification HEK293 (CRL-1573-ATCC) cells were used, a fast growing human embryonic kidney cell line. For generation of knockouts and immunostaining hTERT-RPE1 cells (CRL-4000, ATCC) were used, a human retinal pigment epithelial cell line which upon serum starvation for 48 hours reliably develops good visible cilia which are submerged [23]. Cells were regularly checked for mycoplasma using an EZ-PCR Mycoplasma Detection Kit.

Passage of cells

When reaching a confluency between 80% and 100% medium was discarded and the cells washed with 10 mL PBS. Following PBS removal 1 mL trypsin EDTA was added and incubated for 5 min. Trypsin activity was stopped by adding 4 mL growth medium. Cells were resuspended and 1 mL of cell suspension transferred into a new 10 cm dish with 9 mL of growth medium prior to further maintenance as described above.

Freezing and thawing of cells

Prior to freezing cells were treated with trypsin and stopped as described in ‘passage of cells’ above. Cell suspension was transferred into a 15 mL tube prior to centrifugation for 3 min at 500 g at RT. Supernatant was discarded and the cell pellet resuspended in 1 mL of FBS with 10 % DMSO at 37 °C. Cells were cooled down in intervals: 15 min at 4°C, 1 hour at -20°C and for at least 1 hour at -80°C followed by storage at -180°C in liquid nitrogen.

For thawing the frozen cells were incubated in a water bath at 37°C before being rapidly transferred to a 15 mL tube with 10 mL of growth medium at 37°C. Following centrifugation at 500 g for 3 min at RT the supernatant was discarded and cells resuspended in 10 mL of growth medium before being transferred to a 10 cm dish and maintenance as described above.

Transfection of hTERT-RPE1 cells using Lipofectamine™ 3000

10^5 hTERT-RPE1 cells were seeded on coverslips in a 12-well plate. Following incubation for 4 h cells were transfected using lipofectamine™ 3000 according to manufacturer's protocol. For each well 2 µL of lipofectamine™ 3000 were added to 60 µL of DMEM to prepare a mastermix (A). In a separate reaction tube for each well a mixture of 60 µL of DMEM with 1,000 ng of DNA and 1 µL of P3000 was prepared (B). The corresponding volumina of A and B were mixed and incubated at RT for 10 min before being added to the seeded cells. After 24 hours of incubation the medium was changed to starvation medium and cells incubated and maintained as described above.

Transfection of HEK293 cells using Polyethylenimine (PEI)

$2x10^6$ HEK293 cells were seeded in 10 cm dish. For each dish 400 µL of PEI solution were mixed with 3,200 ng of DNA and incubated for 10 min at RT. The DNA-PEI solution was added to the cells by pipetting and incubated as described above.

Stable lines generation

HEK293 cells were grown in growth medium and transfected as described above before be subjected to a selection process for three weeks in 500 µM G418 condition for cells that stably integrated the expression construct.

Single clone selection

Cells were detached using trypsin EDTA and stopped as described in 'passage of cells' before being counted by using a counting chamber for Tecan™ instruments according to protocol. A total of 500 cells were seeded in a single 14 cm dish containing 20 mL growth medium. After incubation for 3-5 days the medium was discarded and cells washed with 20 mL of PBS at 37°C before adding10 mL of trypsin EDTA diluted 1:20 in PBS to softly detach cells. Colonies from a single clone were harvested under a microscope by taking up cells in a volume of 200 µL with a pipette. Cells from each clone were transferred into one well of a 24 well plate containing 1 mL of growth medium and subsequently incubated for several days. After reaching 50 % confluency cells were detached and transferred to a 10 cm dish. This step was performed as described in 'passage of cells' but with 200 µL of trypsin and 1 mL of growth medium for stopping.

Affinity Purification

Seeding of HEKT cells

From one 80% to 100 % confluent 10 cm dish cells were detached by treatment with 1 mL trypsin EDTA for 5 min. Trypsin activity was stopped by adding 4 mL growth medium and cells counted as described above. A total of $5x10^6$ cells were added to one 14 cm dish containing 20 mL growth medium before incubating for 2 days.

Cell Lysis and Bradford

After discarding medium cells were kept on ice and 1 mL of lysis buffer was added. Cell were detached from the dish using a cell-scraper and transferred to a 2 mL tube prior to incubation for 20 min at 4 °C while rotating. Cells were centrifuged for 10 min at 10,000 g and 4°C before transferring the supernatant into a new 2 mL tube and measuring the protein concentration using a Bradford assay.

For Bradford assay 20 µL of a 10x bovine-serum-albumin (BSA) solution (10 mg/mL) were diluted with 150 µL HPLC water and 6 calibration dilutions prepared as described below.

Table 7: Preparation of a BSA dilution row for Bradford-assay.

BSA concentration [mg/mL]	Used volume 1x BSA [µL]	Used volume water [µL]
0	0	50
0.2	10	40
0.4	20	30
0.6	30	20
0.8	40	10
1.0	50	0

To each calibration dilution 5.5 µL of lysis buffer were added. 5 µL of each dilution and 1 µL of each lysate were incubated with 195 µL of 1x Bradford solution for 5 min prior to measuring the absorbance at a wavelength of 595 nm in a Tecan™ Reader. Using the calibration row the protein concentration of the corresponding lysates was calculated.

Protein complex analysis by Strep affinity purification

For interactome identification HEK293 control and N-terminal Strep/FLAG-tagged protein construct expressing stable lines were used. Cells were lysed and the protein concentration was measured using Bradford assay as described above. A total protein amount of 5 mg for each sample was incubated with Strep-Tactin Superflow beads for 1 hour at 4°C while rotating at 35 rpm. The beads were washed three time with washing buffer and bound proteins eluted with Strep elution buffer. An acetone-based protein precipitation was performed followed by tryptic digest and desalting of digested proteins via stop-and-go extraction tips as described below and prepared for mass spectrometry (MS) analysis [78].

Co-immunoprecipitation by FLAG affinity purification

For validation of specific PPIs HEK293 cells stably expressing Strep/ FLAG -tagged IFT140 or RAF1 constructs were co-transfected with N-terminal HA-tagged TULP3 using homemade PEI solution. Cells were lysed and the protein concentration in the lysates measured as described above. ANTI-FLAG®-M2 Affinity Gel beads were prepared according to protocol and cell lysis and Bradford protein concentration measurement performed as described above. Following centrifugation, the supernatant was discarded and the beads transferred to a micro spin column. Beads were washed three times with 500 µL wash buffer and the supernatant discarded. To elute peptides the micro spin column was transferred to a new 2 mL reaction tube and beads incubated for 10 min with 200 µL of FLAG-peptide at RT. After a centrifugation at 1,000 g for 1 min at 4°C the beads were discarded and the eluates used for further analysis.

Protein Precipitation and tryptic digest

The protein solutions were filled up with 800 µL cold acetone to a final content of 80% acetone. The solution was mixed thoroughly by vortexing for 5 s and stored for 1h at -20°C. Subsequently protein solutions were centrifuged for 10 min at 10,000 g at 4°C. Following the centrifugation step the liquid phase was discarded and the protein pellet briefly air dried.

The precipitated and dried protein was resuspended in 30 µL ammonium bicarbonate (50 mM) and 4 µL RapiGest. The solution was vortexed and centrifuged down briefly before adding 1 µL DTT-solution (100 mM) and incubating on a Thermoblock for 10 min at 60°C. The mixture was cooled down to RT before centrifuging briefly and incubating for 30 min at RT in complete darkness with 1 µL IAA-solution (300 mM). Subsequently 0,5 µg of trypsin solved in 50mM acetic acid were added and samples incubated overnight at 37°C.

The following day samples were centrifuged for 1 min at RT and 9000 g. The enzymatic digest was stopped by adding 1.7 µL TFA to a final concentration of 5%. The solution was transferred to a PP Insert in a 1.5 mL Eppendorf tube and incubated for 10 min at RT prior to centrifugation at 25°C and 16,000 g for 15 min. The clear solution was transferred to a new 0.5 mL tube before proceeding with the desalting step.

Desalting with stop-and-go extraction tips (StageTips)

First the C18 StageTip matrix was equilibrated with 20 µL of 80/5 solution (80% ACN, 5% TFA) by pressing the solution through the matrix without letting the matrix run dry. After rinsing with 20 µL 0/5 (5% TFA) solution the sample was loaded onto the StageTip and washed with 20 µL 0/5 solution. The peptides were eluted into a 0.5 mL tube first with 20 µL 50/5 (50% ACN, 5% TFA) solution followed by a second step with 20 µL 80/5 solution before reducing the volume via SpeedVac at 37°C to a final volume of approximately 2-3 µL. 15 µL of 0,5% TFA were added to each sample and 8 µL transferred into a glass vial for MS-analysis.

Sample analysis using mass spectrometry

Mass spectrometry (MS) is an analytical method to determine the mass of ionized molecules. It is one of the central techniques in the field of proteomics and saw steady improvement over the last decades. Its key equipment is a mass spectrometer, which consists of three main components: an ion source and a mass analyser followed by an ion detector. Within a mass spectrometer ion are separated according to their mass/charge ratio (m/z) and detected [104].

One of the most used workflows is the bottom-up approach. Prior to MS analysis the proteins from a biological sample are cleaved into smaller peptides. The most commonly used protease is trypsin, a pancreatic serine protease, which cleaves peptide bonds after the basic amino acids lysine and arginine [105]. This results in short peptides with an average size of nine, which are suitable for chromatographic separation. The separation of the complex peptide mixture is usually achieved by liquid chromatography (LC), which can be directly coupled to an electrospray ionization (ESI) source where the peptides are ionized. The ionized peptides are subjected to an initial full scan of the precursor ion and the most abundant ions in each scan selected for peptide fragmentation. The analysis of the mass of the peptide fragments allows the determination of the amino acid sequence and subsequently their assignment to a protein using software tools and database searches as well as the quantification of their relative amounts [100,106].

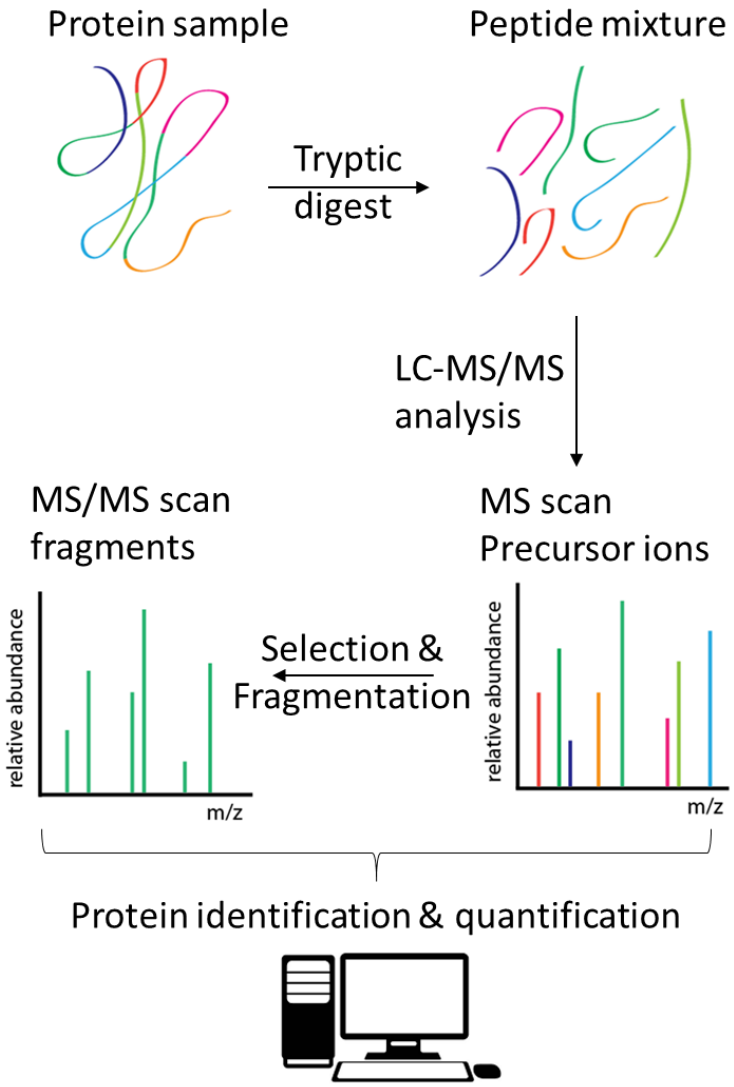

Figure 6: Experimental workflow for bottom-up proteomics. *Protein from a biological sample is digested into peptides using trypsin. The obtained peptides are separated using liquid chromatography and analysed via mass spectrometry. After a MS1 scan of the intact precursor ions the most abundant ions of each scan cycle are selected for further fragmentation. In the MS2 scan the mass to charge ratio of the resulting fragments is analyses. The combination of precursor and fragments mass to charge ratios allows the determination of the amino acid sequence of the analysed peptides by computational analysis using a database search.*

Data-dependent LC-MS/MS analysis

For LC-MS/MS analysis an Ultimate3000 nano-RSLC was coupled to a Orbitrap Fusion Tribrid by a nanospray ion source. Prepared peptide mixtures were loaded automatically onto a nano trap column (µ-Precolumn 300µm i.d. x 5 mm, packed with Acclaim PepMap100 C18, 5 µm, 100 Å; Dionex, USA). Injection was conducted with a flow rate of 30 µL/min in 98 % of buffer C (0,1 % TFA in HPLC-grade water) and 2 % of buffer B (80 % ACN, 0.08 % formic acid in HPLC-grade water) [78]. After 3 min peptides were eluted and separated on an analytical column (75 µm x 25 cm, packed with Acclaim PepMap RSLC, 2 µm, 100 Å; Dionex, USA) at a flow rate of 300 nL/min with a linear gradient from 2 % up to 30 % of buffer B in buffer A (2 % ACN,

0.1 % formic acid) for 82 min after an initial step of 3 min at 2 % buffer B. Remaining peptides were eluted with a steep gradient (30 % to 95 % in 5 min) followed by 5 min at constant 95 % of buffer B before the gradient was decreased rapidly in 5 min to 2 % of solvent B for the final 20 minutes [78]. In the data-dependent analysis full scan MS spectra were measured on the Orbitrap Fusion in a mass-charge range from m/z 335-1,500 with a resolution of 70,000. The ten most abundant precursor ions were selected with a quadrupole mass filter, if they exceeded an intensity threshold of 5.0 $x10^4$ and were at least doubly charged, for further fragmentation using higher energy collisional dissociation (HCD) set at a value of 30 followed by mass analysis of the fragments in the iontrap at a resolution of 120,000. Lock mass option was activated and the background signal with a mass of 445.12003 was used as mass lock. The selected ions were excluded for further fragmentation the following 20 s [78].

Lable free quantification using MaxQuant

MaxQuant software 1.6.1.0 [100] was used for label free quantification. Trypsin/P was used as a digestion enzyme with a maximum of 2 missed cleavages. Cysteine carbamidomethylation was set as fixed modification and methionine oxidations as well as N-terminal acetylation as variable modifications [78]. Minimum ratio count was set at 2 and the first search peptide tolerance at 20. Main search peptide tolerance was set at 4.5 ppm and the re-quantify option was selected. Current SwissProt database (release 2019_11) was used and contaminants detected by the MaxQuant contaminant search. A minimum of two peptides with at least one unique and one razor peptide was required with a minimum length of 7 amino acids for quantification. Match between runs was performed with a match time window of 0.7 min and an alignment window of 20 min [78].

Data analysis using Perseus

After uploading the LFQ intensities the rows of the generic matrix were filtered three times based on categorical column by site, reverse and potential contaminants and removing matching rows. LFQ intensities were transformed into $\log_2(x)$ replicates named according to the sample type by categorical annotation of rows. After filtering rows based on valid values only those which were present in more than half of the samples in at least one group were kept. Missing values were replaced by $\log_{10}(0)$ and a student's t-test performed with a permutation based FDR (p=0.05). The values were transformed by using the formula 2^x and groups averaged by applying the median. The main columns were combined according to the formula x/y with x being the sample of interest and y the negative control. Subsequently values were transformed again using $\log_2(x)$ and it was tested for outliers using a significance A outlier test.

Data analysis using R

Statistical analysis was performed using a custom-made R-script. A minimum of 6 biological replicates grown on individual seeded 14 cm dishes were used for statistics, including IFT140 wildtype and RAF1 control during each individual experiment [78]. Data were filtered for potential contaminants and peptides only identified by site and reverse database. For each gene comparison between mutants/RAF1 versus wildtype, at least half of the samples within one group needed to have valid values i.e. detected by the mass spectrometer. The means were compared using a student's t-test and p-values were corrected using the Benjamini-Hochberg method (q-values). The $\log_2$ ratios of each comparison were used to carry out the outlier significance A test. Proteins with a q <= 0.05 or a significance A value <= 0.05 were defined as significantly enriched/depleted [78].

Protein analysis

SDS-PAGE

Sodium-dodecylsulfate-polyacrylamide gel electrophoresis (SDS-PAGE) was used for the separation of proteins according to their molecular size. To protein lysates (50 µg total protein amount) or 10 µL eluate from co-immunoprecipitations the corresponding volume of 5x Laemmli-buffer was added and samples were heat shocked at 96°C for 2 min. Solutions for a stacking gel and a separation gel with 10% acrylamide were prepared as described below. TEMED and APS were added last, since they start the polymerization. The pouring stand was assembled according to the manufacturer, the separation gel solution added and isopropanol poured over the stacking gel to create a clear junction. After removal of the isopropanol the stacking gel solution was applied over the separation gel. The comb was inserted and the gel incubated for 10 min.

Table 8: Pipetting scheme for SDS-PAGE

Separation gel	**Volume in mL per gel**
Millipore water	4.0
Tris-HCl buffer (pH=8.8)	2.5
Acrylamide (30%)	3.3
SDS (10%)	0.1
Temed	0.02
APS (10%)	0.05
Separation gel	**Volume in mL per gel**
Millipore water	3.5
Tris-HCl buffer (pH=6.8)	0.7
Acrylamide (30%)	0.7
SDS (10%)	0.05
Temed	0.02
APS (10%)	0.05

The gel was inserted into an electrophoresis chamber, filled up with 1x running buffer and the comb removed. 5 µL of marker as well as the prepared protein samples were loaded to the slots. Electrophoresis was performed at a voltage of 80V until the front reached the separation gel before being increase to 120V till the front left the separation gel.

Immunostaining (Western Blot)

The gels from the SDS-PAGE were transferred to a PVDF-membrane via tank blotting. Separation gels, sponges and Whatman paper were incubated in 1x WB and PVDF membrane in methanol. 1x sponge, 2x Whatman paper, separation gel, PVDF membrane, 2x Whatman paper and 1x sponge were stacked up in a transfer frame. The fully assembled frame was inserted into an electrode module containing ice packs and the tank and blotting chamber filled up with 1x WB. An electric potential of 90V was applied for 1.5 hours to transfer the negatively charged SDS-protein complexes from the gel to the membrane, where they stick to due to hydrophobic and polar interactions.

Following the transfer to the PVDF membrane unspecific protein binding sites on the membrane were blocked by incubating the PVDF membrane for 1 hour in blocking solution (5% milk in 1x TBST) on a horizontal shaker at RT. The membranes were transferred to a wet-chamber and incubated with primary antibody solution overnight at 4°C while shaking. The following day the membrane was washed three times with 1x TBST, each time incubating 10 min at RT while shaking, before being incubated for 2 min with 800 µL of ECL solution in the dark. The chemo luminescense created by the reaction of horseradish peroxidase (HRP) with luminol was detected using a Fusion FX7 imaging system.

Intracellular immunofluorescence staining

Control and KO hTERT-RPE1 cells (CRL-4000, ATCC) were used for localization studies. A two-day serum free treatment was performed in 6-well plates to induce cilia formation. The medium was discarded and cells were fixed using 1 mL 4% PFA for 20 min at RT. After washing three times with PBS cells were permeabilized with 50 µL 0.3% PBST for 5 min at RT. Subsequently cells were blocked by applying 10% normal goat serum in 0.1% PBST for 1 hour, followed by primary antibody incubation with mouse ARL13B (1:100) and rabbit IFT140 (1:100) over night at 4°C. The following day cells were washed three times with PBS prior to incubation with secondary antibodies with goat α rabbit/mouse antibodies Alexa Fluor 488/568 (1:350). Finally, cells were mounted with 15 µL Fluoromount-G and examined via fluorescence microscopy.

Images were captured using a Zeiss Axio Imager Z1 ApoTome. The setup includes AxioCam MRm camera as well as 40x (NA 1.3) and 63x (NA 1.4) oil immersion objective lenses. Images were acquired as Z-stacks and processed using Zeiss ZEN 3.0 Blue Edition.

Results

Due to the importance of cilia for many biological processes, defects in genes coding for ciliary components can lead to a variety of diseases, which are commonly referred to as ciliopathies. Ciliopathies are a heterogeneous group of disease and mutations in one gene can lead to clinical phenotypes that vary in type and severity. The mechanisms underlying recessive Mendelian disease were studied with a focus on IFT-A, a protein complex important for retrograde transport of ciliary cargo. In this study four components of the IFT-A complex are examined for which disease-associated mutations have been reported. IFT43 and IFT121, also known as WDR35, from the peripheral subcomplex and IFT122 and IFT140 from the IFT-A core complex. IFT43 is the smallest of the four proteins, consisting of 208 amino acids and has a molecular weight of 24 kDa. It contains a region at its C-terminus that is evolutionary conserved between species. Little is known about the exact structure and function of IFT43. The fact that IFT43, in contrast to the other IFT-A components, is not found in all ciliated organisms indicates that its role in the complex is not essential [107]. The larger components IFT121 (132 kDa), IFT122 (142 kDa) and IFT140 (166 kDa) share several structural features. They consist of two N-terminal ß-propellers that are called WD40 domains, which commonly serve as interaction sites for binding of proteins. All these three proteins share a C-terminal TPR domain, a sequence of α-helices that mediate contact between the components of the complex [29,30,108]. IFT121 and IFT122 both possess a RING domain and IFT122 in addition a Zinc finger domain [109]. Both domains can bind zinc cations as well as other ions and RING domains play a central role in protein ubiquitination. The Zinc finger domain found in IFT122 is a subtype of the RING domain. It lacks several helical structures and cannot promote ubiquitination but e.g. can bind to DNA [110,111].

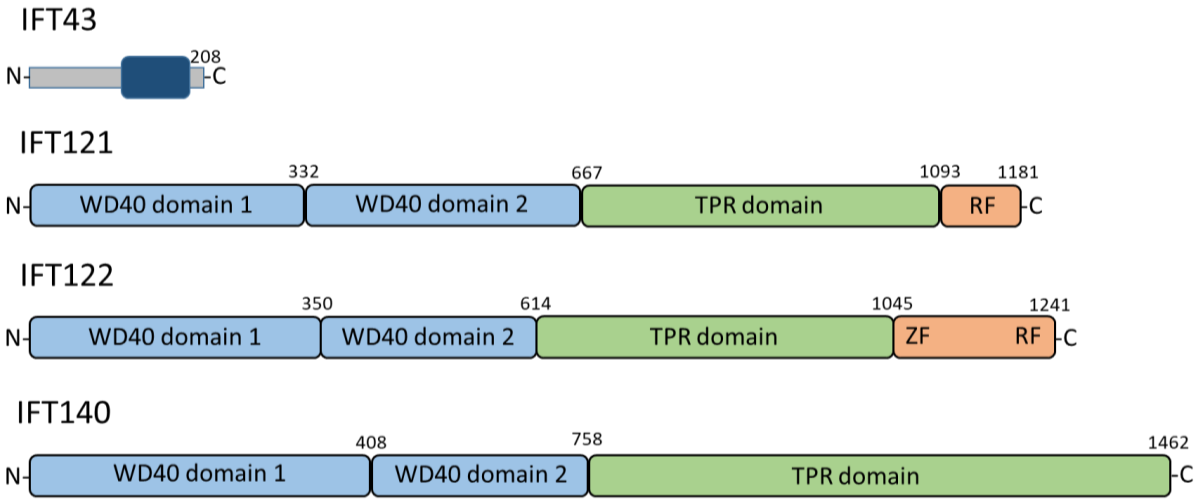

Figure 7: Domain structure of four IFT-A components. *Domain diagrams for IFT43, IFT121, IFT122 and IFT140 are shown. The evolutionary conserved region in IFT43 is indicated (dark blue). WD40 domains are shown (light blue) as well as TPR domains (green). Indicated in orange are the C-terminal RING (RF) and Zinc finger (ZF) domains in IFT121 and IFT122.*

Experimental Setup

To examine the effects of disease-associated missense mutations on protein interaction networks affinity purification coupled to LC-MS/MS was used. After cloning genes coding for four IFT-A components (IFT43, IFT121, IFT122 and IFT140) from cDNA [112] ciliopathy-associated missense mutations reported for these genes were collected. Via site-directed mutagenesis these mutations were introduced into wildtype constructs. Using Gateway cloning plasmids expressing IFT-A wildtype and mutant protein fused to a N-terminal Strep/ FLAG tag were generated as well as HEK293 cell lines stably expressing the desired constructs. A Strep affinity purification was performed with lysates from cells stably expressing wildtype and mutant constructs or RAF1 as negative control. Following affinity purification a protein precipitation as well as a tryptic cleavage were performed prior to LC-MS/MS analysis of the obtained peptides. Label free quantification of the spectral peaks from the obtained peptides was performed using MaxQuant and followed by statistical analysis using R. In a first step the interactome of IFT-A wildtype proteins was determined using RAF1 as a negative control. In a second step the impact of the ciliopathy-associated missense mutations on the wildtype interactors was assessed. Significant parts of the data presented and discussed in this work have been published as a manuscript by the author and are publicly available [78].

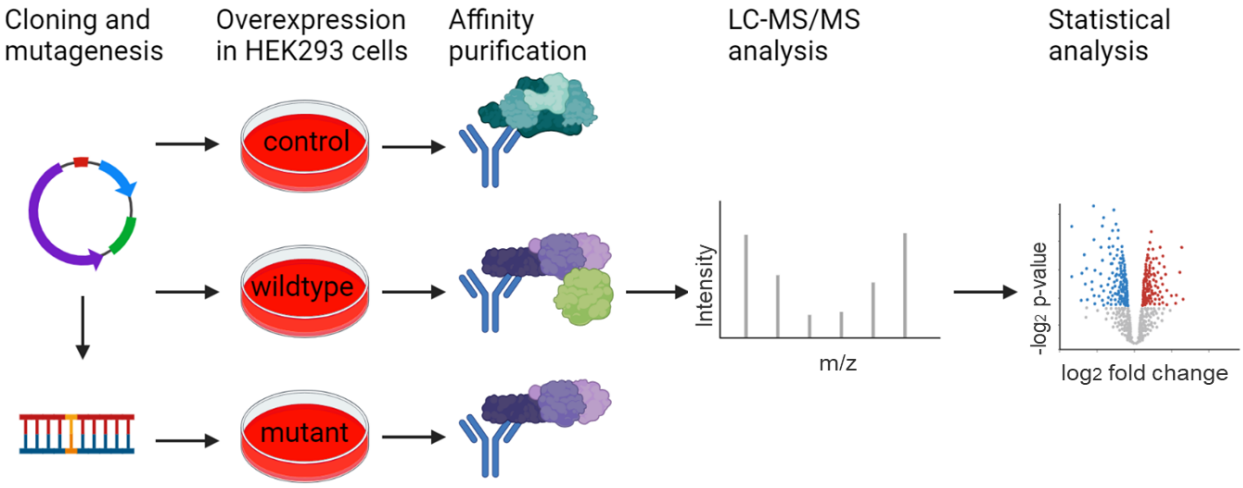

Figure 8: Experimental workflow. *For interactome analysis HEK293 cells stably overexpressing IFT-A wildtype or mutant constructs or RAF1 as negative control fused to a N-terminal Strep/FLAG-tag were used. Cells were grown to 80%-100% confluency and lysed followed by Strep affinity purification. A protein precipitation followed by tryptic cleavage was performed with the eluates prior to analysis via mass spectrometry. MaxQuant was used for label free quantification and a R script for statistical analysis. Graphics made with biorender.com.*

Identification of the IFT43 wildtype interactome

To gain further insight into the PPIs of wildtype IFT43 (IFT43 WT) affinity purification coupled to LC-MS/MS analysis was performed. Using HEK293 cells stably expressing IFT43 WT or RAF1 as negative control, both N-terminal fused to a Strep/FLAG-tag, a Strep affinity purification was performed. After LC-MS/MS analysis and label free quantification the interactome of wildtype IFT43 was determined. Using a total of six biological replicates from two separate experiments a robust dataset for statistical analysis was obtained. The label free quantification was done using the MaxQuant software and statistics were calculated using R. Proteins were classified as interactors if they were enriched with a student's t-test p-value < 0.05 and significance A value < 0.05 in the IFT43 WT samples as compared to the RAF1 control. Figure 9 shows a scatter plot representing the proteins retrieved, and proteins that are enriched following IFT43 pulldown are labelled [78].

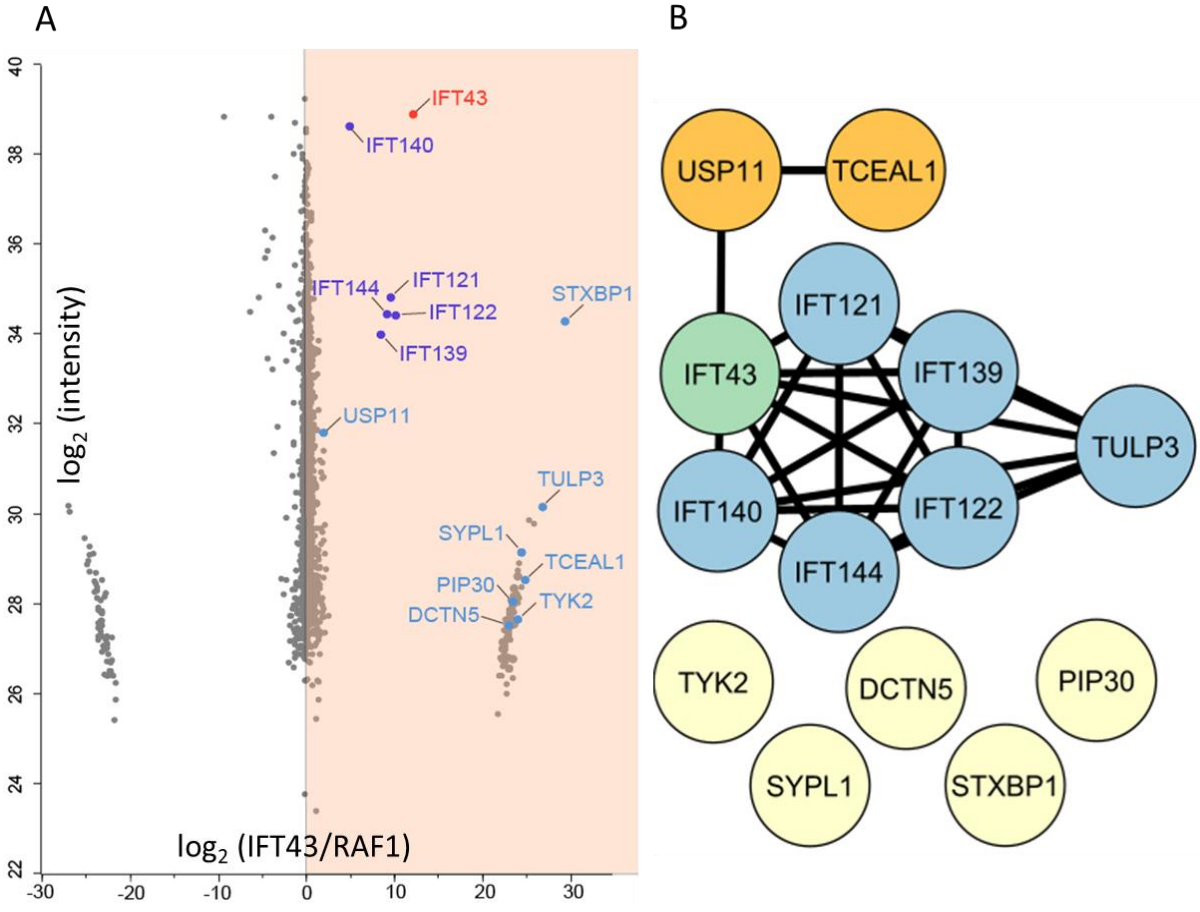

Figure 9: ***Identification of the IFT43 wildtype interactome****. (A) Using Strep affinity purification with lysates from HEK293 cells stably overexpressing IFT43 WT or RAF1 as negative control fused to a N-terminal Strep/FLAG-tag, the protein interactome of IFT43 was determined. Mass spectrometric identification and label free quantification of the detected peptides was performed using MaxQuant. Statistical analysis (n=6) was done using R (student's t-test: p<0.05; Significance A: p<0.05) and the log₂ ratios of IFT43 vs. RAF1 calculated and plotted. (B) A protein interaction analysis for the identified interactors was performed using the STRING database. In addition to all components of the IFT-A complex alsothe ciliary protein TULP3 was identified, confirming the suitability of our approach to detect interaction partners of IFT43. In total eight proteins, which are not part of the IFT-A complex, were identified as potential interactors. Proteins are coloured according to protein interaction clusters.*

***Table 9*: Enriched proteins in the IFT43 wildtype affinity purification.** *For the analysis of the IFT43 protein-protein interaction a Strep affinity purification was performed (n=6). RAF1 was used as a negative control. Mass spectrometric identification and label free quantification of the detected peptides was performed using MaxQuant. Statistical analysis was done using R and the log_2 ratios were calculated (IFT43/RAF1). Ratios as well as statistical significance (*=p<0.05; **=p<0.01; ***=p<0.001) from student's t-test and significance A and known functions of potential interactors are shown. Genes are sorted according to interaction clusters and log_2 ratios.*

Gene name	log_2 ratio (IFT43/RAF1)	student's t-test	Signifi-cance A	Protein function
IFT43 (bait)	12.13	**	***	IFT-A peripheral complex [30]
TULP3	26.81	***	***	Negative regulation of Shh-signaling [35,36]
IFT122	24.78	**	***	Transcriptional regulation [113]
IFT121	24.42	***	***	Regulation of cell proliferation [114]
IFT144	24.02	***	***	Regulation of cell proliferation [115]
IFT139	23.37	***	***	Regulation of protein degradation [116]
IFT140	23.05	***	***	unknown
TCEAL1	24.78	**	***	Transcriptional regulation [113]
USP11	1.88	***	**	Regulation of protein degradation [117]
STXBP1	29.41	***	***	Synaptic vesicle docking [118]
SYPL1	24.42	***	***	Regulation of cell proliferation [114]
TYK2	24.02	***	***	Regulation of cell proliferation [115]
PIP30	23.37	***	***	Regulation of protein degradation [116]
DCTN5	23.05	***	***	unknown

14 proteins were found as enriched in our experiments (figure 9 and table 9), including all six components of the IFT-A complex [30] and TULP3, which is associated to the IFT-A complex [35,36]. Network analysis using STRING (https://string-db.org/) revealed an interaction cluster associated with IFT-A consisting of two proteins. USP11 interacts with IFT-A and is involved in the regulation of protein degradation via the proteasome [117]. TCEAL1 is a known interactor of USP11 and a transcriptional regulator [113]. In addition, five proteins have been identified as potential novel interactors of IFT43. STXBP1 is a protein involved in docking of synaptic vesicles [118]. The proteins SYPL1 and TYK2 are both regulators of cell proliferation and survival [114,115]. PIP30 has a role in targeting proteins for proteasomal degradation, similar to USP11 [116]. The function of DCTN5 is so far unknown.

Selection of a missense mutation in IFT43 that causes Jeune syndrome and campomelia

From a previous publication one missense mutations in IFT43 reported from a patient affect by a ciliopathy was selected. The reported patient was diagnosed with Jeune syndrome with thoraxic dysplasia and campomelia (table 10) and harbours a homozygous W179R mutation in a region of IFT43 that in conserved across species [107] (figure 10). For analysis of the changes in PPIs caused by ciliopathy-associated missense mutations HEK293 stable lines expressing IFT43 WT or W179R mutant construct with a N-term Strep/ FLAG -tag were generated.

Table 10: Missense mutatios in IFT43 and corresponding clinical phenotype. *From previous publications one homozygous missense mutations reported from a patient suffering from a ciliopathy (Jeune syndrome with thoraxic dysplasia and campomelia) was collected. The allelic combination and the reported clinical phenotype are shown.*

Mutation	Second allele	Phenotype	Publication
p. W179R	p. W179R	JATD + campomelia	107

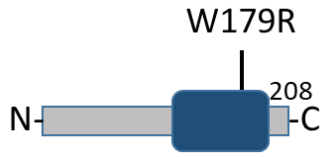

Figure 10: Domain diagram of IFT43 with mutations. *A domain diagram for IFT43 is shown. The evolutionary conserved C-terminal region is indicated in blue. The position of the ciliopathy-associated missense mutation in the domain diagram is indicated.*

The disease-associated W179R mutation in IFT43 disturbs the interaction with IFT-A and TULP3

To analyse the IFT43 protein interactome and the changes induced by the ciliopathy-associated mutation affinity purification followed by LC-MS/MS was performed with the generated HEK293 stable lines [78]. After label free quantification the potential interaction partners were first filtered for stable interactors of WT IFT43. In a second step the ratio of these interactors was evaluated for quantitative changes in the mutant compared to the WT. Through the statistical analysis of six replicates each using stringent statistical filters (student's t-test p-value <0.05 and Significance A p-value <0.05) robust and reproducible results were obtained (figure 11) [78].

The W179R data was plotted against IFT43 WT and the wildtype interactors of IFT43 were labelled (figure 11). The abundance of the bait protein IFT43 was comparable in the wildtype and the mutant. However, the binding of all five remaining components of the IFT-A complex was slightly reduced in the W179R mutant as compared to the IFT43 WT. Seven out of 14 of

the IFT43 WT interactors were unaffected by the W179R mutation. This includes the proteins DCTN5, PIP30, STXBP1, SYPL1, TCEAL1, TYK2 and USP11. The binding of TULP3 is strongly reduced in the W179R mutant as compared to the IFT43 WT.

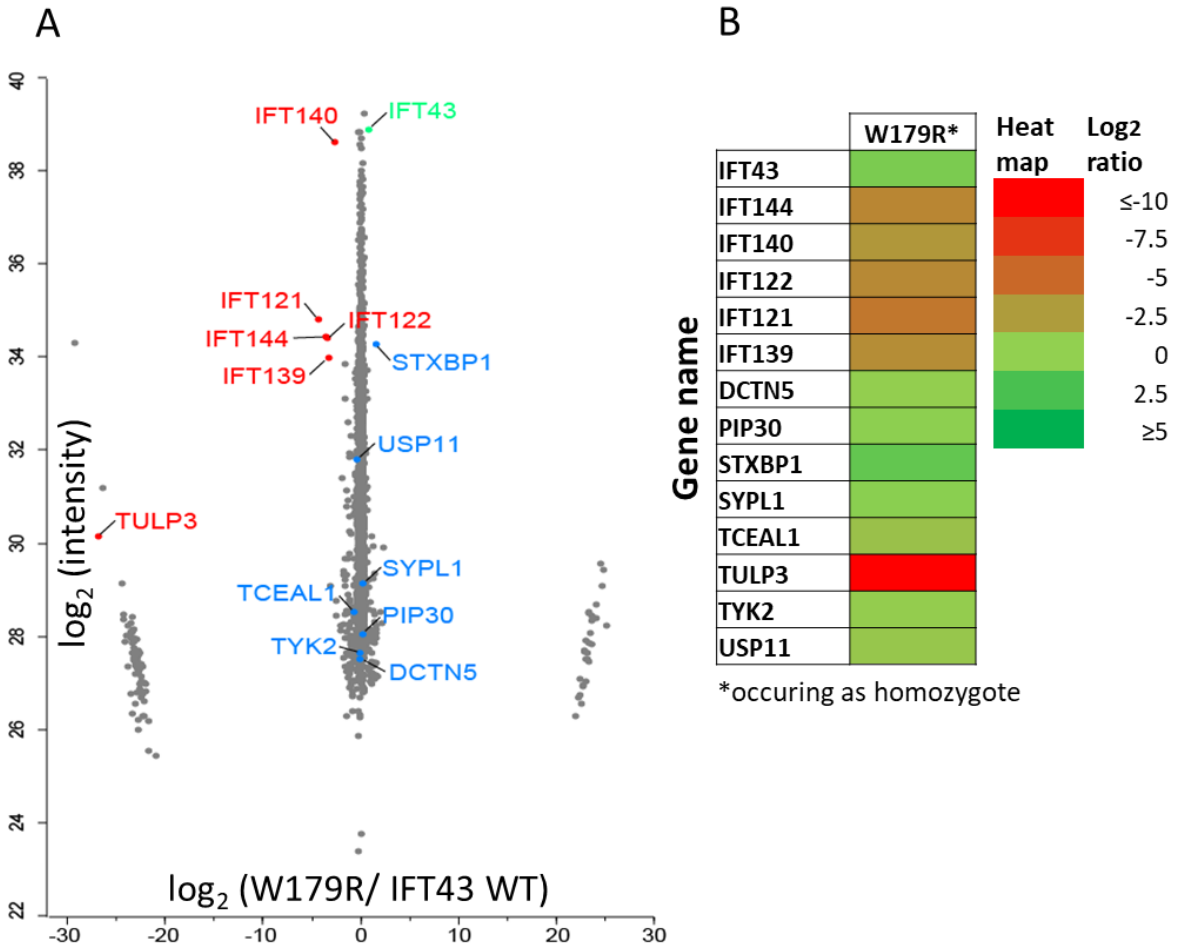

Figure 11: IFT43 missense mutation impacts protein interaction networks. *For one ciliopathy-associated missense mutation in IFT43 the changes affecting interaction partners of wildtype IFT43 were assessed. Strep affinity purification was used with lysates from HEK293 cells stably overexpressing IFT43 wildtype or mutant construct fused to a N-terminal Strep/FLAG-tag. Mass spectrometric identification and label free quantification of the detected peptides was performed using MaxQuant. Statistical analysis was performed using R. The log_2 ratios of mutant vs. wildtype were calculated and are shown in a scatter plot (A) and a heat map (B) for the W179R mutation. Log_2 ratios of 0 indicate similar abundance of the protein in wildtype and mutant conditions, while log_2 ratios <0 indicate reduced protein levels in mutant samples as compared to wildtype* [78].

To assess if similar effects of disease-associated mutations on protein interaction networks are observed for other proteins another component of the IFT-A complex was to be analysed. Since IFT43 is a small component of the IFT-A peripheral subcomplex and not found in all ciliated organisms [107] it was continue with IFT121, a larger component of the same subcomplex, which shows a higher degree of evolutionary conservation between species [28,96].

Analysis of the IFT121 wildtype interactome reveals known and novel interactors

After analysing the interactome of IFT43 and the effect of a disease-associated missense mutation on its protein interactions it was continued with another component of the IFT-A peripheral subcomplex. IFT121, also known as WDR35, is a component of IFT-A, which facilitates the retrograde trafficking of cargo within the cilium [29,30]. In contrast to IFT43, which is not present in several ciliated organisms [107], IFT121 is an essential part of the complex. It shares several structural features with other IFT-A component. This includes two N-terminal ß-propellers called WD40 domains, which commonly serve as binding sites for protein interactions. On the C-terminus IFT121 contains a TPR domain, which mediates contact with other components of the IFT-A complex [29] as well as a RING finger domain. The analysis of the wildtype interactome and the effect of disease-associated missense mutations was done as described for IFT43. Figure 12 shows a scatter plot representing the proteins retrieved, and proteins that are enriched following IFT121 pulldown are labelled.

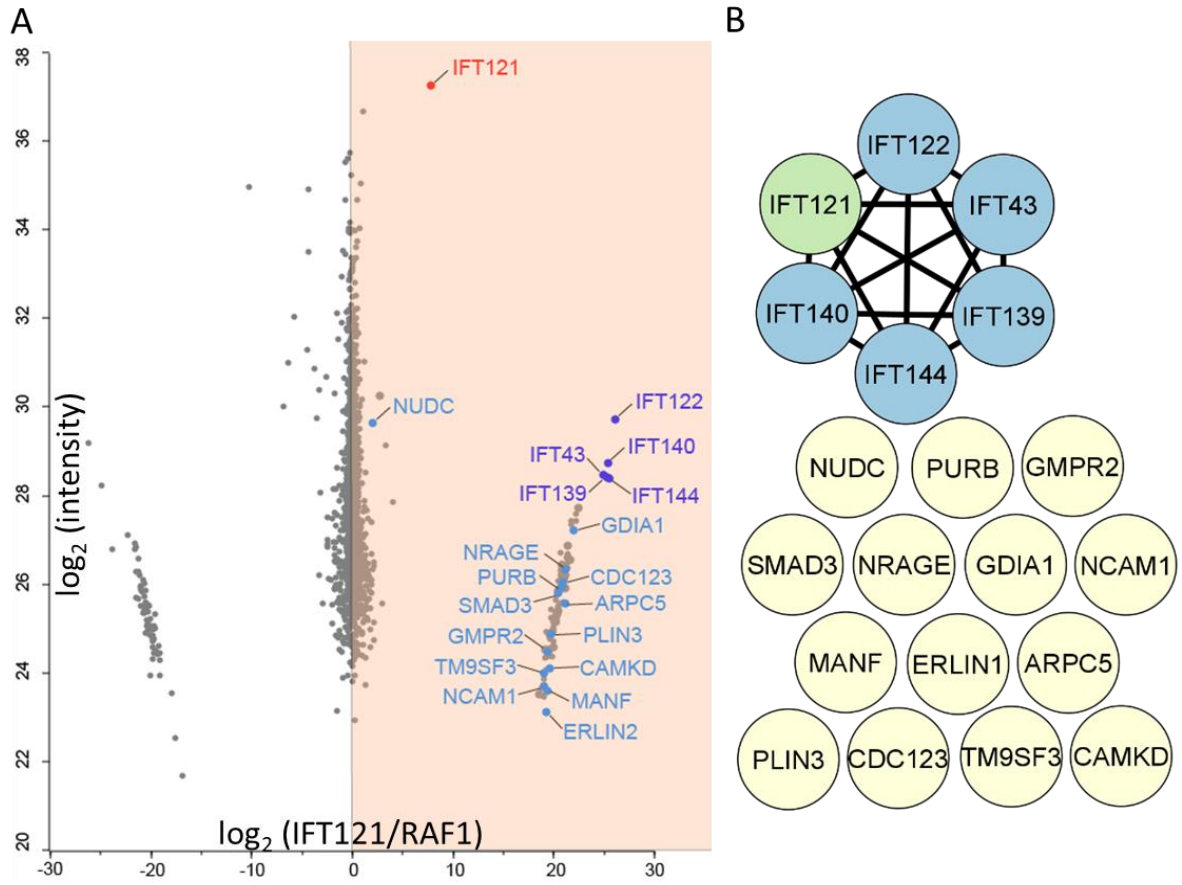

Figure 12*: Identification of the IFT121 wildtype interactome.* *(A) Using Strep affinity purification with lysates from HEK293 cells stably overexpressing IFT121 WT or RAF1 as negative control fused to a N-terminal Strep/FLAG-tag, the protein interactome of IFT121 was determined. Mass spectrometric identification and label free quantification of the detected peptides was performed using MaxQuant. Statistical analysis (n=6) was done using R (student's t-test: p<0.05; Significance A: p<0.05) and the log_2 ratios of IFT121 vs. RAF1 were calculated and plotted. (B) A protein interaction analysis for the identified interactors was performed using the STRING database. In addition to all components of the IFT-A in total 14 proteins, which are not part of the IFT-A complex, were identified as potential interactors. Proteins are coloured according to protein interaction clusters.*

***Table 11: Enriched proteins in the IFT121 wildtype immunoprecipitation**. For analysis of the IFT121 protein-protein interaction a Strep affinity purification was performed (n=6). RAF1 was used as a negative control. Mass spectrometric identification and label free quantification of the detected peptides was performed using MaxQuant. Statistical analysis was done using R and the log_2 ratios were calculated (IFT121/RAF1). Ratios as well as statistical significance (*=p<0.05; **=p<0.01; ***=p<0.001) from student's t-test and significance A and known functions of potential interactors are shown. Genes are sorted according to interaction clusters and log_2 ratios.*

Gene name	log_2 ratio (IFT121/RAF1)	student's t-test	Signifi-cance A	Protein function
IFT121 (bait)	7.85	*	***	IFT-A peripheral complex [30]
IFT122	26.05	**	***	IFT-A core complex [30]
IFT139	25.46	***	***	IFT-A peripheral complex [30]
IFT140	25.35	**	***	IFT-A core complex [30]
IFT144	25.29	***	***	IFT-A core complex [30]
IFT43	24.89	***	***	IFT-A peripheral complex [30]
ARHGDIA	21.94	***	***	Regulation of Rho signaling [119]
SMAD3	21.14	***	***	Regulation of TGF-beta signaling [77]
MAGED1	21.10	*	***	Inhibition of cell cycle progression [120]
CDC123	20.95	*	***	Cell cycle regulation [121]
PURB	20.82	*	***	Transcriptional regulation [122]
ARPC5	20.38	*	***	Actin cytoskeleton regulation [123]
PLIN3	19.77	***	***	Formation of lipid droplets [124]
TM9SF3	19.60	*	***	Localization of transmembrane domains [125]
GMPR2	19.36	***	***	Cell differentiation [126]
NCAM1	19.31	*	***	Neural cell adhesion [127]
ERLIN1	19.28	*	***	Regulation of cellular cholesterol [128]
CAMK2D	19.06	*	***	Calcium influx and histone deacetylation [129]
MANF	19.00	*	***	Inhibition of cell proliferation [130]
NUDC	1.96	***	**	Spindle formation and microtubule organization, protein folding [108,131,132]

20 proteins were found to be enriched in our data (figure 12 and table 11), including all components of the IFT complex A. Besides the IFT-A complex itself, 14 novel potential interactors of IFT121 were enriched, which are not listed in the intact-database so far (www.ebi.ac.uk). This includes regulators of signaling pathways such as SMAD3 (TGF-beta signaling [77]) and ARHGDIA (Rho signaling), which is linked to nephrotic syndrome via defective RHO GTPase signaling [119]. Several regulators of cell cycle progression have been identified, namely MAGED1 (Inhibition of cell cycle progression [120]), CDC123 (Cell cycle regulation [121]) and MANF (Inhibition of cell proliferation [130]). Other enriched proteins are involved in the regulation of transcription (PURB [122]) or the actin cytoskeleton (ARPC5 [123]). PLIN3 is involved in the formation of lipid droplets [124], while ERLIN1 regulates cellular cholesterol levels [128].

GMPR2 is involved in cell differentiation [126] and NCAM1 required for neural cell adhesion [127]. TM9SF3 enables proper localization of transmembrane proteins [125] and CAMK2D regulates the influx of calcium ions into the cell and regulates the activity of the histone deacetylase HDAC4 [129]. NUDC is involved in spindle formation during mitosis and in microtubule organization during cytokinesis[108,131] and also serves as co-chaperone for proper protein folding [132].

Selection of missense mutations in IFT121 from patients suffering from Sensenbrenner

From previous publications four missense mutations in IFT121 found in patients affect by a ciliopathy were gathered (table 12). The mutations S168R and D841V occur as compound heterozygotes in combination with a L641* mutation. The mutations Y971C and W1153C both occur as homozygotes. These mutations are located in the first WD40 domain as well as the TPR repeats and the RING domain (figure 13). All four mutations are associated with Sensenbrenner in affected patients. For analysis of the PPIs of all four mutations HEK293 stable lines expressing IFT121 WT or ciliopathy-related mutant constructs with a N-term Strep/FLAG-tag were generated.

Table 12 Missense mutations in IFT121 and corresponding clinical phenotype. *From previous publications a list of four missense mutations reported from patients suffering from ciliopathies and harbouring missense mutations in both alleles of IFT121 were gathered. For each patient the allelic combination and the reported clinical phenotype is shown.*

Mutation	Second allele	Phenotype	Publication
p. S168R	p. L641*	Sensenbrenner	96
p. D841V	p. L641*	Sensenbrenner	97
p. Y971C	p. Y971C	Sensenbrenner	96
p. W1153C	p. W1153C	Sensenbrenner	95

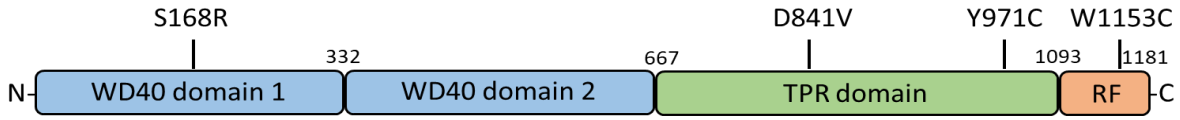

Figure 13: Domain diagram of IFT21 with mutations. *A domain diagram for IFT121 is shown. The different domains are indicated (WD40 in blue; TPR-repeats in green; RING finger domain in orange). The positions of the ciliopathy-associated missense mutations in the domain diagram are indicated.*

Ciliopathy-associated IFT121 missense mutations cause interactome changes

The IFT121 protein interactome and the changes induced by ciliopathy-associated mutations were analysed by affinity purification followed by LC-MS/MS as described above. Stable interactors of WT IFT121 were determined and the ratio of these interactors was evaluated for quantitative changes in the mutants compared to the WT. Through the statistical analysis of six replicates each using stringent filtering (student's t-test p-value <0.05 and Significance A p-value <0.05) robust results for statistical analysis were obtained (figure 14) [78].

The binding of the bait protein IFT121 is slightly reduced in three out of four mutants (S168R, Y971C and W1153C) and to a stronger extent in the D841V mutation as compared to the WT. The D841V mutation shows a strong disruption of all five IFT-A components. In the other three mutations (S168R, Y971C and W1153C) the binding of IFT140 is slightly reduced. While IFT122 is reduced in S168R and D841V it is unaltered in Y971C and W1153C. IFT144 is strongly reduced in S168R and D841V and slightly reduced in Y971C as well as in W1153C. IFT139 is strongly reduced in D841V and slightly reduced in the other three mutations (S168R, Y971C and W1153C). IFT43 is unaltered by the S168R mutation, slightly reduced in the D841V and W1153C mutation and strongly reduced in the Y971C mutation.

The proteins ARHGDIA and NUDC are unaltered in all four mutants. ARPC5 is reduced in one out of four mutants (Y971C) and CAMK2D in three out of four (D841V, Y971C and W1153C). CDC123 is strongly reduced in three out of four mutants (S168R, D841V and Y971C) and unaltered in W1153C, while ERLIN1 is strongly reduced in all four mutants. GMPR2 is strongly reduced in one out of four mutants (S168R). MAGED1 is strongly reduced in one out of four mutants (W1153C) and slightly reduced in two out of four (S168R and D841V). MANF is strongly reduced in three out of four mutants (S168R, Y971C and W1153C) and unaltered in D841V. NCAM1 is strongly reduced in two out of four mutants (D841V and Y971C) and slightly reduced in W1153C, while being unaltered in S168R. PLIN3 is strongly reduced in one mutant (D841V) and unaltered in three out of four (S168R, Y971C and W1153C). PURB is strongly reduced in three out of four mutants (S168R, D841V and W1153C) and unaltered in Y971C. SMAD3 is strongly reduced in two out of four mutants (S168R and D841V) and unaltered in the other two (Y971C and W1153C). TM9SF3 is strongly reduced in two out of four mutants (S168R and Y971C) and unaltered in the other two (Y971C and W1153C).

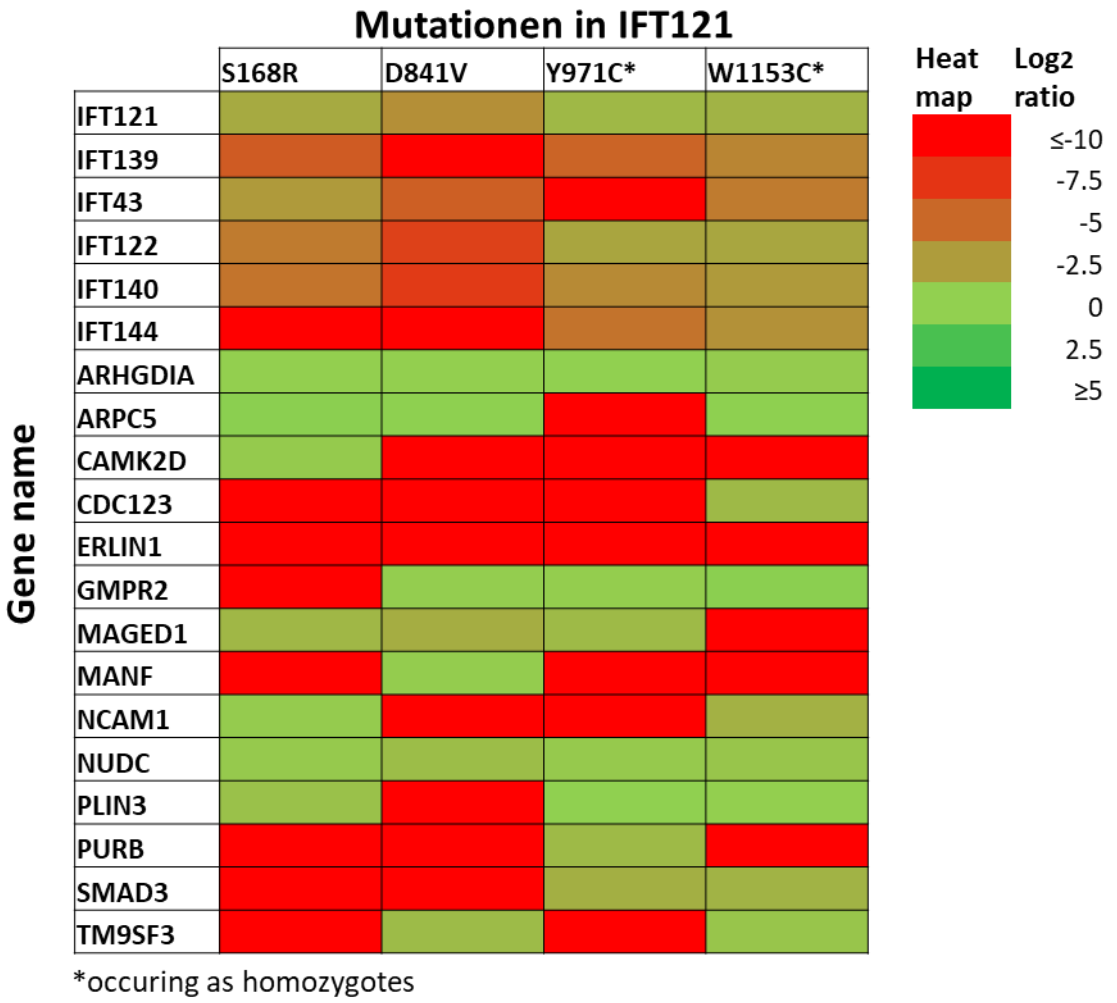

***Figure 14**: **IFT121 missense mutations impact protein interaction networks**. For four ciliopathy-associated missense mutations in IFT121 the changes affecting interaction partners of wildtype IFT121 were assessed. Strep affinity purification was applied with lysates from HEK293 cells stably overexpressing IFT121 wildtype or mutant construct fused to a N-terminal Strep/FLAG-tag. Mass spectrometric identification and label free quantification of the detected peptides was performed using MaxQuant. Statistical analysis was performed using R, the log_2 ratios of mutant vs. wildtype calculated and are shown in a heat map for eight missense mutations. Log_2 ratios of 0 indicate similar abundance of the protein in wildtype and mutant conditions, while log_2 ratios <0 indicate reduced protein levels in mutant samples as compared to wildtype. Mutations are sorted from left to right according to their position in the protein from N- to C-terminal direction.*

The analysis of the WT interactome of two components of the IFT-A peripheral subcomplex (IFT43 and IFT121) revealed several new potential protein interactions. The analysis of the impact on protein interaction networks of disease-associated missense mutations showed a disruption of specific protein interactions. In both IFT43 and IFT121 the missense mutations reduce the integrity of the IFT-A complex. No complete disruption of the complex composition was observed, but rather a quantitative effect that differs between different mutations. After analyzing components of the IFT-A peripheral complex the next aim was the analysis of components of the IFT-A core complex.

Several protein complexes are associated to IFT-A core component IFT122

The mass spectrometric analysis of the wildtype interactome of two components of the IFT-A peripheral complex (IFT43 and IFT121) revealed several novel protein interactions. The introduction of several disease-associated missense mutations led to the disruption of specific protein interactions as well as impairing the integrity of the IFT-A complex in comparison to the wildtype forms. In a next step the wildtype interactome of IFT122 was analysed, a component of the IFT-A core complex [29,30]. IFT122 shows a structure similar to IFT121. It contains two ß-propellers (WD40 domains) at the N-terminal end as well as a TPR domain, which mediates contact with other components of the IFT-A complex. While IFT121 only exhibits a RING finger domain at the C-terminal end, IFT122 in addition to the RING- also contains a Zinc finger domain. Both domains can bind zinc cations and can serve varying biological functions such as ubiquitination [109,110]. Figure 15 shows a scatter plot representing the peptides retrieved, and proteins that are enriched following IFT122 pulldown are labelled.

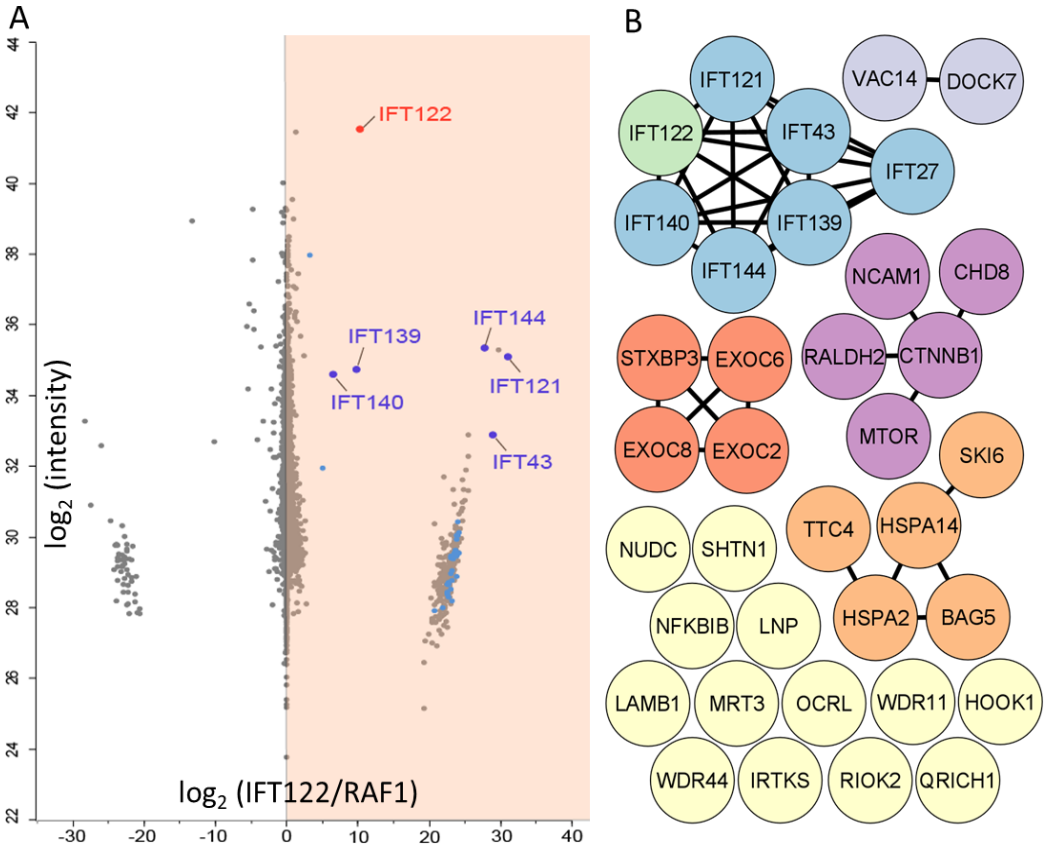

***Figure 15: Identification of the IFT122 wildtype interactome**. (A) Using Strep affinity purification with lysates from HEK293 cells stably overexpressing IFT122 WT or RAF1 fused to a N-terminal Strep/FLAG-tag, the protein interactome of IFT122 was determined. Mass spectrometric identification and label free quantification of the detected peptides was performed using MaxQuant. Statistical analysis (n=12) was done using R (student's t-test: p<0.05; Significance A: p<0.05) and the log_2 ratios of IFT122 vs. RAF1 were calculated and plotted. (B) A protein interaction analysis for the identified interactors was performed using the STRING database. In addition to all components of the IFT-A complex also parts of the IFT-B complex (IFT27) were identified. In total 30 proteins, which are not part of the IFT-A complex, were identified as potential interactors. Proteins are coloured according to protein interaction clusters.*

Table 13 Enriched proteins in the IFT122 wildtype affinity purification. *For the analysis of the IFT122 protein-protein interaction a Strep affinity purification was performed (n=12). RAF1 was used as a negative control. Mass spectrometric identification and label free quantification of the detected peptides was performed using MaxQuant. Statistical analysis was done using a R script and the log_2 ratios were calculated (IFT122/RAF1). Ratios as well as p-values from the statistical analysis and known functions of potential interactors are shown. Genes are sorted according to interaction clusters and their log_2 ratios.*

Gene name	log_2 ratio (IFT122/RAF1)	student's t-test	Significance A	Protein function
IFT122 (bait)	10.32	***	***	IFT-A core complex [30]
IFT121	31.01	***	***	IFT-A peripheral complex [30]
IFT43	28.81	***	***	IFT-A peripheral complex [30]
IFT144	27.73	***	***	IFT-A core complex [30]
IFT27	24.00	***	***	IFT-B complex [34,66]
IFT139	9.84	***	***	IFT-A peripheral complex [30]
IFT140	6.48	***	***	IFT-A core complex [30]
HSPA14	24.21	***	***	Protein folding [133]
TTC4	24.01	**	***	Protein folding [134]
SKI6	23.04	***	***	Exosome complex [135]
HSPA2	23.00	***	***	Protein folding [136]
BAG5	4.96	**	***	Protein folding [137]
RALDH2	24.13	**	***	Generation of retinoic acid [138]
MTOR	23.83	*	***	Regulation of cell growth and survival [99,139]
NCAM1	23.77	***	***	Brain development [127]
CTNNB1	22.96	***	***	Canonical Wnt signaling [140,141]
CHD8	22.56	***	***	Regulation of Wnt-signaling [142]
EXOC2	23.35	**	***	Exocyst component; brain development [143]
STXBP3	22.66	*	***	Docking of GLUT4 [118]
EXOC8	22.50	***	***	Exocyst component [143]
EXOC6	20.71	**	***	Exocyst component [143]
DOCK7	23.45	***	***	Axon formation [144]
VAC14	23.10	**	***	Endosome transport [145]
SHTN1	23.82	***	***	Axon growth [146]
LAMB1	23.78	***	***	Brain development [147]
HOOK1	23.71	***	***	Vesicle trafficking [148]
MRT3	23.61	***	***	Centrosome organization
NFKBIB	23.42	*	***	Inhibition of NF-κB [149]
IRTKS	23.24	***	***	Organization of actin cytoskeleton
RIOK2	23.13	**	***	Regulation of mitosis [150]
QRICH1	23.09	***	***	Bone growth(longitudinal) [151]
LNP	22.76	**	***	Nervous system development [152]
WDR44	22.60	***	***	Vesicle recycling
WDR11	22.51	*	***	Hedgehog signaling and ciliogenesis [137]
OCRL	21.94	***	***	Primary cilia assembly [153]

NUDC	3.17	***	**	Spindle formation and microtubule organization; protein folding [108,131]

36 proteins were enriched in the experiments (figure 15 and table 13), including all six components of the IFT-A complex as well as IFT27, which is part of the IFT-B core complex. Network analysis using STRING (https://string-db.org/) revealed four additional interaction clusters among the enriched proteins (figure 15). One of them is a cluster of the five proteins CTNNB1, MTOR, RALDH2, CHD8 and NCAM1. CTNNB1 is the central effector protein of the canonical Wnt-signaling pathway, which plays a crucial role during embryogenesis among other processes [140,141]. CHD8 is also involved in Wnt signaling as negative regulator [142]. RALDH2 is involved in the generation of retinoic acid [138]. NCAM1 is important for proper brain development [127] and MTOR crucial for the control of cell growth and survival [99,139]. The third interaction cluster includes the two proteins VAC14 and DOCK7. While VAC14 participates in endosome transport [145] DOCK7 is important for axon formation [144]. The fourth cluster involves the four proteins STXBP3, EXOC2, EXOC6 and EXOC8. The latter three are exocyst components and EXOC2 has also been shown to be important for brain development [143]. STXBP3 is crucial for the membrane docking of the GLUT4 receptor [118]. The fifth interaction cluster includes the five proteins HSPA2, HSPA14, BAG5, SKI6 and TTC4. All protein are chaperones involved in protein folding [134,136,137], except SKI6, which is part of the exosome complex [135]. The 13 other proteins are not part of any known interaction cluster. Among them is NUDC, which is important for microtubule organization during spindle formation and for protein folding [108,131]. SHTN1 is important for axon growth [146] and LAMB1 for brain development [147]. HOOK1 is involved in vesicle trafficking [148] and MRT3 was proposed to be involved in centrosome organization. NFKBIB is a negative regulator of the crucial cellular signaling pathway NF-κB [149]. IRTKS participates in the organization of the actin cytoskeleton and RIOK2 in the regulation of mitosis [150]. QRICH1 is involved in the control of the longitudinal bone growth [151]. LNP is crucial for the proper development of the nervous system [152] and WDR11 for hedgehog signaling as well as ciliogenesis [137]. WDR 44 was proposed to be involved in the recycling of vesicles and OCRL is important for the formation of primary cilia [153].

Collection of missense mutations in IFT122 from patients with Sensenbrenner

From previous publications we gathered a total of eight missense mutations in IFT122 found in patients affect by ciliopathies (table 14). Three of these mutations (S373R, V442L and G623) occur homozygous in patients, while the other five occur as compound heterozygotes. Even though IFT122 is part of the IFT-A core complex all eight mutations are associated with Sensenbrenner, same as with IFT121 from the peripheral complex. The clinical features of Sensenbrenner include skeletal abnormalities as well as retinal degeneration [17,95] .For analysis

of the PPIs of all eight mutations HEK293 stable lines expressing IFT122 WT or ciliopathy-related mutant constructs with a N-terminal Strep/FLAG-tag were generated.

Table 14: Missense mutations in IFT121 and corresponding clinical phenotype. *From previous publications a list of eight missense mutations (first column) reported from patients suffering from ciliopathies and harbouring mutations in both alleles of IFT122 was created, mostly compound heterozygotes and in three out of eight cases homozygotes. For each patient the allelic combination and the reported clinical phenotype is shown.*

Mutation	Second allele	Phenotype	Publication
p. W7C	c.502+5G>A	Sensenbrenner	[17]
p. S373F	p. S373F	Sensenbrenner	[17]
p. V442L	p. Y339Wfs*73	Sensenbrenner	[154]
p. G546R	p. E370Sfs*51	Sensenbrenner	[155]
P. V553G	P. V553G	Sensenbrenner	[17]
P. F621C	p. Y1077Vfs*11	Sensenbrenner	[154]
p. G623V	p. G623V	Sensenbrenner	[19]
p. L763P	c.2005-13T>A	Sensenbrenner	[154]

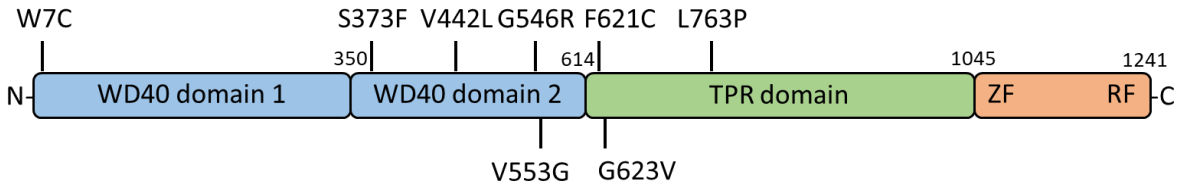

Figure 16: Domain diagram of IFT21 with mutations. *A domain diagram for IFT121 is shown. The different domains are indicated (WD40 in blue; TPR-repeats in green; RING finger (RF) and ZINC finger (ZF) domain in orange). The position of the ciliopathy-associated missense mutations in the domain diagram is indicated with an arrow.*

Ciliopathy-associated IFT122 missense mutations disrupt the interaction with the IFT-A peripheral subcomplex

To analyse the IFT122 protein interactome and the changes induced by ciliopathy-associated mutations HEK293 stable lines were lysed followed by affinity purification and a quantitative LC-MS/MS analysis. In a first step stable interactors of WT IFT122 were identified. In a second step the ratio of these interactors was evaluated for quantitative changes in the analysed mutants compared to the WT. Statistical analysis of six replicates for each condition was performed (student's t-test p-value <0.05 and Significance A p-value <0.05). A heat map summarizing the results is shown in figure 17 [78].

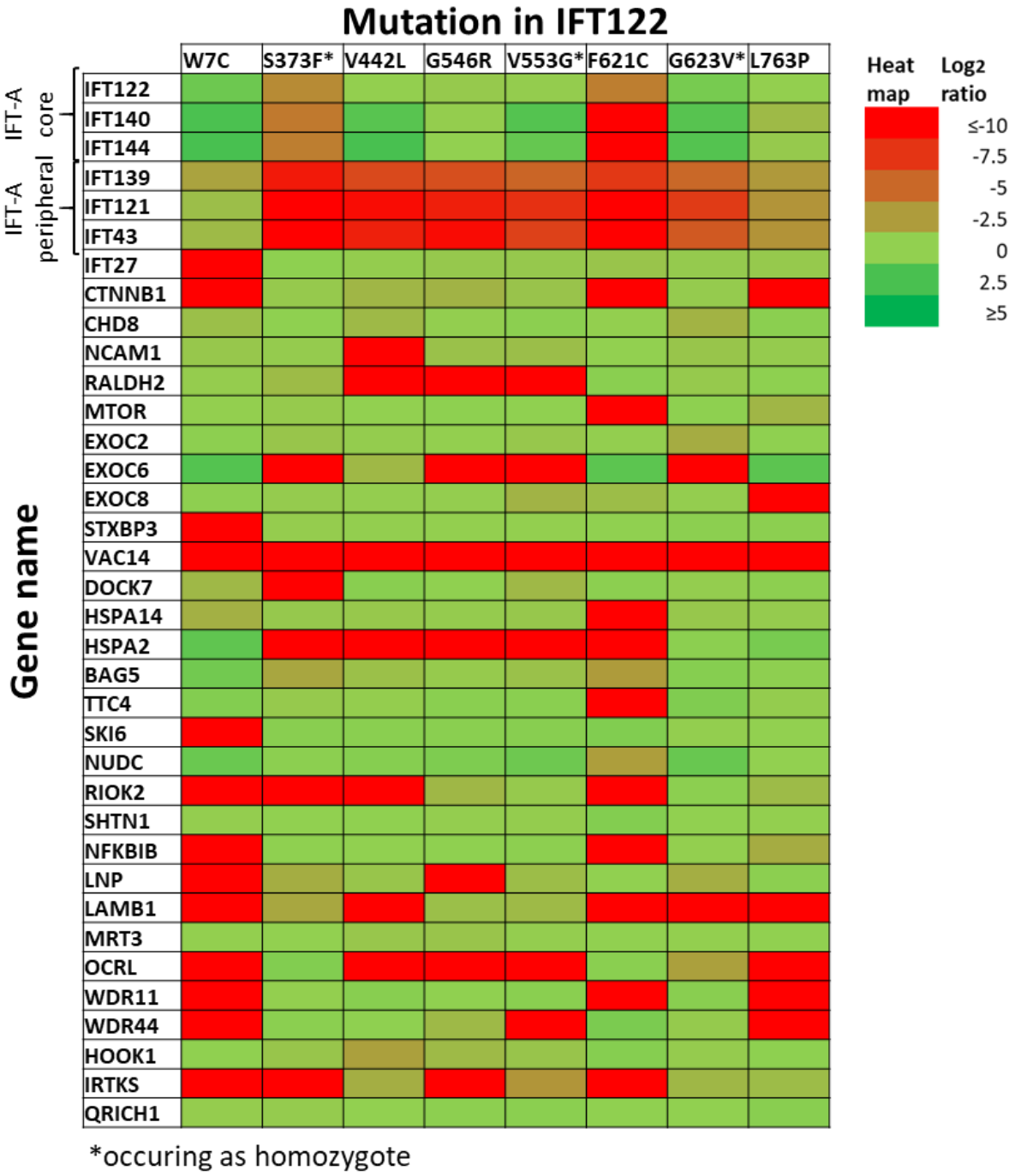

***Figure 17: IFT122 missense mutations impact protein interaction networks**. For eight ciliopathy-associated missense mutations in IFT122 the changes affecting interaction partners of wildtype IFT122 were assessed. Strep affinity purification was performed with lysates from HEK293 cells stably overexpressing IFT122 wildtype or mutant construct fused to an N-terminal Strep/FLAG-tag. Mass spectrometric identification and label free quantification of the detected peptides was achieved using MaxQuant. Statistical analysis was performed using a R script and the log_2 ratios of mutant vs. wildtype were calculated and are shown in a heat map for eight missense mutations. Log_2 ratios of 0 indicate similar abundance of the protein in wildtype and mutant conditions, while log_2 ratios <0 indicate reduced protein binding in mutant samples as compared to wildtype. Mutations are sorted from left to right according to their position in the protein from N- to C-terminal direction.*

The components of the IFT-A core complex (IFT122, IFT140 and IFT144) are unaltered in six out of eight mutations (W7C, V442L, G546R, V553G, G623V and L763P) and strongly reduced in the two mutations S373F and F621C. IFT139 is strongly reduced in six out of eight mutations

(S373F, V442L, G546R, V553G, F621C and G623V) and slightly reduced in two mutations (W7C and L763P). IFT121 and IFT43 are strongly reduced in six out of eight mutations (S373F, V442L, G546R, V553G, F621C and G623V), slightly reduced in L763P and unaltered in W7C. IFT27 is strongly reduced in W7C and unaffected in the other seven mutations (S373F, V442L, G546R, V553G, F621C, G623V and L763P). CTNNB1 is strongly reduced in three out of eight mutations (W7C, F621C and L763P) and unaltered in the other five mutants. CHD8, SHTN1, MRT3 and QRICH1 are unaltered in all mutations. NCAM1 is strongly reduced in one out of eight mutations (V442L) and unaltered in the other seven mutations. RALDH2 is strongly reduced in three out of eight mutations (V442L, G546R and V553G) and unaltered in the other five mutations. MTOR is strongly reduced in the F621C mutations and unaltered in the other seven mutations. EXOC2 is unaltered in all eight mutations, while EXOC6 is strongly reduced in four out of eight mutations (S373F, G546R, V553G and G623V) and unaltered in the other four mutations. EXOC8 is strongly reduced in the L763P mutation and STXBP3 in the W7C mutation, while both are unaltered in the other seven mutations. VAC14 is strongly reduced in all eight mutations. DOCK seven is strongly reduced in the S373F mutation and unaltered in the other seven mutations. HSPA14 is strongly reduced in the F621C mutation and unaltered in the other seven, while HSPA2 is strongly reduced in five out of eight mutations (S373F, V442L, G546R, V553G and F621C) and unaltered in the other three mutations (W7C, G623V and L763P). BAG5 is unaltered in all eight mutations and TTC4 strongly reduced in the F621C mutation while being unaltered in the other seven mutations. SKI6 is strongly reduced in the W7C mutation and unaltered in the other seven, while NUDC is slightly reduced in the F621C mutation and unaltered in the other seven mutations. RIOK2 is strongly reduced in four out of eight mutations (W7C, S373F, V442L and F621C) and unaltered in the other four mutations (G546R, V553G, G623R, L763P). NFKBIB is strongly reduced in two out of eight mutations (W7C and F621C) and unaltered in the other six mutations. LNP is strongly reduced in two out of eight mutations (W7C and G546R) and unaltered in the six remaining mutations. LAMB1 is strongly reduced in five out of eight mutations (W7C, V442L, F621C, G623R and L763P) and unaltered in the other three mutations. OCRL is strongly reduced in five out of eight mutations (W7C, V442L, G564R, V553G and L763P), slightly reduced in G623R and unaltered in the remaining two mutations (S373F and F621C). WDR11 is strongly reduced in three out of eight mutations (W7C, F621C and L763P) and unaltered in the other five mutations, while HOOK1 is slightly disrupted in the V442L mutation and unaffected in the remaining seven mutations. IRTS is strongly reduced in four out of eight mutations (W7C, S373F, G546R and F621C), slightly reduced in the V553G mutation and unaltered in the remaining three mutations (V442L, G623R and L763P). To further understand the IFT-A core and peripheral complex stability and its influence on the disease outcome, another IFT-A core protein was analysed.

Identification of the IFT140 wildtype interactome

After analysing two components of the IFT-A peripheral complex (IFT43 and IFT121) and one component of the IFT-A core complex (IFT122) another component of the IFT-A core complex was analysed. IFT140 is an essential part of the IFT-A core complex. Similar to IFT121 and IFT122 it contains two N-terminal WD40 domains as well as a C-terminal TPR domain, but no Zinc or RING finger domain. For IFT140 a large number of disease-associated missense mutations is reported, which lead to an extremely heterogeneous disease spectrum. Affected patients show clinical phenotypes ranging from isolated retinal dystrophy to systemic diseases such as Jeune syndrome or Mainzer Saldino (table 16). The protein interaction network of wildtype IFT140 and the impact of disease-associated missense mutations was analysed as described. Using a total of 36 biological replicates from 12 separate experiments an extremely robust dataset for statistical analysis of the IFT140 wildtype interactome was obtained. Figure 18 shows a scatter plot representing the proteins retrieved in the experiments.

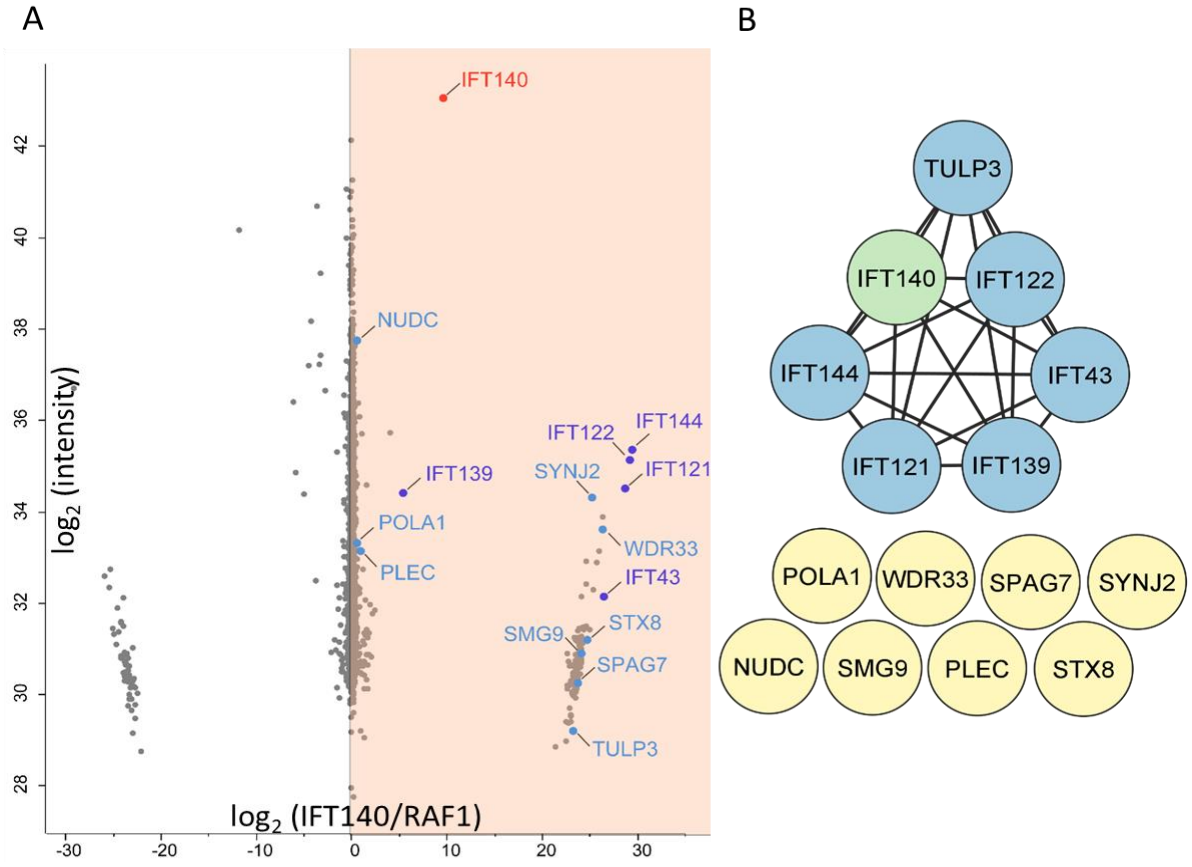

Figure 18: ***Identification of the IFT140 wildtype interactome.*** *(A) Using Strep affinity purification with lysates from HEK293 cells stably overexpressing IFT140 WT or RAF1 as negative control fused to a N-terminal Strep/FLAG-tag, the protein interactome of IFT140 was determined. Mass spectrometric identification and label free quantification of the detected peptides was performed using MaxQuant. Statistical analysis (n=36) was done with R (student's t-test: p<0.05; Significance A: p<0.05) and the log_2 ratios of IFT140 vs. RAF1 were calculated and plotted. (B) A protein interaction analysis for the identified interactors was performed using the STRING database. In addition to all components of the IFT-A complex also known interactors like TULP3 were identified. In total nine proteins which are not part of the IFT-A complex were identified as potential interactors. Proteins are coloured according to protein interaction clusters.*

Table 15: Enriched proteins in the IFT140 wildtype affinity purification. *For the analysis of the IFT140 protein-protein interaction a Strep affinity purification was performed (n=36). RAF1 was used as a negative control. Mass spectrometric identification and label free quantification of the detected peptides was performed using MaxQuant. Statistical analysis was done using R and the log_2 ratios calculated (IFT140/RAF1). Ratios as well as p-values from the statistical analysis and known functions of potential interactors are shown. Genes are sorted according to interaction clusters and their log_2 ratios.*

Gene name	log_2 ratio (IFT140/RAF1)	student's t-test	Signifi-cance A	Protein function
IFT140 (bait)	9.6	***	***	IFT-A core complex [30]
IFT144	29.45	***	***	IFT-A core complex [30]
IFT121	28.73	***	***	IFT-A peripheral complex [30]
IFT43	26.44	***	***	IFT-A peripheral complex [30]
IFT122	23.71	***	***	IFT-A core complex [30]
TULP3	23.18	***	***	negative regulation of Shh-signaling [34–36]
IFT139	5.39	**	***	IFT-A peripheral complex [30]
WDR33	26.31	*	***	mRNA modification
SYNJ2	25.18	*	***	membrane trafficking and signal transduction [156]
STX8	24.71	*	***	vesicle trafficking [157]
SMG9	24.14	*	***	Wnt/ß-catenin signaling [158]
SPAG7	23.71	**	***	unknown
PLEC	0.88	*	***	cytoskeleton, interlinks intermediate filaments with microtubules [159]
POLA1	0.59	**	**	initiation of DNA synthesis [160]
NUDC	0.53	***	**	Spindle formation and microtubule organization; protein folding [131,132,161]

15 proteins were found to be enriched in the data (figure 18 and table 15), including all components of the IFT complex A. Besides the IFT-A complex itself, known interactors of IFT-A were enriched, such as the ciliary protein TULP3, a negative regulator of hedghehog signaling [34–36]. SYNJ2 was also found to be enriched, a protein involved in membrane trafficking and signal transduction [156]. Another previously reported interactor is NUDC, which is involved in spindle formation during mitosis and microtubule organization during cytokinesis [15,16]. Gene enrichment analysis of the generated protein-protein interaction data using STRING (https://string-db.org/) revealed eight so far unknown potential interactors as enriched in the dataset (figure 18) [78]. To illuminate potential new roles of IFT140 the function of each so far unknown potential interactor has been searched (table 15). PLEC has been proposed to be involved in the organization of the cytoskeleton, where it interlinks intermediate filaments with microtubules [159]. Apart from its role in the nonsense-mediated decay of mRNA the protein SMG9 has been proposed to play a role in brain, heart and eye development[158]. STX8 is thought to be involved in vesicle trafficking[157] and POLA1 in the initiation of DNA synthesis [160]. The role of SPAG7 is so far unknown [78].

Missense mutations in IFT140 lead to a heterogeneous disease spectrum

From previous publications 24 missense mutations in IFT140 from patients affect by disease were selected. Most of these mutations occur as compound heterozygotes, while four mutations (I233M, C333Y, T484M and E664K) occur as homozygotes [23,26,94,162]. In contrast to the other analysed components of IFT-A, missense mutations in IFT140 vary largely in their clinical outcome, ranging from retinal diseases to skeletal abnormalities, atrioventricular septal defects and organ deficiencies such as Mainzer-Saldino and Jeune syndrome (table 16).

Table 16: Missense mutations in IFT140 and corresponding clinical phenotype. *From previous publications a list of 24 missense mutations reported from patients suffering from ciliopathies and harbouring mutations in both alleles of IFT140 was gathered, mostly compound heterozygotes. For each patient the allelic combination and the reported clinical phenotype is shown. Mutations are sorted according to severity of the clinical phenotype*

Mutation	Second allele	Phenotype	Publication
p. C333Y	p. C333Y	Isolated retinal dystrophy	23
p. A341T	p. Arg475Asnfs*14	Isolated retinal dystrophy	23
p. T484M	p. T484M	Isolated retinal dystrophy	23
p. S939P	c.2399+1G>T	Isolated retinal dystrophy	23
p. P71L	p. V217Gfs*2	retinitis pigmentosa	163
p. C663W	p. G1276R	retinitis pigmentosa	163
p. R871C	p. W459*	retinitis pigmentosa	163
p. A974V	p. A418P	retinitis pigmentosa	163
p. L1399P	p. N633Sfs*10	retinitis pigmentosa	163
p. C329R	p. T484M	LCA	163
p. E790K	p. E522Gfs*6	LCA	163
p. V108M	p. E1065K	Atrioventricular septal defect	62
p. L440P	unknown	LCA, renal failure	23
p. E664K	p. E664K	Retinal dystrophy with skeletal defects	94,162
p. G212R	c.2399+1G>T	JATD	26
p. V292M	p. G522E	JATD	93
p. V292M	p. N460Kfs28	JATD	93
p. G140R	p. E164*	Mainzer-Saldino	93
p. G212R	p. Ala1306Glyfs*56	Mainzer-Saldino	26
p. I233M	c.2399+1G>T	Mainzer-Saldino	26
p. I233M	p. I233M	Mainzer-Saldino	26
p. Y311C	p. Ile286Lysfs*6	Mainzer-Saldino	26
p. E664K	c.2399+1G>T	Mainzer-Saldino	26
p. C1360R	c.2399+1G>T	Mainzer-Saldino	93

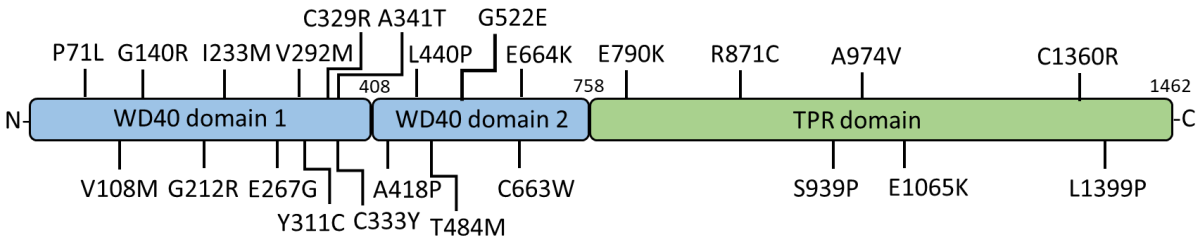

Figure 19: Domain diagram of IFT21 with mutations. *A domain diagram for IFT121 is shown. The different domains are indicated (WD40 in blue; TPR-repeats in green). The position of the ciliopathy-associated missense mutations in the domain diagram are indicated.*

Ciliopathy-associated IFT140 missense mutations have edgetic effects and disrupt IFT-A complex stability as well as TULP3 interaction

To analyse the IFT140 protein interactome and the changes induced by ciliopathy-associated mutations affinity purification followed by LC-MS/MS was performed with the generated HEK293 stable lines [78]. The potential interaction partners were first filtered for stable interactors of WT IFT140. In a second step, the ratio of these interactors was evaluated for quantitative changes in the mutants compared to the WT [78]. Through the statistical analysis of six replicates each using stringent statistical filters (student's t-test p-value <0.05 and Significance A p-value <0.05) a robust dataset was obtained. The different effects of IFT140 missense mutations on complex stability and TULP3 interaction are exemplarily shown for the mutations G212R, E267G and C663W in figure 20. In figure 21 all results regarding IFT-A complex composition and TULP3 interaction are summarized [78].

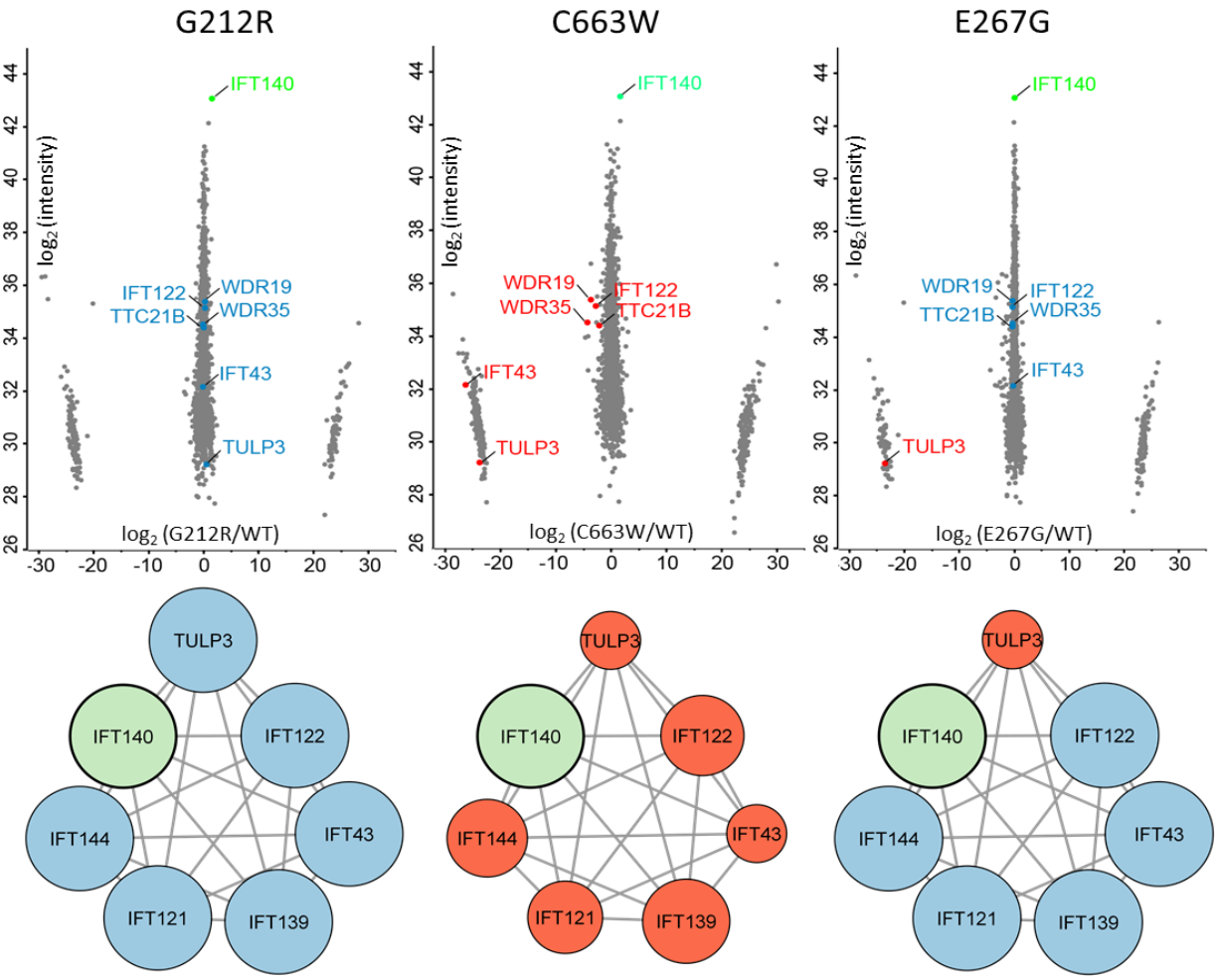

Figure 20: Missense mutations in IFT140 have varying effects on IFT-A complex stability and TULP3 interaction. *The effect of missense mutations in IFT140 was assessed via Strep affinity purification with lysates from HEK293 cells stably overexpressing IFT140 WT or mutant construct fused to a N-terminal Strep/FLAG-tag. Mass spectrometric identification and label free quantification of the detected peptides was performed using MaxQuant* [78]*. Statistical analysis was performed using R and the log₂ ratios of mutant vs. WT were calculated. Scatter plots are shown for the mutations G212R, E267G and C663W. The effect of each mutation on the interaction of IFT140 with other IFT-A proteins as well as TULP3 is shown below each scatter plot. IFT140 (green) was used as bait. Protein interactions that have not been affected are shown in blue. Disrupted interactions are indicated in red with the size reduction of the corresponding circle reflecting the severity of the reduction of binding in the mutant as compared to IFT140 WT* [78]*.*

The IFT-A complex could be reliably detected and quantified in our experiments (figure 21 and 23). For seven out of 24 mutations (V108M, G140R, A341P, G522E, E664K, C663W, S939P) an impairment of the IFT-A complex integrity was observed [78]. This is indicated by the reduced abundance of IFT-A components in these mutants, while the levels of IFT140 are comparable in both conditions. For other mutations the complex composition was not affected (figure 21 and 23). This indicates that at least a subset of missense mutations might disrupt the stability of the IFT-A complex, changing its composition and potentially hampering its molecular function [78]. Several patients harbour two mutations, which do not lead to the disruption of the IFT-A complex in our experiments, e.g. A974V/A418P and C329R/T484M. This makes

complex disruption as the single cause of disease unlikely [78]. In the mutants A418, L440P and T484M (three out of 24) all components of the IFT-A complex are slightly enriched, even though protein levels of IFT140 are similar as compared to the IFT140 WT. In the case of the T484M mutant IFT43 is strongly enriched [78].

For the mutant L1399P the abundance of the bait protein IFT140 as well as all IFT-A components were significantly reduced in comparison to the WT, indicating problems with expression or protein stability [78]. V108M, G140R, A341P, G522E, E664K, C663W, R871C and L1399P (eight out of 24) led to significantly reduced binding of IFT-A components. In the case of G522E, E664K, C663W and L1399P (four out of 24), IFT43 was not detected in the mutant condition [78].

In the mutants G212R, Y311C, C329R and C333Y (four out of 24), the protein TULP3 was detected at similar levels as in the corresponding WT control (figure 21) [78]. A group of seven out of 24 mutations (V108M, G140R, E267G, V292M, A341P, C663W and S939P) showed a strong reduction in the binding of TULP3. In no case a stronger binding of TULP3 in the mutant in comparison to the WT condition could be observed [78].

For all four mutants (G212R, Y311C, C329R and C333Y), which showed no reduced binding of TULP3 as compared to IFT140 WT, also no strong disruption of IFT-A complex stability was observed (shown for G212R in figure 20 and in figure 21) [78]. In the case of four mutants (V108M, G140R, A341P and C663W) a severe disruption of IFT-A complex integrity accompanied by reduced binding of TULP3 could be detected (shown for C663W in figure 20 and figure 21). Three mutants (E267G, V292M and E267G) resulted in reduced TULP3 binding in the mutant, but had only a weak (V292M and S939P) or no effect at all (E267G) on IFT-A composition (shown for E267G in figure 20 and figure 21) [78].

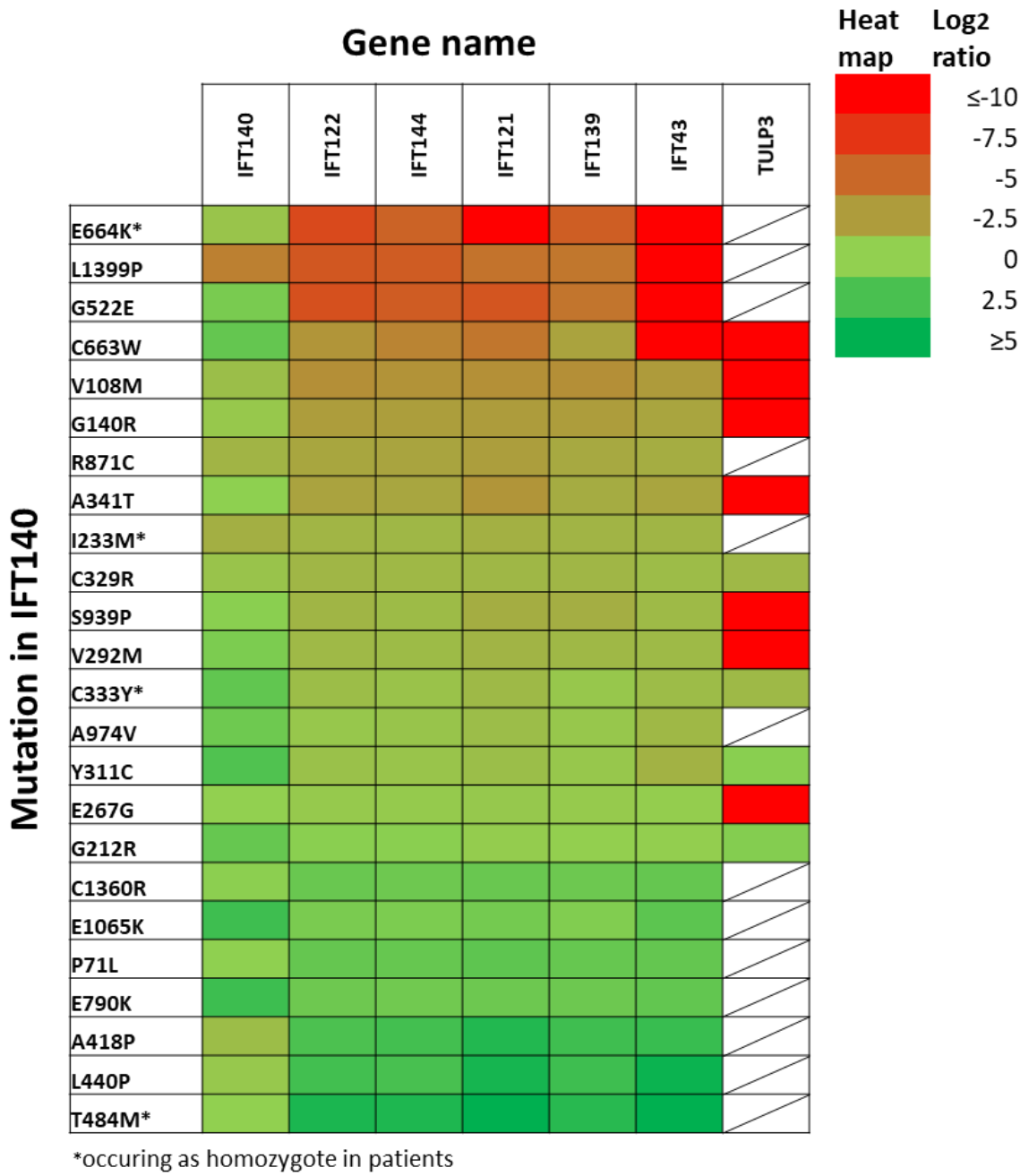

Figure 21: A subset IFT140 missense mutations is hypomorph and has a quantitative effect on IFT-A complex composition. *For 24 ciliopathy-associated missense mutations in IFT140 the changes affecting interaction partners of IFT140 WT were assessed by Strep affinity purification. Mass spectrometric identification and label free quantification of the detected peptides was performed using MaxQuant. Statistical analysis was performed using R and the log_2 ratios of mutant vs. WT were calculated and are shown in a heat map for 24 missense mutations. Log_2 ratios of 0 indicate similar abundance of the protein in WT and mutant conditions, while log_2 ratios <0 indicate reduced protein levels in mutant samples as compared to WT. Crossed fields are shown for cases in which the protein could not be detected. Mutations are sorted from top to bottom according to the severity of the IFT-A complex disruption* [78].

Single nucleotide polymorphisms (SNPs) in IFT140 do not affect IFT-A complex composition

The data revealed that IFT-A complex integrity is impaired in a quantitative manner by a subset of IFT140 missense mutations. To further strengthen the hypothesis that this effect is related to the clinical phenotype observed in the affected patients, the effect of single nucleotide polymorphism in IFT140 on the IFT-A complex integrity was assessed. Using the gnomAD database six mutations in IFT140 were selected, which lead to exchanges of single amino acids similar in severity to the disease-associated IFT140 missense mutations. Selected SNPs needed to show high allele frequencies in healthy individuals and occur as homozygotes in at least one individual. Analog to the analysis of the IFT140 missense mutations HEK293 cells stably expressing IFT140 WT and SNP constructs were used, both N-terminal fused to a Strep/FLAG-tag. A Strep affinity purification followed by LC-MS/MS analysis and label free quantification was performed with three biological replicates for each condition. The mutant/WT ratios of all six IFT-A components were calculated for a total of six SNPs and are shown in figure 22.

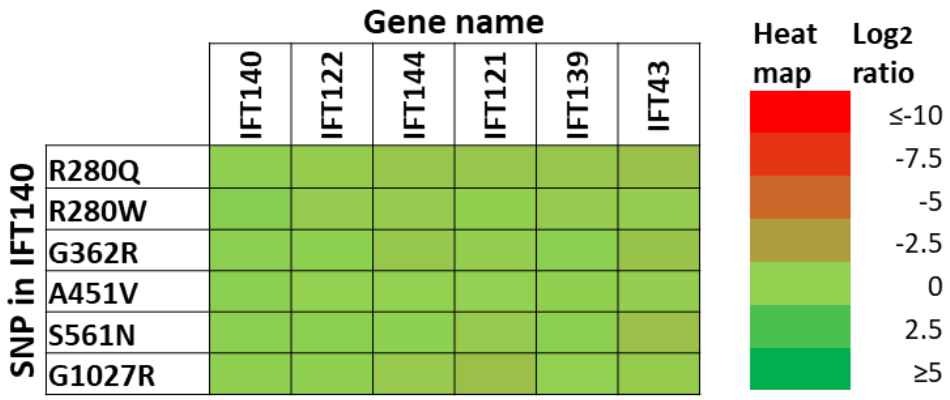

Figure 22: IFT140 SNPs have no effect on IFT-A complex composition. *For six single nucleotide polymorphisms (SNPs) that lead to the exchange of a single amino acid in IFT140 the effect on IFT-A complex composition was assessed. Strep affinity purification followed by mass spectrometric identification and label free quantification of the detected peptides using MaxQuant was applied and IFT140 WT and SNPs were compared. Statistical analysis was performed using R and the log_2 ratios of SNP vs. WT were calculated and are shown in a heat map for six SNPs. Log_2 ratios of 0 indicate similar abundance of the protein in WT and mutant conditions, while log_2 ratios <0 indicate reduced protein levels in SNP samples as compared to WT. SNPs are sorted according to their position.*

The data revealed that the composition of the IFT-A protein complex is not affected by SNPs in IFT140, even though the amino acid exchanged are comparable in severity to the disease-associated missense mutations in IFT140. This indicates that the disruptive effects on IFT-A complex composition are exclusive to disease-associated mutations and relevant for the clinical phenotype observed in patients harbouring these mutations.

Missense mutations in IFT140 have edgetic effects on specific PPIs

In the mutant conditions G212R, Y311C, C329R and C333Y (four out of 24) the protein TULP3 was detected at similar levels as in the corresponding wildtype control. A group of seven out of 24 mutations (V108M, G140R, E267G, V292M, A341P, C663W and S939P) showed a strong reduction of TULP3 binding. In no case a higher binding of TULP3 in the mutant in comparison to the wildtype condition could be observed. The protein SYNJ2 is reduced in P71L (one out of 24), while it is enriched in C333Y, G522E, C663W and A974V (four out of 24). PLEC is enriched in the case of P71L, L440P, T484M and C1360R (four out of 24) while being mildly reduced in the case of G522E (one out of 24). In five out of 24 mutations (Y311C, C333Y, E790K, A974V, E1065K) the protein STX8 was reduced and SMG9 in four out of 24 (I233M, Y311C, C663W, A974V). SPAG7 was reduced in the case of the E790K mutation (one out of 24). POLA1 and NUDC were detected in all samples and were unaffected by all mutations. WDR33 was detected in 13 out of 24 mutations and unaltered in all of them.

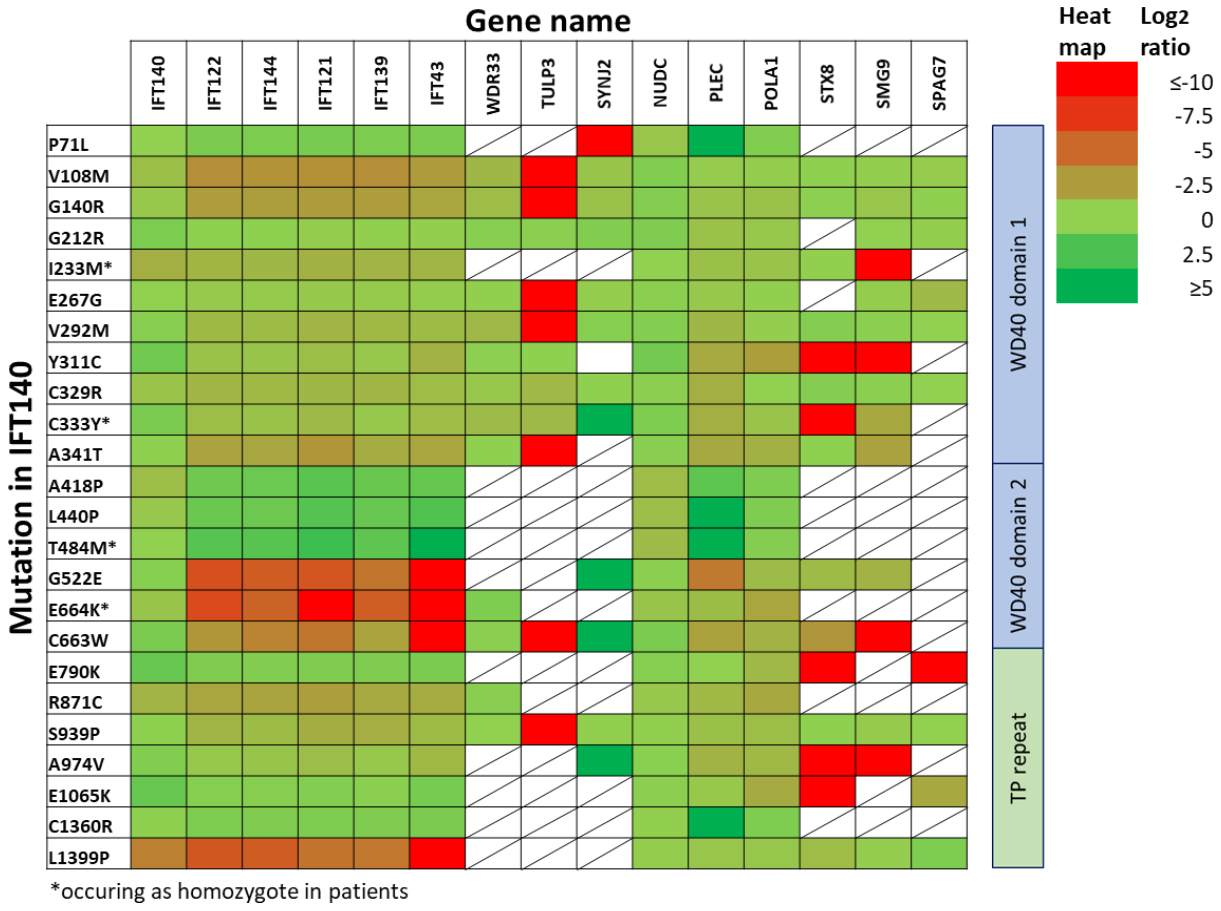

Figure 23: IFT140 missense mutations have edgetic effects on protein interaction networks. *For 24 ciliopathy-associated missense mutations in IFT140 the changes affecting interaction partners of wildtype IFT140 were assessed. Step affinity purification was applied with lysates from HEK293 cells stably overexpressing IFT140 wildtype or mutant construct fused to a N-terminal Strep/FLAG-tag. Mass spectrometric identification and label free quantification of the detected peptides was performed using MaxQuant. Statistical analysis was performed using R and the log_2 ratios of mutant vs. wildtype calculated and are shown in a heat map for 24 missense mutations. Log_2 ratios of 0 indicate similar abundance of the protein in wildtype and mutant conditions, while log_2 ratios <0 indicate reduced protein levels in mutant samples as compared to wildtype. Crossed fields are shown for cases in which no data could be obtained. Mutations are sorted from top to bottom according to position* [78].

Allelic combination of disruptive missense mutation correlates with severity of the clinical phenotype

To assess whether the disruption of IFT-A complex stability observed in the experiments may contribute to the clinical outcome the allelic combination of missense mutations was assessed. For eight patients harbouring missense mutations in IFT140 on both alleles [23,26,94,162] the allelic combination and severity of each allele on the IFT-A complex integrity was assessed. A clear correlation of the severity of the clinical phenotype and the disruptive effect of the harboured mutations on the IFT-A complex integrity was observed (table 17). Patients with missense mutations, that show mild or no disruption of IFT-A in the LC-MS/MS experiments on both alleles, also show milder clinical features, such as isolated retinal dystrophy. In two patients where a mild allele is combined with a disruptive allele also the severity of the clinical phenotype is increased. Most strikingly, while a patient homozygous for the mildly disruptive T484M mutation suffers an isolated retinal dystrophy, another patient carrying the same T484M mutation in combination with the disruptive C329R mutation suffers from LCA [23,163]. In contrast to isolated retinal dystrophy LCA is characterized by early onset of blindness among other features. In three patients carrying two disruptive alleles also the strongest clinical phenotypes were observed, including systemic diseases such as Mainzer Saldino and Jeune syndrome as well as retinal dystrophy accompanied by skeletal defects.

Table 17: Allelic combination in patients reveals correlation between genotype severity and clinical phenotype. *For eight patients, who harbour missense mutations on both alleles, the severity of the disruption of IFT-A complex stability for each allele was assessed. A strong disruption was defined as an accumulated log_2 change of at least -5 for all five IFT-A components, meaning that on average the binding of each component was reduced by 50%. Strong disruption is indicated in red, while weak or no disruption is indicated by a green field. Patients are sorted from top to bottom with increasing severity of the clinical phenotype. While patients with two undisruptive or mild disruptive alleles show milder clinical phenotypes, disease severity increases in cases where one strongly disruptive allele is included. The strongest clinical phenotypes are observed in patients who harbour disruptive missense mutations in IFT140 on both alleles, showing a clear correlation between genotype and phenotype.*

Patient	First allele	Severity	Second allele	Severity	Clinical phenotype
1	p. C333Y		p. C333Y		Isolated retinal dystrophy
2	p. T484M		p. T484M		Isolated retinal dystrophy
3	p. A418P		p. A974V		retinitis pigmentosa
4	p. C329R		p. T484M		LCA
5	p. V108M		p. E1065K		Atrioventricular septal defect
6	p. E664K		p. E664K		Retinal dystrophy with skeletal defects
7	p. V292M		p. G522E		JATD
8	p. I233M		p. I233M		Mainzer-Saldino

Shorter IFT140 isoform does not rescue IFT-A complex integrity

In human, beside the full length isoform of IFT140 (1462aa) also a shorter isoform of IFT140 is expressed (656aa). This isoform is characterized by the loss of both WD40 domains and parts of the TPR domain (figure 24). Potential defects with e.g. protein stability or folding caused by mutations in the WD40 domains should not affect the short isoform. Hence the shorter isoform might be capable of partially rescuing the native protein function of IFT140 in patients affected by mutations. To assess the ability of this shorter isoform to rescue the integrity of the IFT-A complex affinity purification was performed to investigate isoform-specific interactions. Using HEK293 cells stably expressing N-terminally Strep/FLAG-tagged IFT140 short isoform or RAF1 a Strep affinity purification was performed. After protein precipitation and tryptic digest LC-MS/MS analysis of the obtained peptides was performed. Label free quantification was done using MaxQuant. A scatter plot as well as the $\log_2$ ratios for all IFT-A components are shown in figure 24.

In addition to the bait protein IFT140 also IFT43 was enriched in the IFT140 isoform and to a low extent IFT139. Both IFT43 and IFT139 are part of the IFT-A peripheral subcomplex. While the abundance of IFT121 was similar in both conditions, IFT144 was mildly reduced in the IFT140 isoform and IFT122 strongly reduced. Taken together this data indicates that the loss of both WD40 domains and part of the TPR domain leads to the loss of the short isoforms ability to bind to the whole IFT-A complex.

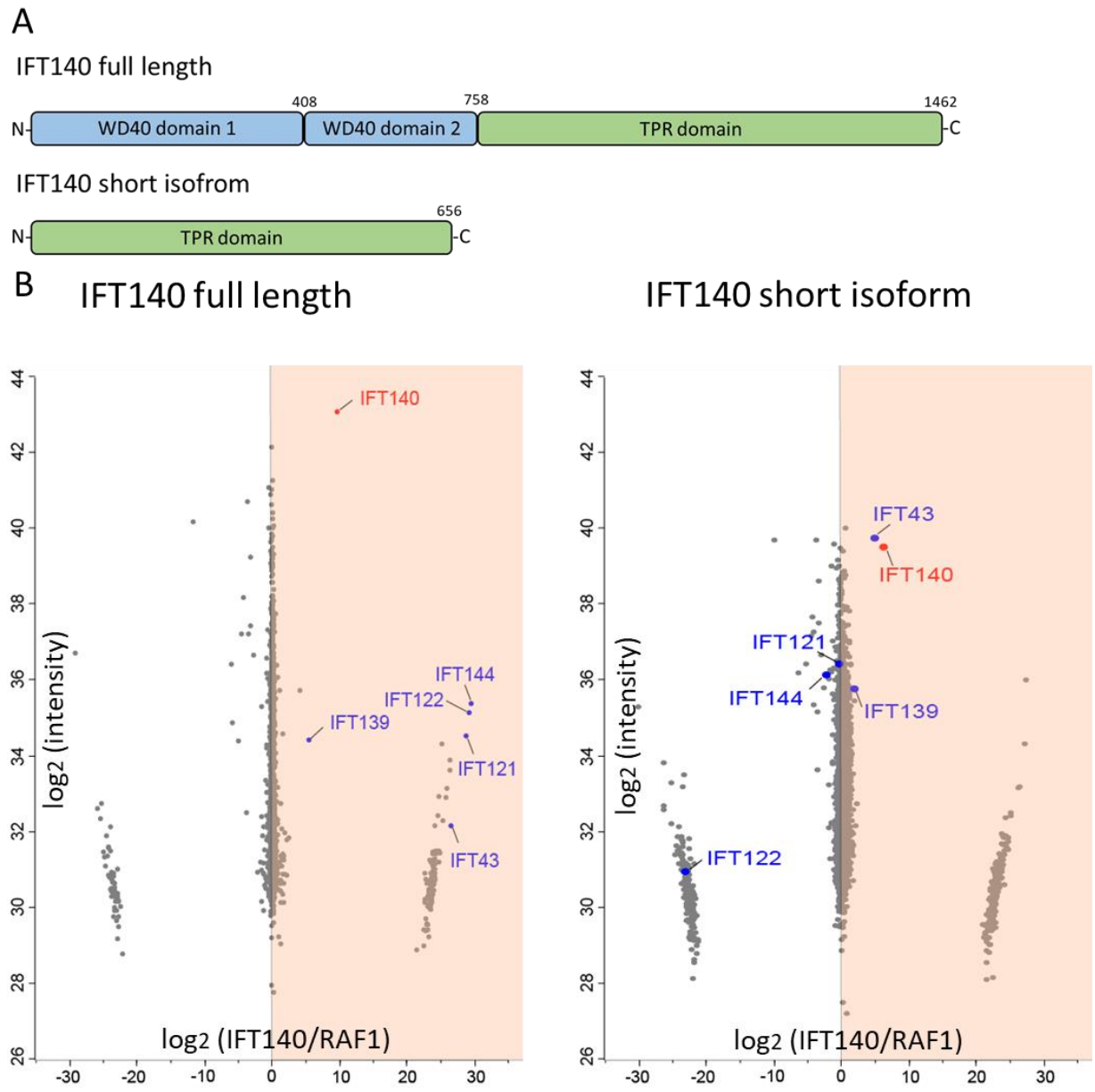

Figure 24: Short isoform of IFT140 does not bind all IFT-A components. *(A) The short isoform of IFT140 is lacking 806 amino acids, leading to the loss of both WD40 domains and parts of the TPR domain. (B) The ability of the short isoform of IFT140 to bind to IFT-A components was assessed via Strep affinity purification with lysates from HEK293 cells stably overexpressing IFT140 short isoform or RAF1 fused to an N-terminal Strep/FLAG-tag. Mass spectrometric identification and label free quantification of the detected peptides was performed using MaxQuant. The log_2 ratios of IFT140 isoform vs. RAF1 were calculated and plotted and IFT-A components labelled.*

TULP3 interaction is impaired to varying degree by IFT140 missense mutations

Our data identified TULP3 as enriched in IFT140 WT, a ciliary protein with a known role in the regulation of hedgehog signaling (figure 18 and table 15) [78]. In the mutants G212R, Y311C, C329R and C333Y (four out of 24) the protein TULP3 was detected at similar levels as in the corresponding WT control (figure 21). A group of seven out of 24 mutations (V108M, G140R, E267G, V292M, A341P, C663W and S939P) showed a strong reduction of TULP3 binding. The observed reduction in TULP3 binding hints towards a potential impairing or even disruptive effect of seven out of 24 of the analysed missense mutations on the interaction between IFT140 and TULP3 [78]. For the other 13 out of 24 mutations the data did not allow reliable quantification of TULP3. This might be due to technical limitations of the applied shotgun proteomics approach regarding the detection of lowly abundant proteins in complex samples, which may be the case with TULP3 [78]. Even though not all mutants were affected, a misregulation of the IFT140-TULP3 interaction to varying degree might be a cause of clinical defects observed in patients, also when considering the compound heterozygosity of most patients, where the combination of different alleles might cause varying degrees of IFT140-TULP3 disruption. Notably, for three of the four mutations (Y311C, C333Y, T484M, E664K), which occur as homozygotes, TULP3 was not stably detected, which led to a targeted investigation of the IFT140-TULP3 interaction [78].

The interaction of IFT140 and TULP3 was further examined using co-immunoprecipitation followed by SDS-PAGE and western blotting using HEK293 cells stably expressing (N)SF-tagged IFT140 constructs as described (Methods ‘Co-immunoprecipitation by FLAG affinity purification’). Cells were co-transfected with a vector expressing TULP3 fused to a N-terminal HA-tag followed by FLAG affinity purification of IFT140 and detection of IFT140 and TULP3 in eluates by using specific antibodies (figure 25 and 26) [78].

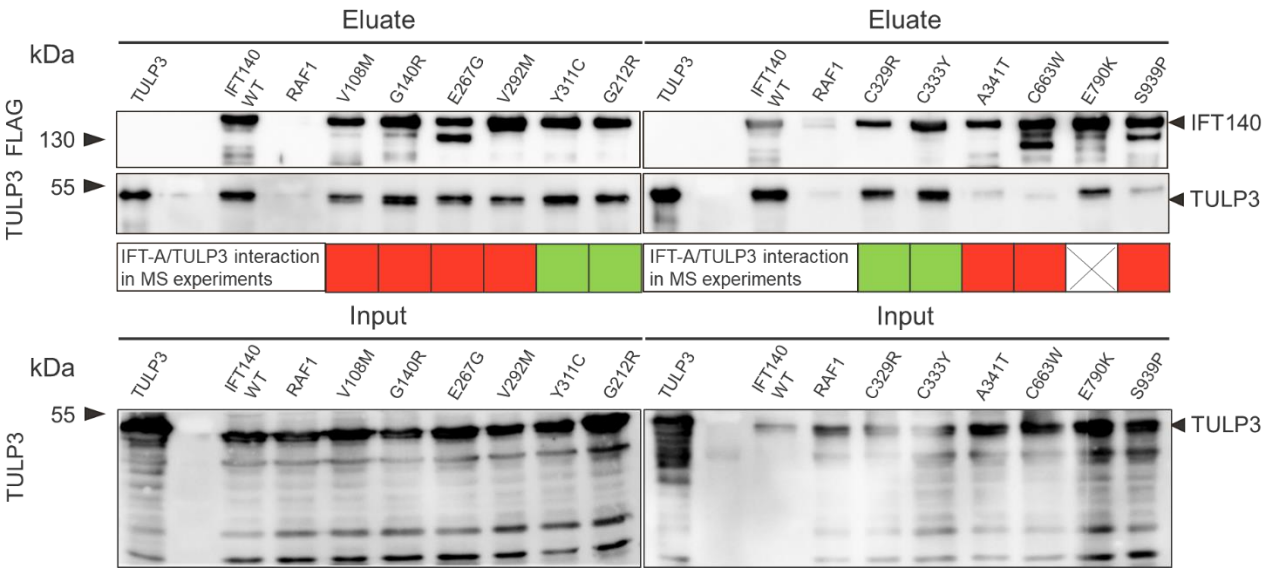

Figure 25: The interaction of IFT140 and TULP3 is disturbed by a subset of missense mutation. *For 12 out of 24 mutations (including all for which a mutant/WT ratio for TULP3 could be determined) a co-immunoprecipitation was performed. A FLAG immunoprecipitation of (N)SF-tagged IFT140 WT and mutant expressing HEK293 cells transiently co-transfected with (N)HA-TULP3. A SDS-PAGE was performed, followed by western blotting with FLAG-specific (for IFT140) and-TULP3-specific antibody. The levels of TULP3 in lysate (50ug) are shown as input and indicate comparable levels of TULP3 in lysates. For each analysed mutant the result for the IFT-A/TULP3 interaction from the MS-experiments is shown at the bottom (red box= disruption of interaction; green box= no disruption of interaction)* [78].

The results of the co-immunoprecipitation further confirmed the findings from the interactome studies. The six out of seven mutations (V108M, E267G, V292M, A341P, C663W, S939P), which showed a loss of TULP3 binding in the previous affinity purification experiments also exhibit reduced binding of TULP3 to IFT140 in co-immunoprecipitation (figure 25) [78]. This effect is not due to different amounts of TULP3, as shown by similar amounts of the protein lysate input. The only exception is the G140R mutation, where the reduced binding of TULP3 in the proteomics experiments is not reflected in the co-immunoprecipitation [78]. While the amounts of IFT140 in eluates seem to vary slightly and degradation products are seen in some conditions, these do not invalidate the findings. The observed alterations in levels of TULP3 are stronger than the differences in the abundance of bait protein in eluates. For the mutation E790K no mass spectrometric data could be obtained [78].

The homozygous mutations represent the best suited model to investigate genotype-phenotype correlations regarding TULP3. Besides validating heterozygote missense mutations, a focused analysis of the four homozygous mutations I233M, C333Y, T484M, and E664K was performed (figure 26) [78]. In the proteomics experiment data for C333Y could be obtained, where the interaction of IFT140 and TULP3 was not changed significantly in comparison to IFT140 WT. In the co-immunoprecipitation a strong signal for TULP3 is visible in case of the C333Y mutation [78]. However, the signal appears weaker in comparison to the WT. In the case of the I233M mutation a degradation product of IFT140 as well as reduced levels of TULP3 can be seen. For T484M and E664K only a weak signal for TULP3 is visible, indicating a strong disruption. Taken together the data strongly suggest that the interaction between IFT140 and TULP3 is disrupted by a subset of missense mutations to varying degree [78].

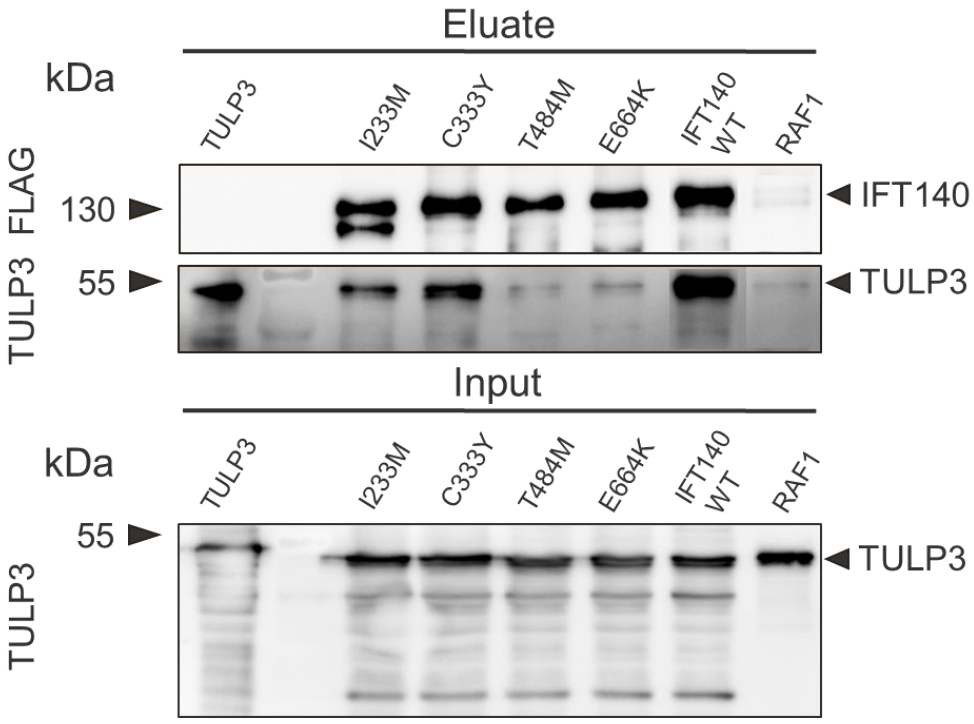

Figure 26: The interaction of IFT140 and TULP3 differs in homozygous missense mutations. *For all four mutations (I233M, C333Y, T484M, E664K), which occur as homozygotes a co-immunoprecipitation was performed. Following a FLAG immunoprecipitation of (N)SF-tagged IFT140 wildtype and mutant expressing HEK293 cells transiently co-transfected with (N)HA-TULP3 a SDS-PAGE was performed followed by western blotting with FLAG-specific (for IFT140) and-TULP3-specific antibody. The levels of TULP3 in equal protein amounts of lysate (50ug) are shown as input and indicate comparable levels of TULP3 in lysates.*

Generation of IFT140 knockout cell lines

For a functional assessment of IFT140 in cellular processes a CRISPR/Cas9-mediated knockout of IFT140 was generated in retinal pigment epithelial cells (hTERT-RPE1). Cells were transfected with sgRNAs targeting a region in IFT140 exon 4 and treated with puromycin. After selection of single clones an isolation of genomic DNA was performed, the region of interest amplified and sent in for Sanger sequencing [164]. A single clone harbouring a 1 bp insertion leading to a frameshift and early stop codon in exon 4 was identified (figure 27). This resulted in a p.H57Tfs33 mutation, which from now on will be referred to as IFT140 knockout.

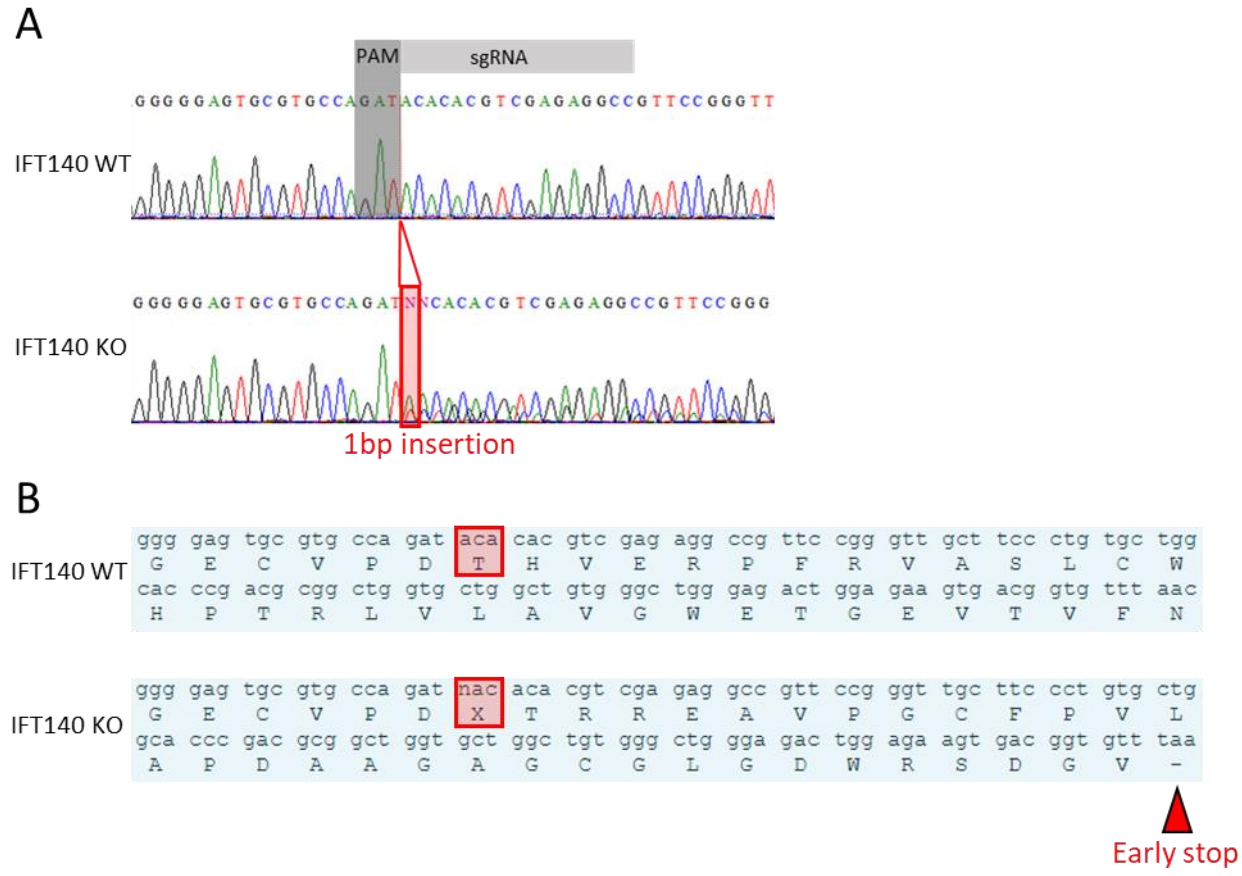

Figure 27: Sequencing of IFT140 wildtype and knockout. *(A) A part of the IFT140 gene sequence is shown with the PAM sequence indicated (dark grey) as well as the sgRNA target region (light grey). The position of the 1 bp insertion in the knockout is marked in red. The sequencing results shows a heterozygous 1bp insertion. (B) Translation of the resulting nucleotide sequence in the IFT140 knockout leads to an early stop codon in exon 4 (red arrow).*

IFT140 knockout in hTERT-RPE1 leads to the loss of full length IFT140

To assess differences in the total protein amount IFT140 KO as well as wildtype cells were lysed and a SDS-PAGE followed by western blotting performed. Using the protein levels of GAPDH as a loading control a clear reduction of the IFT140 signal in IFT140 knockout cells as compared to the wildtype was observed(figure 28).

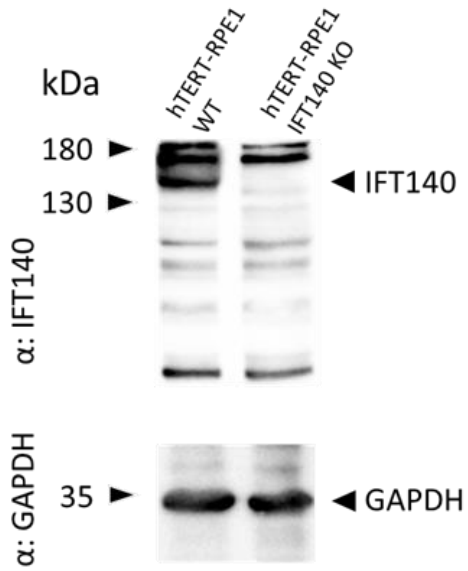

Figure 28: Ful length IFT140 is reduced in IFT140 knockout cells. *Using an antibody specific for IFT140 the protein levels of IFT140 in hTERT-RPE1 wildtype and IFT140 knockout cells were determined. A clear reduction of the IFT140 specific signal can be observed in the knockout as compared to the wildtype. GAPDH levels were used as a loading control.*

To further validate the CRISPR/Cas9-mediated knockout of IFT140 as well as the suitability of the IFT140 specific antibody for localization studies an analysis using immunofluorescence microscopy was performed. The cilium was visualized using an ARL13B specific antibody. ARL13B is a small GTPase, which localizes to the ciliary membrane [31]. For immune-fluorescence microscopy hTERT-RPE1 wildtype as well as IFT140 knockout cells were fixed and subsequently an immunostaining with specific IFT140 and ARL13B antibodies performed. Secondary antibodies linked to a fluorophore and DAPI to visualize the nucleus were used.

Immunofluorescence microscopy revealed a clear signal for ARL13B along the primary cilium in the wildtype control cells. IFT140 co-localized with ARL13B at the primary cilium and was unevenly distributed, with a concentration of IFT140 being visible at the basal body and the ciliary tip region (figure 29). The observed localization of IFT140 at the primary cilium is consistent with previous observations [16,42,53] and confirms the suitability of the used antibody for localization studies of IFT140 in immunofluorescence microscopy.

In the IFT140 knockout cell line no specific signal for IFT140 was detected. This further confirms the successful knockout generation, leading to the loss of functional IFT140. Also in the ARL13B channel no specific signal was visible, which indicate loss of ARL13B at primary cilia in IFT140 knockout cells.

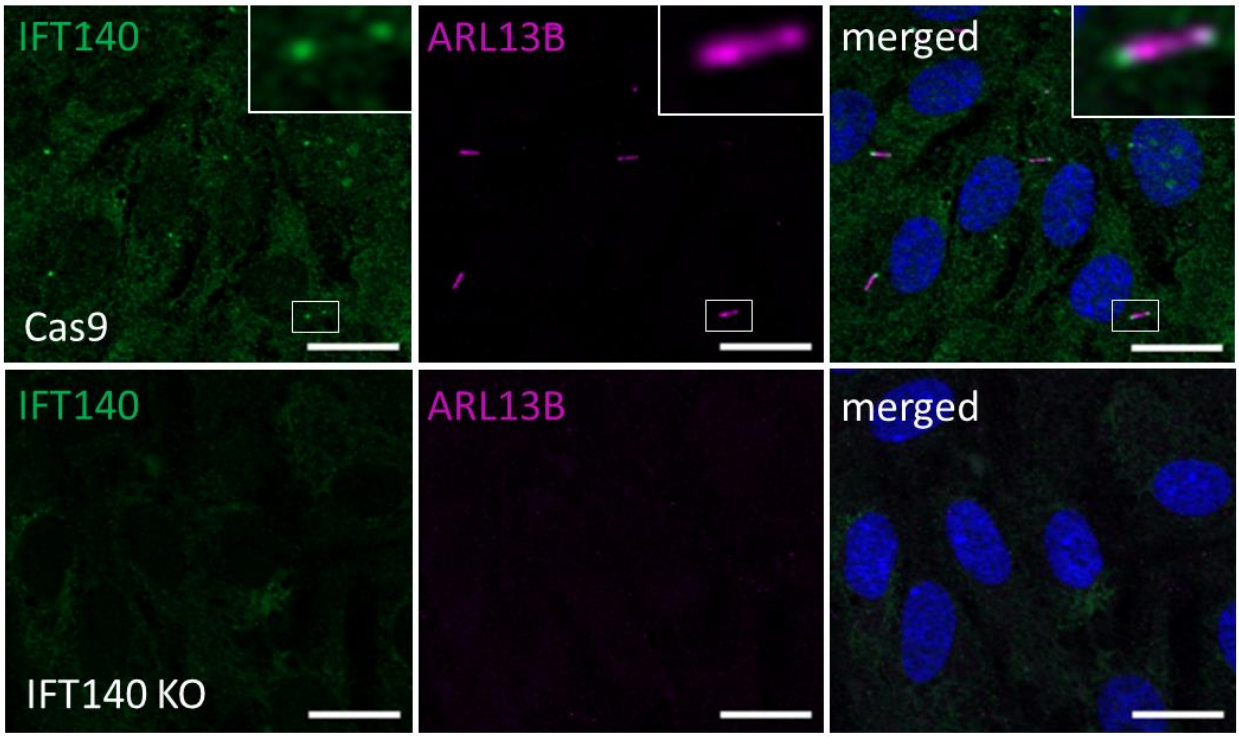

Figure 29: IFT140 knockout in hTERT-RPE1-cells leads to the loss of functional IFT140 at the primary cilium. *(Top) A staining for IFT140 as well as the ciliary marker ARL13B in Cas9-transfected hTERT-RPE1 cells is shown. ARL13B clearly localizes to primary cilia as seen in the ARL13B channel. IFT140 co-localizes with ARL13B at the primary cilium, with a concentration of IFT140 at the ciliary base and tip region. (Bottom) A staining for IFT140 and the ciliary marker ARL13B in IFT140 knockout hTERT-RPE1 cells is shown. No cilia-specific signal for ARL13B is visible. Also, IFT140 does not show any specific localization.*

IFT140 knockout in hTERT-RPE1 cells leads to stimulus-independent activation of hedgehog signaling

In the previous experiments a disruption of the interaction between IFT-A and TULP3 in some of the ciliopathy-associated missense mutations was observed. TULP3 is a known interactor of IFT-A and bridges it to cargo in the ciliary membrane, enabling the transport of the bound cargo from the ciliary base to the ciliary tip [34,35]. Among these cargo proteins are membrane-bound receptors such as several GPCRs. The loss of functional TULP3 can lead to severe clinical manifestations, including neural tube defects, skeletal abnormalities and disturbed kidney function [24,32,80]. One of the GPCRs that depends on functional TULP3 for its proper ciliary localization is GPR161, a negative regulator of hedgehog signaling [34,36]. To assess whether the loss of functional IFT140 has an effect on hedgehog signaling in IFT140 knockout

cells a quantitative RT-PCR was performed to measure the expression level of one of the target genes of the hedgehog signaling pathways. GLI1 is one of the main effectors and is expressed upon activation of the hedgehog signaling pathway [36,80,165]. Using *GLI1* specific primers and *GAPDH* as a negative control the expression levels of both genes in hTERT-RPE1 wildtype and IFT140 knockout cells were analysed. Also, the effect of stimulation of the hedgehog signaling pathway was tested by treatment with extracellular recombinant human shh-ligand on both cell lines. Through the analysis of three biological replicates and three technical replicates for each condition a robust dataset for statistical analysis was obtained. *GLI1* expression was normalized using *GAPDH*. Results are shown in figure 30.

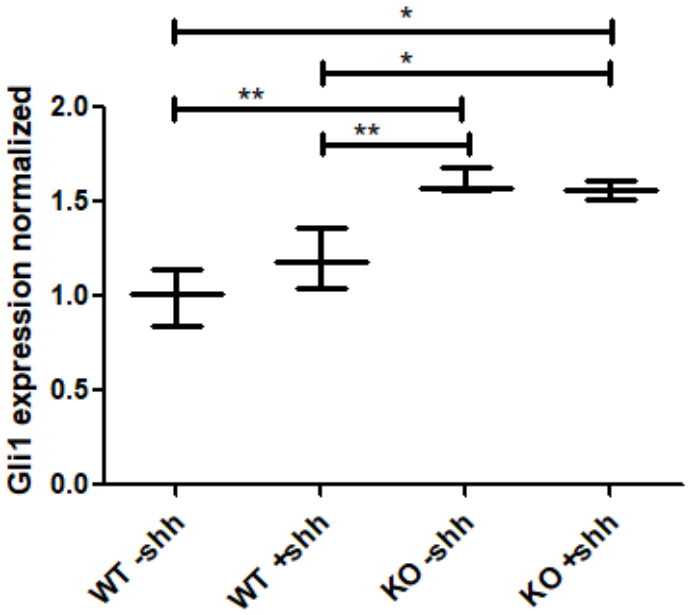

Figure 30: IFT140 knockout cells show expression of hedgehog target genes in the absence of hedgehog stimulation. *The expression levels of GLI1 normalized by GAPDH are shown for hTERT-RPE1 wildtype and IFT140 knockout cells, both in the absence and after stimulation of hedgehog signaling (n=3). IFT140 knockout cells show expression of GLI1 in the absence and presence of hedgehog stimulation. The increase as compared to the wildtype, which shows lower normalized expression levels, is statistically significant (p<0.01). While IFT140 knockout cells show no change in GLI1 expression after stimulation of hedgehog signaling, the expression of GLI1 is slightly increased in wildtype cells after stimulation with recombinant human shh-ligand, but not statistically significant.*

The data reveal that the normalized expression levels of *GLI1* are significantly increased ($p<0.01$) in IFT140 knockout cells as compared to the WT. This increase was observed both in the absence of hedgehog stimulation as well as after stimulus. While the IFT140 knockout cells show no change in *GLI1* expression upon stimulation with extracellular recombinant human shh-ligand, a slight increase was observed in the WT, but was not statistically significant. Taken together the data indicate that hedgehog signaling is activated in IFT140 knockout cells also in the absence of a hedgehog specific stimulation. Considering the importance of functional hedgehog signaling this deregulation may be one of the causes leading to disease in patients affected by disrupted IFT140-TULP3 interaction.

Discussion

In this study the changes in protein interaction networks induced by missense mutations in IFT-A proteins, which facilitates the retrograde trafficking of cargo within the cilium [2,66,166], were examined using a proteomics workflow. Understanding the relationship between genotype and phenotype and disease mechanisms is a major challenge in understanding genetic disorders and is not limited to ciliopathies. Potential mechanisms include e.g. reduced abundance of functional protein, disruption of protein complexes as well as the alteration of specific protein-protein interactions (PPIs), so called edgetic effects [20–22]. Due to the necessity of functional IFT-A during development [6,11,28,82], it seems unlikely that ciliopathy-associated missense mutations on both alleles of a patients lead to a full loss of protein function. It is more plausible, that mutations in these genes cause a loss of function to a limited extent and hence are hypomorph [78].

In the work presented here, valuable new insights into the interaction network of four components of the IFT-A protein complex (IFT43, IFT121, IFT122 and IFT140) were created. In addition, the effects of disease-causing mutations on protein-protein interactions (PPIs) in all four proteins were examined. The generated insights into the effects of ciliopathy-associated missense mutations in IFT-A proteins enable a better understanding of the general mechanisms in recessive Medelian disorders on the molecular level. It also led to a better understanding of the mechanisms, that cause varying types and severity of disease in patients affected by mutations in the same gene.

Analysis of IFT-A wildtype proteins reveals potential new interaction partners

By analysing samples from at least six biological replicates for each condition and stringent statistical filtering (student's t-test p value <0.05 and significance A p-value < 0.05) robust datasets were obtained. This enabled insights in the interaction networks of four components of the IFT-A complex (IFT43, IFT121, IFT122 and IFT140).

In the case of wildtype IFT43 all components of the IFT-A complex were identified as significantly enriched (figure 9; table 9). In addition, the ciliary protein TULP3 was enriched in IFT43 samples, a known interactor of IFT-A [34–36]. This shows that even though IFT43 is no essential part of the IFT-A protein complex and not present in all ciliated organisms, [107] it still is capable of stably binding to the whole complex. Analysis using the STRING database (www.string-db.org) revealed two other known interactors, further confirming the suitability of the method to detect protein interaction partners. These two proteins are TCEAL1, which is a transcriptional regulator [113], and USP11, which participates in the regulation of proteasomal protein degradation via ubiquitination [117]. This indicates a role of USP11 in the combination with IFT43 in the targeting of ciliary proteins for proteasomal degradation, which might be

relevant for the regulation of protein levels and ciliary processes. This hypothesis is further strengthened by the discovery of PIP30 as new potential interactor of IFT43, which is also involved in the process of protein degradation by regulating the activity of proteasomal co-factors [116]. The binding of IFT43 to STXBP1, which is involved in the docking of synaptic vesicles [118], is consistent with the role of IFT-A in the trafficking of vesicles [35,76]. The interaction with the proteins SYPL1 and TYK2, which are involved in the regulation of cell proliferation [114,115], is in accordance with the known role of cilia in cellular signaling [2,8,13,30]. The data presented in this study reveals five new potential interactors of IFT43, that are in accordance with known roles of IFT-A. It puts these proteins for the first time in a ciliary context. This further illuminates the complex interplay between proteins that is necessary for proper function of cilia, which enables crucial cellular processes. The exact nature and functional relevance of these interaction remains to be further investigated.

The analysis of wildtype IFT121 showed that also this component of the IFT-A peripheral complex is able to bind to all components of the IFT-A complex, but not to TULP3 (figure 12; table 11). IFT121 is a large protein consisting of 1181 amino acids and shares several structural features with components of the IFT-A core components. This includes two N-terminal ß-propellers, called WD40 domains, and a TPR domain consisting of several α-helices [29,30]. While the WD40 domains commonly serve as binding sites for other proteins, the TPR domains are crucial for mediating the contact between components of the protein complex [29,76,108]. The C-terminal RING domain may be important for protein ubiquitination [109,111]. These structural features and the fact that IFT121 in contrast to IFT43 is found in all ciliated organisms [30,107], indicate that IFT121 is more ancient and evolutionary more conserved than IFT43. No other known interactors of IFT121 were identified in the obtained dataset, but a total number of 14 potential new interactors (figure 12; table 11). Among these are proteins involved in the regulation of signaling pathways (Rho and EGF-ß) [77,119], cell cycle progression and cytoskeleton organization [120,121,130]. As in the case of the previous analysis of IFT43 this is consistent with the known function of IFT-A. Notably, several of the identified proteins have functions related to the cellular membrane, such as the localization of transmembrane domains [125], the formation of lipid droplets [124], regulation of cholesterol levels [128] and ion channels [129]. This not only highlights the importance of the ciliary membrane but also the complexity of the transport of membrane components and their regulation [2,24,35,42]. The data presented here shed further light on these processes and indicate that IFT121 as component of the peripheral subcomplex might be more relevant for the transport of membrane components within the cilium as reported so far. It might also be possible that IFT43 and IFT121 have different roles in the transport of membrane proteins. While IFT43 e.g. might be involved in the TULP3-mediated transport of membrane cargo, IFT121 might be important for the transport of other

signaling components, e.g. for Rho or TGF-ß signaling. Also, TULP3 might not be detected in samples from IFT121 due to technical reasons.

IFT122 is one of the analysed components of the IFT-A core complex. Its structure is similar to IFT121, but in addition to two WD40, a TPR and a RING domain it also contains a C-terminal Zinc domain [29,30,154]. The analysis of 12 biological replicates led to the identification of 35 proteins that were enriched with IFT122 (figure 15; table 13). Among these are all components of the IFT-A complex as well as IFT27, which is part of the IFT-B complex [30,66]. While it is known that IFT-A and IFT-B are associated to each other [29,30,76,167], a direct interaction of IFT27 with the IFT-A complex has not been reported so far. The analysis using STRING database (www.string-db.org) reveals four additional interaction clusters that were enriched in IFT122 affinity purifications. One of these clusters contains three components of the exocyst complex [143], indicating that IFT122 might be involved in the targeting of post-Golgi vesicles to the plasma membrane and exocytosis. Another interaction cluster contains proteins important for canonical Wnt signaling. Among these are CTNNB1, the key downstream effector of the canonical Wnt signaling pathway [140], and CHD8, which negatively regulates Wnt signaling [142]. The role of primary cilia in Wnt signaling is controversial. Several studies propose that canonical and non-canonical Wnt signaling are independent of primary cilia [98,168–170]. Zebrafish lacking cilia and IFT mutant mice show normal expression of Wnt target genes [171]. Previous studies suggested an inhibition of canonical Wnt signaling through the targeting of the Wnt component Dishevelled for degradation by ciliary inversins [151,172,173]. Additional studies also show an overactivation of Wnt signaling caused by ciliary defects in cell and mouse experiments [170,174,175]. While the role of cilia in canonical Wnt signaling remains disputed, it is evident that proper ciliogenesis and basal body migration are crucial for the planar cell polarity/ non-canonical Wnt signaling pathway [176–178]. Defects in ciliary proteins regulating ciliogenesis and basal body migration lead to neural tube closure defects as well as congenital deafness and retinitis pigmentosa [36,37,80,179]. The data presented here support the relevance of cilia for proper Wnt signaling. The association of components of Wnt signaling to IFT122 indicates a possible role of IFT-A in the targeting of these proteins to the primary cilium or their degradation. The enriched protein WDR11 is involved in the regulation of hedgehog signaling via the proteolytic processing of GLI3 [86] and NFKBIB inhibits the NF-kB signaling pathway [149]. Taken together these data indicate a role of IFT122 in three crucial cellular signaling pathways.

Another interesting cluster contains four proteins important for protein folding, including two members of the heat shock protein family (HSPA2 and HSPA14) [133,136]. Also BAG5 is enriched in IFT122 as well as the protein NUDC, which are also involved in protein folding [132,137,161]. This might indicate problems with folding of IFT122. WD40 domains have been reported to show a high rate of misfolding [180,181]. Hence, the association of several proteins that assist in the correct folding of proteins does not seem surprising. Among the other proteins enriched in

IFT122 are several proteins that are involved in brain development (NCAM1 [127] and LAMB1 [147]) and the nervous system (SHTN1 [146], DOCK7 [144] and LNP [152]). Even though defects in IFT122 have not been reported to lead to anomalies in the development of the nervous system [19,154,155], these data indicate that IFT122 might play a role in axon growth and guidance. The other proteins that were enriched in IFT122 serve several functions, that are consistent with the reported role of IFT-A, including vesicle trafficking, cytoskeleton organization and cell cycle regulation [2,34,36,66,166]. The data presented here not only hint towards new potential interactors of IFT122, but also support the involvement of this IFT-A component in processes such as Wnt signaling, that are still debated in the field and need to be further analysed.

Finally, a second component of the IFT-A core complex was analysed. With a size of 1462 amino acids IFT140 is the largest component of the whole IFT-A complex. Similar to IFT121 and IFT122 it contains two N-terminal WD40 domains and a C-terminal TPR domain, but no Zinc or RING finger domains [30,76]. The large size of about 700 amino acids of the TPR domain and the lack of any other C-terminal domains may indicate that IFT140 differs in its function from IFT121 and IFT122. Due to the size of its TPR domain and the fact that it has physical contact with three components of the IFT-A complex [30,76,166,182] (IFT144, IFT121 and IFT122) it may be especially important for the stability of the complex. For IFT140 the largest number of disease-associated missense mutations has been reported, which lead to an extremely heterogeneous group of diseases [18,23,25,26]. The analysis of a total number of 36 biological replicates led to the identification of 15 enriched proteins in IFT140 affinity purifications (figure 18; table 15) [78]. Same as with the other three analysed proteins, all six components of the IFT-A complex were enriched in IFT140. In addition, the ciliary protein TULP3 was enriched, which is a known interactor of IFT140 [34–36,182]. Also, the known interactor NUDC was enriched, same as in IFT121 and IFT122. Members of the nud gene family are essential for brain cortex development and is known to serve as a co-chaperone in protein folding [132,161]. NUDC might be important for correct folding of IFT140, especially the WD40 domains, to which it is known to bind [108]. This is further supported by the fact that NUDC is associated to all three IFTs examined in this study, that contain WD40 domains [78]. The dataset also indicates seven so far unknown potential interactors of IFT140. Among these is the protein SYNJ2, which was proposed to play a role in membrane trafficking and signal transduction [156]. The association of SYNJ2 with the IFT-A complex might hint towards a role of SYNY2 in the trafficking of membrane bound cargo in a ciliary context, which has not been reported so far. This might explain the previously proposed role of SYNJ2 in signal transduction. Another interesting new interactor of IFT140 is SMG9. It has been implicated in brain, heart and eye development [158]. This is consistent with some of the defects observed in patients suffering from ciliopathies associated with mutations in IFT140 [18,23,25,26]. The exact role of the interaction between IFT140 and SMG9 and its potential role in ciliary function needs to be further evaluated. Among the

other novel identified proteins is PLEC. It is of known importance for interlinking intermediate filaments with microtubules [159]. It might be important for formation of ciliary structures and their stability and require IFT140 for correct function and localization, which could be investigated in the future [78].

In summary, the study presented here further confirmed a number of known protein interactions for all four analysed IFT-A proteins. In addition, it led to the identification of novel potential interactors of IFT-A, shedding a light on possible new functions of several proteins in a ciliary context. Interestingly, an interaction with the ciliary protein TULP3 was only observed in two out of four IFT-A proteins (IFT43 and IFT140). This might indicate that the cargo transport via TULP3 is mediated by just a subset of IFT-A components. It must be noted that the experimental approach used is not suitable to identify all interaction partners, which have been reported previously. In the case of IFT140 for example according to the IntAct database (www.ebi.ac.uk/intact) 26 interactors have been reported so far. 20 of these were not found as enriched in the presented study. One reasons for this may be the requirement of stable binding to the used bait protein during affinity purification, which excludes less stable and transient interactions [101,104,112,183,184]. The statistical analysis used in this approach leads to a stringent filtering of potential interactors, which may exclude other potentially interesting candidates. However, this approach results in a list of bona fide interactors, which is a requirement to allow evaluation of missense mutation-specific changes in the next step.

Missense mutations in IFT-A have a quantitative effect on IFT-A complex stability

The mass spectrometric data revealed that a subset of ciliopathy-associated missense mutations in all four analysed IFT-A proteins have a quantitative effect on IFT-A complex stability. Rather than causing a complete disruption of the protein complex a hypomorph effect was observed, that resulted in reduced binding of components of the IFT-A complex [78]. In the W179R mutant in IFT43, the binding of all five components of the IFT-A complex is reduced, while the abundance of IFT43 is unaltered in the mutant samples (figure 11). In IFT121 for all four mutations a reduced abundance of the bait protein was observed, which may indicate problems with the stability of the protein caused by missense mutations (figure 14). The abundance of the other components of the IFT-A complex is also reduced in all four mutations. In IFT121 a strong reduction in the case of the S168R and D841V mutant is seen (figure 14). This shows that the level of the disruption of the complex integrity varies and occurs in a quantitative manner. This is also observed in IFT122, where e.g. the W7C mutant leads to a mild reduction of IFT139 while not altering the abundance of the other components of IFT-A (figure 17). In the L763P mutant the abundance of the bait protein and other components of the IFT-A core complex are unaltered, while all components of the IFT-A peripheral complex are mildly reduced. Four out of eight mutants (V442L, G546R V553G and G623V) do not alter

the abundance of the bait protein and the other components of the IFT-A core complex, while showing a strong reduction of all components of the IFT-A peripheral complex (figure 17). This further highlights the quantitative nature of the disruptive effect on the IFT-A complex composition. In the S373F mutant the binding of the bait protein as well as all components of the core complex is mildly reduced and all components of the core complex are strongly reduced, while in the F621C mutant the bait protein is mildly reduced and all components of the IFT-A complex strongly reduced. Interestingly, in IFT122 all mutants except W7C show a stronger disruption of all components of the IFT-A peripheral complex as compared to the IFT-A core complex. This indicates that these mutants in IFT122 specifically impair the binding of the IFT-A peripheral complex. According to previous studies, while being part of the IFT-A core complex IFT122 has large areas of physical contact with components of the IFT-A peripheral complex [30,76]. The data presented here support the hypothesis that IFT122 is essential for maintaining contact between the subcomplexes of IFT-A and indicate that this contact is impaired by mutations in IFT122.

In the case of IFT140 seven out of 24 of the analysed mutations (V108M, G140R, A341T, G522E, E664K, C663W, S939P) impair the stability of the IFT-A complex, leading to a partial disruption (figure 21). Also for IFT140 quantitative effects on the IFT-A complex composition can be observed [78]. Due to the importance of functional IFT-A for retrograde trafficking of cargo towards the basal body [30,34,45,185], the disruption of the complex might explain some of the defects observed in patients harbouring these mutations. The data presented here show for the first time that disease-associated missense mutations can affect specific PPIs in a quantitative manner to varying degree.

Disease-associated missense mutations in IFT-A are edgetic and disrupt specific protein interactions

The potential effect of amino acid changes on protein-protein interactions is known and has been observed for a broad variety of proteins [21,112,186]. One model to explain these alterations is the edgetic concept, in which mutations lead to the loss of specific PPIs (edge loss) rather than to a total loss of function of the affected protein (node loss) [20–22]. The data presented here show that mutations in IFT-A proteins can impair specific interactions within a protein interaction network. The analysis of missense mutations in four different proteins revealed that 34 out of 37 analysed mutations lead to the disruption of specific PPIs. For three out of 24 mutations in IFT140 (G212R, C329R and A418P) no change in the binding of wildtype interactors has been observed (figure 23). It may still be possible that these mutations impact specific PPIs that were not identified by the used experimental approach or that additional mutations or modifiers are relevant. In no case a total loss of all wildtype interaction partners

was observed. This is consistent with the edgetic hypothesis and further strengthens the idea of edge removal in protein interaction networks induced by missense mutations [78].

A striking example for edgetic effects of missense mutations observed in this study is the interaction between IFT140 and TULP3. A total number of seven out of 24 mutations (V108M, G140R, E267G, V292M, A341T, C663W, S939P) in IFT140 in AP-experiments led to a disruption of the binding of TULP3 to IFT-A (figure 21 and figure 23). For four out of 24 mutations (G212R, Y311C, C329R, C333Y) the interaction with TULP3 remained unchanged in comparison to the WT. For the other 13 out of 24 mutations no quantification for TULP3 was possible in the MS/MS-experiments. The interaction of IFT140 and TULP3 was further validated via co-immunoprecipitation for 15 out of 25 mutations, including all homozygotes and all mutations for which a TULP3 ratio could be obtained in the proteomics experiment. The degree of the loss of TULP3 varied between mutations in co-immunoprecipitation experiments (figure 25 and 26). This indicates that the loss is not complete, but rather that mutations in IFT140 reduce the interaction with TULP3 to varying degrees. For the homozygous mutations a mild disruption of the interaction with TULP3 could be observed for C333Y and to a stronger extent for I233M (figure 26). For the homozygous mutations T484M and E664K a stronger disruption was observed in the interaction between IFT140 and TULP3 [78]. Differences in the binding of TULP3 observed between the mass spectrometry and the co-immunoprecipitation may have different reasons. Protein detection via specific antibodies is commonly more sensitive than the applied bottom-up proteomics approach [187]. In addition, for the co-immunoprecipitation the HEK293 cells were co-transfected with a TULP overexpression vector. Therefore, TULP3 is expressed at higher levels in the co-immunoprecipitation samples than in native condition and more likely to be detected on the protein level.

Notably, the data presented in this study indicate that the disruption of the interaction between IFT-A and TULP3 can occur via two different mechanisms [78] (figure 20 and figure 21). The disruption of the IFT-A complex integrity by a missense mutation in IFT140 not only leads to a reduced binding of components of the IFT-A complex, but also results in a loss of TULP3 (figure 21). This was observed for all four mutations in IFT140 for which a quantification of TULP3 was possible (C663W, V108M, G140R and A341T) and which showed a reduced binding of IFT-A components as compared to the WT. In no case similar levels of TULP3 as compared to the WT were observed for mutants, that lead to a reduction of IFT-A components [78]. This is consistent with previous reports that TULP3 binds to the IFT-A complex [30,34,35,182]. This study revealed that missense mutations in IFT140 have edgetic effects on the interaction with TULP3 and can disrupt binding of TULP3 to IFT-A without altering the composition of the complex itself [78] (figure 21). This is the case for three out of seven mutations (S939P, V292M and E267G), that show an unaltered binding of IFT-A component as compared to the WT and for which a quantification of TULP3 was possible. Previous studies suggested that the

interaction of TULP3 with the IFT-A complex is mainly mediated by IFT122 and only to a minor degree by IFT140 [30,76]. The data presented here indicate that IFT140 is crucial for proper binding of TULP3 and that single amino acid exchanges can impair this interaction without altering the IFT-A complex composition [78].

Keeping in mind the importance of the IFT140/TULP3 interaction during development [34–36], the question arises if reduced TULP3 interaction results in a reduction of signaling. Also, a reduction of TULP3 binding via IFT140 might be compensated to a certain degree by other IFT-A components. Knockout of Tulp3 in mice leads to disturbed eye development, neural tube defects and other developmental defects [37,80], which shows a clinical overlap with some of the observed defects in patients suffering from IFT140-associated ciliopathies [18,23,25,26]. In hTERT-RPE1 cells, knockout of TULP3 leads to defective cilia formation [24,188]. Based on this knowledge a total loss of TULP3 dependent signaling is unlikely. However, other IFT-A complex proteins might compensate the function of IFT140 to a certain extent. Interestingly, the T484M mutation, which results in a milder phenotype, shows normal IFT-A binding, whereas E664K showed loss of IFT-A and TULP3 and resulted in additional skeletal defects (figure 21 and table 17) [78]. It was also shown that TULP3 bridges the IFT-A complex to the ciliary membrane, which promotes trafficking of components important for hedgehog signaling, such as GPR161, a negative regulator of hedgehog signaling pathway [24,35,36,83]. In cells lacking TULP3 in their primary cilia due to knockout of IFT-A components also GPR161 was absent from the cilium [34]. Primary cilia are essential for functional hedgehog signaling [13,35,82,86]. Defects in hedgehog signaling have been reported to be involved in several ciliopathies, including retinal dystrophies as well as skeletal abnormalities and organ damage [5,7,189]. The ciliary dislocation of these proteins caused by the disrupted IFT140/TULP3 interaction might provide a possible explanation on how IFT140 defects lead to skeletal abnormalities and organ defects in patients [78]. However, due to the low number of patients it should be further validated, to what extent TULP3-dependent signaling is affected by specific mutations [78]. In addition, it remains unknown if this effect is also observed *in vivo*, which should be examined in future experiments.

Edgetic effects are not domain specific

The question if the disruption of specific protein interactions is domain specific was exemplary assessed for IFT140, for which the largest number of missense mutations was analysed [78]. IFT140 has three main domains: two separate WD40 domains at the N-terminus and a C-terminal TPR repeat (figure 4 and figure 7). Mutations that impair the IFT-A complex integrity are found in all three domains of IFT140 (figure 21). In the first WD40 domain, three out of 11 mutants (V108M, G140R and A341T) show a mild reduction in the binding of the remaining five IFT-A components in relation to the bait protein IFT140. In the second WD40 domain two out of six mutants (G522E and E664K) show a strong disruption of the IFT-A complex integrity,

while C663W shows a mild reduction of four IFT-A components and a loss of IF43. The mutant L1399P, which is located in the TPR domain, also shows a strong disruption of the IFT-A complex integrity, while the other six mutants show no alterations. In the case of TULP3 and SMG9 mutations, that lead to a strong reduction are found in all three domains. For the protein STX8 disruptive mutations can be found in the first WD40 domain as well as the TPR domain. For the proteins SPAG7, and SYNJ2 strongly disruptive mutations can be found in only one domain, in the first WD40 in the case of SYNJ2 and in the TPR domain for SPAG7. Taken together, these data indicate that the disruption of IFT-A complex integrity as well as several PPIs is not limited to mutations in one specific domain of IFT140. Similar effects can be observed for IFT121 and IFT122, while due to the low number of tested mutations no statement can be made for IFT43. The mechanisms leading to the disruption of specific PPIs appear to be more complex and result from a combination of different factors. This may include changes in protein structure and stability as well as the interplay with other components of the complex and interaction partners. Reduced protein stability or problems with proper folding may lead to lower amounts of functional protein. The exchange of amino acids might also lead to changes in the protein structure. Also, it needs to be considered that in the 3D protein structure amino acids that are at different positions in the amino acid sequence might still be in close proximity within the folded protein. The combined effect of all relevant mechanisms may decide the final outcome on each specific PPI.

Impairment of IFT-A complex composition is specific to disease-associated missense mutations and shows a genotype-phenotype correlation in patients

34 out of 37 of the analysed disease-associated missense mutations show a disruption of specific protein interactions (figure 11, figure 14, figure 17 and figure 23). This is most evident in the case of the IFT-A complex itself, where a quantitative effect on the IFT-A complex composition was observed in all four proteins. The question arises, whether this effect is a specific result of the analysed disease-associated mutations or due to the applied experimental approach. To assess this question, the effect of single nucleotide polymorphisms (SNPs) in IFT140 was assessed using the same experimental approach. Six SNPs from all three domains of IFT140 were selected, which all occur as homozygotes in at least one healthy individual according to the gnomAD database (www.gnomad.broadinstitute.org). The resulting amino acid exchanges caused by these SNPs are comparable in severity regarding the differences in the chemical and sterical properties (www.insilicase.com/) to the ones caused by disease-associated missense mutations in IFT140 [190]. The data revealed that all six analysed SNPs did not show any alterations in the composition of the IFT-A complex as compared to the WT [78] (figure 22). The observed quantitative effects on the complex composition therefore appear to be specific to the disease-associated missense mutations in IFT140. This observation raises the question, what exactly separates disease-associated

missense mutations from SNPs. The data presented here demonstrate that even severe exchanges of amino acids, which largely differ in their chemical and sterical properties (e.g. glycin to arginine), do not necessarily lead to a disease phenotype. Therefore, it is unlikely that the clinical outcome of a missense mutations can be predicted only by comparing the chemical and sterical similarity of exchanged amino acids. The analysis of changes of PPIs as performed in this study might be one way to analyse the specific effect of a missense mutation. Due to technical limitations of affinity-purification and MS-analysis not all relevant changes on the protein level caused by a mutation might be captured by the approach used in this work. Until all mechanisms deciding the clinical outcome are understood, it remains necessary to experimentally assess the effect of each individual amino exchange on PPIs.

So far the data show that missense mutations in IFT140 have quantitative effects on the integrity of the IFT-A complex and that this effect is specific to disease-associated missense mutations. Subsequently it was examined whether the severity of this impairment contributes to the severity of the clinical phenotype observed in affected patients. Interestingly, a correlation between genotype and phenotype in eight patients carrying missense mutations on both alleles of IFT140 was observed (table 17). Patients who harbour two mutations that are mildly or undisruptive for the IFT-A integrity on both alleles also show milder clinical phenotypes. The disease severity is increased when one allele harbours a missense mutation, which shows a strong disruption of IFT-A complex integrity in the MS-experiments. Patients with IFT-A-disruptive missense mutations on both alleles show the strongest phenotypes. This observation hints towards a clear correlation between the severity of PPI disruption observed in the experiments and the disease severity observed in affected patients [78].

It also indicates that the combination of missense mutations affects the phenotype, as seen in the case of the T484M mutation (table 17). While a patient carrying a non-disruptive biallelic T484M mutation shows isolated retinal dystrophy, a patient harbouring the same T484M mutation in combination with the more disruptive C329R mutation was diagnosed with LCA. This more severe phenotype is characterized by early-onset of blindness [12,91,191] and may be due to the more severe inhibition of IFT-A dependent trafficking and signaling caused by the allelic combination, indicating genetic threshold effects that define disease severity [78].

In this study also the ability of a shorter isoform of IFT140 isoform to rescue the composition of the IFT-A complex was examined. The shorter isoform still contains the majority of the TPR domain of the full-length construct and might be able to ensure the integrity of the IFT-A independent of the full length isoform (figure 24 A). This might be relevant e.g. when a mutation, that is only present in the full length isoform, induces misfolding, which would only affect the full length protein. This question was assessed by performing an affinity-purification and comparing the enriched proteins in samples from the full length and short isoforms of

IFT140. It revealed that the shorter isoform does not bin to four out of six components (IFT121, IFT122, IFT139 and IFT144) of the IFT-A complex and only stably binds to IFT43 (figure 24 B). This shows that it is highly unlikely that the short isoform is sufficient to rescue the complex integrity when the full-length isoform loses its ability to mediate contact with the complex due to missense mutations. This further supports the hypothesis that the disruptive effect of missense mutations observed in the full-length form of IFT140 is a defining factor for disease severity and shows no domain specific cluster, since it is not rescued by another isoform of IFT140.

Loss of IFT140 leads to absent ciliary ARL13B

For functional analysis of IFT140 a CRISPR/Cas9-mediated knockout of IFT140 was generated in hTERT-RPE1. The loss of full length IFT140 in the knockout was confirmed by western blot analysis with lysates from wildtype or knockout hTERT-RPE1 cells (figure 28). The generated IFT140 knockout cells and Cas9-transfected wildtype cells as a negative control were used for immunofluorescence staining and microscopy using an IFT140-specific antibody. An antibody for the protein ARL13B was used as a marker for primary cilia [31,82,93,188]. As reported previously IFT140 co-localized with ARL13B at the primary cilium, with a concentration at the ciliary base and tip region [26,33] (figure 29). This not only confirms previous reports of the specific localization of IFT140 at the cilium, but also demonstrates the suitability of the used antibodies to detect signals specific for IFT140 and ARL13B. In contrast to the control cells in the IFT140 knockout cells no specific signal was observed for neither IFT140 nor ARL13B (figure 29). This finding further confirms the successful knockout generation. Previous publications reported that IFT140 knockout leads to shortened cilia with a bulged appearance in IMCD3 cells rather than a total loss of cilia [33,93]. The loss of the ARL13B specific signal in IFT140 knockout cells may be due to the loss of ARL13B within the primary cilium. It has been reported that TULP3 knockout leads to loss of IFT140 within the cilium in cells [188]. Since TULP3 depends on functional IFT-A for the transport of cargo proteins [34–36], a knockout of IFT-A components may have similar effects. Hence the observed loss of ARL13B specific signal might be due to the loss of ARL13B at the cilium rather than the total loss of cilia in the knockout cells. This should be further examined using other antibodies for other cilia-specific proteins such as acetylated tubulin [192,193].

Knockout of IFT140 leads to overactivation of hedgehog signaling

The mass spectrometric analysis as well as the co-immunoprecipitation showed that the interaction between IFT-A and the ciliary protein TULP3 is impaired by a subset of seven out of eleven missense mutations in IFT140 (figure 21, figure 25 and figure 26). TULP3 is necessary for the transport of several signaling components within the cilium. This includes the transmembrane protein GPR161, a negative regulator of the hedgehog signaling pathway.

Loss of TULP3 leads to the loss of GPR161 in the cilium and the transport of GPR161 also depends on functional IFT-A [24,35,36,188]. Since functional hedgehog signaling is essential for correct tissue development and homeostasis defects in this crucial pathway can lead to a variety of clinical defects [31,35,40,82]. This includes neural tube closure defects as well as skeletal abnormalities, showing an overlap with some of the observed clinical features in patients affected by IFT-A related ciliopathies [18,23,26,80,165,194]. The observed disruption of the interaction between TULP3 and IFT-A caused by missense mutations in IFT140 may also effect the transport of GPR161 via TULP3, leading to an activation of hedgehog signaling in the absence of a stimulus[78]. The question if the knockout of IFT140 has an effect on hedgehog signaling and therefore might be relevant in the disease mechanism of IFT140 missense mutations was assessed using the generated hTERT-RPE1 knockout cells. Via a quantitative qPCR the expression of the hedgehog target gene *GLI1* was analysed, which is expressed upon stimulation of the hedgehog signaling pathway [36,38,80,195]. The data revealed that *GLI1* is expressed on significantly higher levels in the knockout cells as compared to the wildtype control (figure 30). This is true both in the presence and in the absence of hedgehog stimulation with recombinant human sonic hedgehog ligand. This is evidence of an increased expression of hedgehog target genes in IFT140 knockout cells. Upon stimulation with extracellular recombinant human sonic hedgehog ligand the expression of *GLI1* is unaltered in the knockout but increased in the wildtype. However, the observed increase of the *GLI1* expression in the wildtype is not statistically significant. This may indicate that higher concentrations of sonic hedgehog ligand are necessary for proper pathway stimulation in the used assay. In summary, the data presented here show that knockout of IFT140 in hTERT-RPE1 cells leads to an increased expression of *GLI1*, which indicates an overactivation of the hedgehog signaling pathway. This hints towards a potential mechanism through which mutations, that disrupt the interaction between IFT-A and TULP3, may lead to disease. The functional relevance of this effect and the ability of the different IFT140 mutants to rescue this phenotype should be further investigated in the future.

Conclusion

The data presented in this study show that disease-associated missense mutations in four components of the IFT-A complex (IFT43, IFT121, IFT122 and IFT140) impair specific protein-protein interactions (PPIs). The disruption of specific PPIs, as shown here e.g. for TULP3, further strengthens the idea of edgetic perturbations caused by disease-associated mutations. It also allows to link a subset of mutations to specific potential disease mechanisms like hedgehog signaling [78].

This work examined the effect of disease-associated mutations via a systematic analysis of in total 37 missense mutations in IFT-A. It shows that missense mutations have quantitative effects on specific interactions, as demonstrated here for the composition of the IFT-A complex. This might hamper the complex and limit its ability to function properly, potentially leading to transport defects resulting in mislocalization of important cargo for proper ciliary function. The impairment of the IFT-A complex integrity is specific for disease-associated missense mutations and not observed in single nucleotide polymorphisms in IFT140. A shorter isoform of IFT140 does not bind to all components of the IFT-A complex and therefore is unlikely to rescue defects caused by mutations that are only present in the full-length isoform.

The genotype severity of the IFT-A complex disruption observed in the MS-experiments also allows to establish a correlation between genotype and clinical phenotype. The disruption of different PPIs to a varying degree as well as the allelic combination might explain the clinical variation observed in patients regarding type, severity and tissue specificity of the observed ciliopathies. Since the experiments were conducted in HEK293 cells these finding need to be further validated in the future in a more suitable model system, e.g. patient-derived cells or *in vivo* models [78].

The presented data shed light on two relevant disease mechanisms: edgetic effects and quantitative impairment of the complex composition. While improving the understanding of the general mechanisms of genetic disease, this also highlight their complexity and indicates the existence of additional effects, which have not been identified so far. One possibility might be threshold effects caused by altered levels of functional protein, which could include folding defects caused by mutations, leading to the degradation of protein in the cell or the accumulation of misfolded protein with limited functionality. In addition, it seems likely that at least for some of the existing disease mechanisms, compensatory effects or modifiers are relevant, e.g. chaperones. Additional research is necessary to further illuminate these interplays [78]. However, the understanding of shh signaling in development of IFT-A related diseases might be a therapeutical target, which does not rely on single mutation correction. This might enable treatment in a more general way via pharmacological intervention in patients, also to stop disease progression in patients already affected by disease.

References

1. Avasthi, P. & Marshall, W. F. Stages of ciliogenesis and regulation of ciliary length. *Differentiation* **83**, S30–S42 (2012).

2. Ishikawa, H. & Marshall, W. F. Ciliogenesis: Building the cell's antenna. *Nat. Rev. Mol. Cell Biol.* **12**, 222–234 (2011).

3. Berbari, N. F., O'Connor, A. K., Haycraft, C. J. & Yoder, B. K. The Primary Cilium as a Complex Signaling Center. *Curr. Biol.* **19**, R526–R535 (2009).

4. Ching-Hwa Sung & M., D. M. The roles of evolutionarily conserved functional modules incilia-related trafficking. *Bone* **23**, 1–7 (2011).

5. Anvarian, Z., Mykytyn, K., Mukhopadhyay, S., Pedersen, L. B. & Christensen, S. T. Cellular signalling by primary cilia in development, organ function and disease. *Nat. Rev. Nephrol.* **15**, 199–219 (2019).

6. Hildebrandt, F., Benzing, T. & Katsanis, N. Ciliopathies: An expanding disease spectrum. *N Engl J Med.* **364**, 1533–1543 (2011).

7. Waters, A. M. & Beales, P. L. Ciliopathies: An expanding disease spectrum. *Pediatr. Nephrol.* **26**, 1039–1056 (2011).

8. Pazour, G. J. & Witman, G. B. The vertebrate primary cilium is a sensory organelle. *Curr. Opin. Cell Biol.* **15**, 105–110 (2003).

9. Satir, P. & Christensen, S. T. Overview of structure and function of mammalian cilia. *Annu. Rev. Physiol.* **69**, 377–400 (2007).

10. Lee, J. & Chung, Y. D. Ciliary subcompartments: How are they established and what are their functions? *BMB Rep.* **48**, 380–387 (2015).

11. Rosenbaum, J. L. & Witman, G. B. Intraflagellar transport. *Nat. Rev. Mol. Cell Biol.* **3**, 813–825 (2002).

12. Boldt, K. *et al.* Disruption of intraflagellar protein transport in photoreceptor cilia causes Leber congenital amaurosis in humans and mice. *J. Clin. Invest.* **121**, 2169–2180 (2011).

13. Wheway, G., Nazlamova, L. & Hancock, J. T. Signaling through the primary cilium. *Front. Cell Dev. Biol.* **6**, 1–13 (2018).

14. Rohatgi, R. & Snell, W. J. The ciliary membrane. *Curr. Opin. Cell Biol.* **22**, 541–546 (2010).

15. Reiter, J. F. & Leroux, M. R. Genes and molecular pathways underpinning ciliopathies. *Nat. Rev. Mol. Cell Biol.* **18**, 533–547 (2017).

16. Forbes, T. A. *et al.* Patient-iPSC-Derived Kidney Organoids Show Functional Validation of a Ciliopathic Renal Phenotype and Reveal Underlying Pathogenetic Mechanisms. *Am. J. Hum. Genet.* **102**, 816–831 (2018).

17. Walczak-Sztulpa, J. *et al.* Cranioectodermal Dysplasia, Sensenbrenner Syndrome, Is a Ciliopathy Caused by Mutations in the IFT122 Gene. *Am. J. Hum. Genet.* **86**, 949–956 (2010).

18. Priest, J. R. *et al.* De Novo and Rare Variants at Multiple Loci Support the Oligogenic Origins of Atrioventricular Septal Heart Defects. *PLoS Genet.* **12**, 1–25 (2016).

19. Alazami, A. M., Seidahmed, M. Z., Alzahrani, F., Mohammed, A. O. & Alkuraya, F. S. Novel IFT122 mutation associated with impaired ciliogenesis and cranioectodermal dysplasia. 2011–2014 (2013) doi:10.1002/mgg3.44.

20. N. Sahni, M. Taipale, M. V. Widespread Macromolecular Interaction Perturbations in Human Genetic Disorders. *Physiol. Behav.* **176**, 139–148 (2017).

21. Wang, Y., Sahni, N. & Vidal, M. Global Edgetic Rewiring in Cancer Networks. *Cell Syst.* **1**, 251–253 (2015).

22. Zhong, Q. *et al.* Edgetic perturbation models of human inherited disorders. *Mol. Syst. Biol.* **5**, (2009).

23. Hull, S. *et al.* Nonsyndromic retinal dystrophy due to bi-allelic mutations in the ciliary transport gene IFT140. *Investig. Ophthalmol. Vis. Sci.* **57**, 1053–1062 (2016).

24. Hong, J. J. *et al.* Differential roles of tubby family proteins in ciliary formation and trafficking. *Mol. Cells* **44**, 591–601 (2021).

25. Peña-Padilla, C. *et al.* Compound heterozygous mutations in the IFT140 gene cause Opitz trigonocephaly C syndrome in a patient with typical features of a ciliopathy. *Clin. Genet.* **91**, 640–646 (2017).

26. Perrault, I. *et al.* Mainzer-saldino syndrome is a ciliopathy caused by IFT140 mutations. *Am. J. Hum. Genet.* **90**, 864–870 (2012).

27. Liang, Y., Meng, D., Zhu, B. & Pan, J. Mechanism of ciliary disassembly. *Cell. Mol. Life Sci.* **73**, 1787–1802 (2016).

28. Zhu, B. *et al.* Functional exploration of the IFT-A complex in intraflagellar transport and ciliogenesis. *PLoS Genet.* **13**, 1–20 (2017).

29. Hesketh, S. J., Mukhopadhyay, A. G., Nakamura, D., Toropova, K. & Roberts, A. J. IFT-A Structure Reveals Carriages for Membrane Protein Transport into Cilia. *bioRxiv* 2022.08.09.503213 (2022).

30. Nakayama, K. & Katoh, Y. Architecture of the IFT ciliary trafficking machinery and interplay between its components. *Crit. Rev. Biochem. Mol. Biol.* **55**, 179–196 (2020).

31. Larkins, C. E., Gonzalez Aviles, G. D., East, M. P., Kahn, R. A. & Caspary, T. Arl13b regulates ciliogenesis and the dynamic localization of Shh signaling proteins. *Mol. Biol. Cell* **22**, 4694–4703 (2011).

32. Legué, E. & Liem, K. F. Tulp3 Is a Ciliary Trafficking Gene that Regulates Polycystic Kidney Disease. *Curr. Biol.* **29**, 803-812.e5 (2019).

33. Oud, M. M. *et al.* Cellular ciliary phenotyping indicates pathogenicity of novel variants in IFT140 and confirms a Mainzer-Saldino syndrome diagnosis. *Cilia* **7**, 1–9 (2018).

34. Hirano, T., Katoh, Y., Nakayama, K. & Marshall, W. Intraflagellar transport - A complex mediates ciliary entry and retrograde trafficking of ciliary G protein-coupled receptors. *Mol. Biol. Cell* **28**, 429–439 (2017).

35. Mukhopadhyay, S. *et al.* TULP3 bridges the IFT-A complex and membrane phosphoinositides to promote trafficking of G protein-coupled receptors into primary cilia. *Genes Dev.* **24**, 2180–2193 (2010).

36. Mukhopadhyay, S. *et al.* The ciliary G-protein-coupled receptor Gpr161 negatively regulates the sonic hedgehog pathway via cAMP signaling. *Cell* **152**, 210–223 (2013).

37. Ikeda, A., Ikeda, S., Gridley, T., Nishina, P. M. & Naggert, J. K. Neural tube defects and neuroepithelial cell death in Tulp3 knockout mice. *Hum. Mol. Genet.* **10**, 1325–1334 (2001).

38. Briscoe, J. & Thérond, P. P. The mechanisms of Hedgehog signalling and its roles in

development and disease. *Nat. Rev. Mol. Cell Biol.* **14**, 418–431 (2013).

39. Reynolds, R. M. *et al.* Patched1 Regulates Hedgehog Signaling at the Primary Cilium. 372–376 (2007).

40. Choudhury, A., Neumann, N. M., Raleigh, D. R. & Lang, U. E. Clinical Implications of Primary Cilia in Skin Cancer. *Dermatol. Ther. (Heidelb).* **10**, 233–248 (2020).

41. Yuan, S. & Sun, Z. Expanding horizons: Ciliary proteins reach beyond cilia. *Annu. Rev. Genet.* **47**, 353–376 (2013).

42. Nakayama, K. & Katoh, Y. Ciliary protein trafficking mediated by IFT and BBSome complexes with the aid of kinesin-2 and dynein-2 motors. *J. Biochem.* **163**, 155–164 (2018).

43. Reynolds, M. J. *et al.* The Developmental Process of the Growing Motile Ciliary Tip Region. *Sci. Rep.* **8**, 1–10 (2018).

44. Sánchez, I. & Dynlacht, B. D. Cilium assembly and disassembly. *Nat. Cell Biol.* **18**, 711–717 (2016).

45. Pazour, G. J. & Rosenbaum, J. L. Intraflagellar transport and cilia-dependent diseases. *Trends Cell Biol.* **12**, 551–555 (2002).

46. Satir, P. & Sleigh, M. A. The physiology of cilia and mucociliary interactions. *Annu. Rev. Physiol.* **52**, 137–155 (1990).

47. Kee, H. L. *et al.* A size-exclusion permeability barrier and nucleoporins characterize a ciliary pore complex that regulates transport into cilia. *Nat. Cell Biol.* **14**, 431–437 (2012).

48. Kohli, P. *et al.* The ciliary membrane-associated proteome reveals actin-binding proteins as key components of cilia. *EMBO Rep.* **18**, 1521–1535 (2017).

49. Mitchison, H. M. & Valente, E. M. Motile and non-motile cilia in human pathology: from function to phenotypes.

50. Williantarra, I., Richardo, T., Kumalasari, I. & Devanthi, P. V. P. An overview of the primary cilium and rpgrip1l: The signalling hub's anchor for organ development and homeostasis. *Malaysian J. Fundam. Appl. Sci.* **17**, 582–592 (2021).

51. Angeles, L. The renewal of photorecept o r cell outer segments. *J. Cell Biol.* **33**, 61–72 (1967).

52. Young, R. W. The renewal of photoreceptor cell outer segments. *J. Cell Biol.* **33**, 61–72 (1967).

53. Crouse, J. A. *et al.* Distinct functions for IFT140 and IFT20 in opsin transport. *Cytoskeleton* **71**, (2014).

54. Kefalov, J.-S. W. and V. J. The Cone-specific Visual Cycle. *Bone* **23**, 1–7 (2011).

55. Marc, R. E., Jones, B. W., Watt, C. B. & Strettoi, E. Neural remodeling in retinal degeneration. *Prog. Retin. Eye Res.* **22**, 607–655 (2003).

56. Baylor, D. A., Lamb, T. D. & Yau, K.-W. The membrane current of single rod outer segments. *Vision Res.* **19**, 355 (1979).

57. Flock, H. R. Jameson and Hurvich's theory of brightness contrast. *Percept. Psychophys.* **8**, 118–124 (1970).

58. Baylor, D. A., Lamb, T. D. & Yau, K. W. Responses of retinal rods to single photons. *J. Physiol.* **288**, 613–634 (1979).

59. Liu, Q., Lyubarsky, A., Skalet, J. H., Jr, E. N. P. & Pierce, and E. A. RP1 is required for the

correct stacking of outer segment discs. *Early Hum. Dev.* **83**, 1–11 (2013).

60. Rosenbaum, J. L., Cole, D. G. & Diener, D. R. Intraflagellar Transport: The Eyes Have It. *J. Cell Biol.* **144**, 385–388 (1999).

61. Cavodeassi, F., Creuzet, S. & Etchevers, H. C. The hedgehog pathway and ocular developmental anomalies. *Hum. Genet.* **138**, 917–936 (2019).

62. Cote, R. *Photoreceptor Phosphodiesterase (PDE6):A G-Protein-Activated PDERegulating Visual Excitationin Rod and ConePhotoreceptor Cells*. *Cyclic Nucleotide Phosphodiesterases in Health and Disease* (2006). doi:10.1201/9781420020847.ch8.

63. Gupta, G. D. *et al.* A Dynamic Protein Interaction Landscape of the Human Centrosome-Cilium Interface. *Cell* **163**, 1484–1499 (2015).

64. Rieder, C. L., Jensen, C. G. & Jensen, L. C. W. The resorption of primary cilia during mitosis in a vertebrate (PtK1) cell line. *J. Ultrasructure Res.* **68**, 173–185 (1979).

65. Reiter, J. F., Blacque, O. E. & Leroux, M. R. The base of the cilium: Roles for transition fibres and the transition zone in ciliary formation, maintenance and compartmentalization. *EMBO Rep.* **13**, 608–618 (2012).

66. Santos, N. & Reiter, J. F. Building it up and taking it down: The regulation of vertebrate ciliogenesis. *Dev. Dyn.* **237**, 1972–1981 (2008).

67. Taschner, M., Bhogaraju, S. & Lorentzen, E. Architecture and function of IFT complex proteins in ciliogenesis. *Differentiation* **83**, S12–S22 (2012).

68. Singh, S., Gui, M., Koh, F., Yip, M. C. J. & Brown, A. Structure and activation mechanism of the BBsome membrane protein trafficking complex. *Elife* **9**, 1–22 (2020).

69. Garcia-Gonzalo, F. R. & Reiter, J. F. Scoring a backstage pass: Mechanisms of ciliogenesis and ciliary access. *J. Cell Biol.* **197**, 697–709 (2012).

70. Sorokin, S. Centrioles and the formation of rudimentary cilia by fibroblasts and smooth muscle cells. *J. Cell Biol.* **15**, 363–377 (1962).

71. Quarmby, L. M. & Parker, J. D. K. Cilia and the cell cycle? *J. Cell Biol.* **169**, 707–710 (2005).

72. Carvalho-Santos, Z., Azimzadeh, J., Pereira-Leal, J. B. & Bettencourt-Dias, M. Tracing the origins of centrioles, cilia, and flagella. *J. Cell Biol.* **194**, 165–175 (2011).

73. Wang, G. *et al.* PCM1 recruits Plk1 to the pericentriolar matrix to promote primary cilia disassembly before mitotic entry. *J. Cell Sci.* **126**, 1355–1365 (2013).

74. Yi, H., Nakamura, R. E. I., Mohamed, O., Dufort, D. & Hackam, A. S. Characterization of Wnt signaling during photoreceptor degeneration. *Investig. Ophthalmol. Vis. Sci.* **48**, 5733–5741 (2007).

75. Pugacheva, E. N., Jablonski, S. A., Hartman, T. R., Henske, E. P. & Golemis, E. A. HEF1-Dependent Aurora A Activation Induces Disassembly of the Primary Cilium. *Cell* **129**, 1351–1363 (2007).

76. Jenna L. Wingfield, Karl-Ferdinand Lechtreck, E. L. Trafficking of ciliary membrane proteins by the intraflagellar transport/BBSome machinery. *Cell* **185**, 2022.08.09.503213 (2022).

77. Seong, H. A., Jung, H., Kim, K. T. & Ha, H. 3-Phosphoinositide-dependent PDK1 negatively regulates transforming growth factor-β-induced signaling in a kinase-dependent manner through physical interaction with Smad proteins. *J. Biol. Chem.* **282**, 12272–12289 (2007).

78. Leonhard, T. *et al.* Ciliopathy-associated missense mutations in IFT140 are hypomorphic and have edgetic effects on protein interaction networks. (2023).

79. Bisgrove, B. W. & Yost, H. J. The roles of cilia in developmental disorders and disease. *Development* **133**, 4131–4143 (2006).

80. Norman, R. X. *et al.* Tubby-like protein 3 (TULP3) regulates patterning in the mouse embryo through inhibition of Hedgehog signaling. *Hum. Mol. Genet.* **18**, 1740–1754 (2009).

81. Tschaikner, P., Enzler, F., Torres-Quesada, O., Aanstad, P. & Stefan, E. Hedgehog and Gpr161: Regulating cAMP Signaling in the Primary Cilium. *Cells* **9**, 1–14 (2020).

82. Liem, K. F. *et al.* The IFT-A complex regulates Shh signaling through cilia structure and membrane protein trafficking. *J. Cell Biol.* **197**, 789–800 (2012).

83. Shantanam, S. & MUELLER. Gpr161 anchoring of PKA consolidates GPCR and cAMP signaling. *Physiol. Behav.* **176**, 139–148 (2018).

84. Bachmann, V. A. *et al.* Gpr161 anchoring of PKA consolidates GPCR and cAMP signaling. *Proc. Natl. Acad. Sci. U. S. A.* **113**, 7786–7791 (2016).

85. Zhang, H., Kong, Q., Wang, J., Jiang, Y. & Hua, H. Complex roles of cAMP–PKA–CREB signaling in cancer. *Exp. Hematol. Oncol.* **9**, 1–13 (2020).

86. Kim, Y. *et al.* WDR11-mediated Hedgehog signalling defects underlie a new ciliopathy related to Kallmann syndrome. *EMBO Rep.* **19**, 269–289 (2018).

87. Carballo, G. B., Honorato, J. R., De Lopes, G. P. F. & Spohr, T. C. L. D. S. E. A highlight on Sonic hedgehog pathway. *Cell Commun. Signal.* **16**, 1–15 (2018).

88. Bacino, C. A., Dhar, S. U., Brunetti-pierri, N., Lee, B. & Bonnen, P. E. Ciliopathy With Variable Phenotype. **0**, 2917–2924 (2014).

89. Khan, A. O., Bolz, H. J. & Bergmann, C. Early-onset severe retinal dystrophy as the initial presentation of IFT140-related skeletal ciliopathy. *J. AAPOS* **18**, 203–205 (2014).

90. Pearlman, J. T., Flood, T. P. & Seiff, S. R. Retinitis pigmentosa without pigment. *Am. J. Ophthalmol.* **81**, 417–419 (1976).

91. den Hollander, A. I., Roepman, R., Koenekoop, R. K. & Cremers, F. P. M. Leber congenital amaurosis: Genes, proteins and disease mechanisms. *Prog. Retin. Eye Res.* **27**, 391–419 (2008).

92. Den Hollander, A. I. *et al.* Mutations in LCA5, encoding the ciliary protein lebercilin, cause Leber congenital amaurosis. *Nat. Genet.* **39**, 889–895 (2007).

93. Schmidts, M. *et al.* Combined NGS Approaches Identify Mutations in the Intraflagellar Transport Gene IFT140 in Skeletal Ciliopathies with Early Progressive Kidney Disease. *Hum. Mutat.* **34**, 714–724 (2013).

94. Miller, K. A. *et al.* Cauli: A Mouse Strain with an Ift140 Mutation That Results in a Skeletal Ciliopathy Modelling Jeune Syndrome. *PLoS Genet.* **9**, (2013).

95. Smith, C. *et al.* A relatively mild skeletal ciliopathy phenotype consistent with cranioectodermal dysplasia is associated with a homozygous nonsynonymous mutation in WDR35. *Am. J. Med. Genet. Part A* **170**, 760–765 (2016).

96. Hoffer, J., Fryssira, H., Konstantinidou, A., Ropers, H. H. & Tzschach, A. Novel WDR35 mutations in patients with cranioectodermal dysplasia (Sensenbrenner syndrome). *Clin. Genet.* **83**, 92–95 (2013).

97. Walczak-Sztulpa, J. *et al.* Intrafamilial phenotypic variability in a Polish family with Sensenbrenner syndrome and biallelic WDR35 mutations. *Am. J. Med. Genet. Part A* **173**, 1364–1368 (2017).

98. Eggenschwiler, J. T. & Anderson, K. V. Cilia and developmental signaling. *Annu. Rev. Cell Dev. Biol.* **23**, 345–373 (2007).

99. Saxton, R. A. & Sabatini, D. M. mTOR Signaling in Growth, Metabolism, and Disease. *Cell* **169**, 361–371 (2017).

100. Cox, J. & Mann, M. MaxQuant enables high peptide identification rates, individualized p.p.b.-range mass accuracies and proteome-wide protein quantification. *Nat. Biotechnol.* **26**, 1367–1372 (2008).

101. Gloeckner, C. J., Boldt, K. & Ueffing, M. Strep/FLAG tandem affinity purification (SF-TAP) to study protein interactions. *Curr. Protoc. Protein Sci.* 1–19 (2009) doi:10.1002/0471140864.ps1920s57.

102. Suzuki, Y. *et al.* A novel high-throughput (HTP) cloning strategy for site-directed designed chimeragenesis and mutation using the Gateway cloning system. *Nucleic Acids Res.* **33**, 1–6 (2005).

103. Zhang, C., Quan, R. & Wang, J. Development and application of CRISPR/Cas9 technologies in genomic editing. *Hum. Mol. Genet.* **27**, R79–R88 (2018).

104. Noor, Z., Ahn, S. B., Baker, M. S., Ranganathan, S. & Mohamedali, A. Mass spectrometry-based protein identification in proteomics- A review. *Brief. Bioinform.* **22**, 1620–1638 (2021).

105. Tsiatsiani, L. & Heck, A. J. R. Proteomics beyond trypsin. *FEBS J.* **282**, 2612–2626 (2015).

106. Aebersold, B. D. and R. Mass Spectrometry and Protein Analysis. **312**, 212–217 (2006).

107. Duran, I. *et al.* Mutations in IFT-A satellite core component genes IFT43 and IFT121 produce short rib polydactyly syndrome with distinctive campomelia. *Cilia* **6**, 1–13 (2017).

108. Chen, D. *et al.* EML4 promotes the loading of NUDC to the spindle for mitotic progression. *Cell Cycle* **14**, 1529–1539 (2015).

109. Sun, J., Sun, Y., Ahmed, R. I., Ren, A. & Xie, M. Research progress on plant RING-finger proteins. *Genes (Basel).* **10**, (2019).

110. Krishna, S. S., Majumdar, I. & Grishin, N. V. Structural classification of zinc fingers. *Nucleic Acids Res.* **31**, 532–550 (2003).

111. Miyamoto, K., Uechi, A. & Saito, K. The zinc finger domain of RING finger protein 141 reveals a unique RING fold. *Protein Sci.* **26**, 1681–1686 (2017).

112. Boldt, K. *et al.* An organelle-specific protein landscape identifies novel diseases and molecular mechanisms. *Nat. Commun.* **7**, 1–13 (2016).

113. Rushworth, L. K. *et al.* In vivo CRISPR/Cas9 knockout screen: TCEAL1 silencing enhances docetaxel efficacy in prostate cancer. *Life Sci. Alliance* **3**, 1–14 (2020).

114. Song, Y. *et al.* SYPL1 Inhibits Apoptosis in Pancreatic Ductal Adenocarcinoma via Suppression of ROS-Induced ERK Activation. *Front. Oncol.* **10**, 1–13 (2020).

115. Rani, M. R. S. *et al.* Catalytically active TYK2 is essential for interferon-β-mediated phosphorylation of STAT3 and interferon-α receptor-1 (IFNAR-1) but not for activation of phosphoinositol 3-kinase. *J. Biol. Chem.* **274**, 32507–32511 (1999).

116. Jonik-Nowak, B. *et al.* PIP30/FAM192A is a novel regulator of the nuclear proteasome activator PA28γ. *Proc. Natl. Acad. Sci. U. S. A.* **115**, E6477–E6486 (2018).

117. Harper, S. *et al.* Structure and catalytic regulatory function of ubiquitin specific protease 11 N-terminal and ubiquitin-like domains. *Biochemistry* **53**, 2966–2978 (2014).

118. Debra Abramov, Noah Guy Lewis Guiberson, J. B. STXBP1 encephalopathies: Clinical spectrum, disease mechanisms, and therapeutic strategies. *Physiol. Behav.* **176**, 139–148 (2018).

119. Gupta, I. R. *et al.* ARHGDIA: A novel gene implicated in nephrotic syndrome. *J. Med. Genet.* **50**, 330–338 (2013).

120. Barker, P. A. & Salehi, A. The MAGE proteins: Emerging roles in cell cycle progression, apoptosis, and neurogenetic disease. *J. Neurosci. Res.* **67**, 705–712 (2002).

121. Panvert, M. *et al.* Cdc123, a Cell Cycle Regulator Needed for eIF2 Assembly, Is an ATP-Grasp Protein with Unique Features. *Structure* **23**, 1596–1608 (2015).

122. Bergemann, A. D., Ma, Z. W. & Johnson, E. M. Sequence of cDNA comprising the human pur gene and sequence-specific single-stranded-DNA-binding properties of the encoded protein. *Mol. Cell. Biol.* **12**, 5673–5682 (1992).

123. Schrank, B. R. *et al.* Nuclear Arp2/3 drives DNA break clustering for homologydirected repair. **559**, 61–66 (2018).

124. Liu, R. *et al.* Choline kinase alpha 2 acts as a protein kinase to promote lipolysis of lipid droplets. *Mol. Cell* **81**, 2722-2735.e9 (2021).

125. Perrin, J. *et al.* TM9 family proteins control surface targeting of glycine-rich transmembrane domains. *J. Cell Sci.* **128**, 2269–2277 (2015).

126. Zhang, J. *et al.* Cloning and functional characterization of GMPR2, a novel human guanosine monophosphate reductase, which promotes the monocytic differentiation of HL-60 leukemia cells. *J. Cancer Res. Clin. Oncol.* **129**, 76–83 (2003).

127. Vukojevic, V. *et al.* Evolutionary conserved role of neural cell adhesion molecule-1 in memory. *Transl. Psychiatry* **10**, (2020).

128. Huber, M. D., Vesely, P. W., Datta, K. & Gerace, L. Erlins restrict SREBP activation in the ER and regulate cellular cholesterol homeostasis. *J. Cell Biol.* **203**, 427–436 (2013).

129. Little, G. H., Bai, Y., Williams, T. & Poizat, C. Nuclear calcium/calmodulin-dependent protein kinase IIδ preferentially transmits signals to histone deacetylase 4 in cardiac cells. *J. Biol. Chem.* **282**, 7219–7231 (2007).

130. Bai, M. *et al.* Conserved roles of C. elegans and human MANFs in sulfatide binding and cytoprotection. *Nat. Commun.* **9**, 1–11 (2018).

131. Aumais, J. P. *et al.* Role of NudC, a dynein-associated nuclear movement protein, in mitosis and cytokinesis. *J. Cell Sci.* **116**, 1991–2003 (2003).

132. Zheng, M. *et al.* Structural features and chaperone activity of the NudC protein family. **409**, 722–741 (2012).

133. Otta, H. *et al.* The chaperones MPP11 and Hsp70L1 form the mammalian ribosome-associated complex. *Proc. Natl. Acad. Sci. U. S. A.* **102**, 10064–10069 (2005).

134. Crevel, G., Bennett, D. & Cotterill, S. The human TPR protein TTC4 is a putative Hsp90 co-chaperone which interacts with CDC6 and shows alterations in transformed cells. *PLoS One* **3**, 1–10 (2008).

135. Slomovic, S., Fremder, E., Staals, R. H. G., Pruijn, G. J. M. & Schuster, G. Addition of poly(A) and poly(A)-rich tails during RNA degradation in the cytoplasm of human cells. *Proc. Natl. Acad. Sci. U. S. A.* **107**, 7407–7412 (2010).

136. Radons, J. The human HSP70 family of chaperones: where do we stand? *Cell Stress Chaperones* **21**, 379–404 (2016).

137. Arakawa, A. *et al.* The C-Terminal BAG Domain of BAG5 Induces Conformational Changes of the Hsp70 Nucleotide- Binding Domain for ADP-ATP Exchange. *Structure* **18**, 309–319 (2010).

138. Yan Chen, Jin-Yi Zhu, Kwon Ho Hong, David C. Mikles, Gunda I. Georg, A. S. & Goldstein, John K Amory, Schönbrunn, and E. Structural Basis of ALDH1A2 Inhibition by Irreversible and Reversible Small Molecule Inhibitors. *Physiol. Behav.* **176**, 139–148 (2018).

139. Zou, Z., Tao, T., Li, H. & Zhu, X. MTOR signaling pathway and mTOR inhibitors in cancer: Progress and challenges. *Cell Biosci.* **10**, 1–11 (2020).

140. Hackam, A. S. The Wnt signaling pathway in retinal degenerations. *IUBMB Life* **57**, 381–388 (2005).

141. Balmer, S. *et al.* Components of Intraflagellar Transport complex A (IFT-A) function independently of the cilium to regulate canonical Wnt signaling in Drosophila. **34**, 705–718 (2016).

142. Thompson, B. A., Tremblay, V., Lin, G. & Bochar, D. A. CHD8 Is an ATP-Dependent Chromatin Remodeling Factor That Regulates β-Catenin Target Genes. *Mol. Cell. Biol.* **28**, 3894–3904 (2008).

143. Van Bergen, N. J. *et al.* Mutations in the exocyst component EXOC2 cause severe defects in human brain development. *J. Exp. Med.* **217**, 1–20 (2020).

144. Watabe-Uchida, M., John, K. A., Janas, J. A., Newey, S. E. & Van Aelst, L. The Rac Activator DOCK7 Regulates Neuronal Polarity through Local Phosphorylation of Stathmin/Op18. *Neuron* **51**, 727–739 (2006).

145. Sbrissa, D. *et al.* Core protein machinery for mammalian phosphatidylinositol 3,5-bisphosphate synthesis and turnover that regulates the progression of endosomal transport: Novel Sac phosphatase joins the ArPIKfyve-PIKfyve complex. *J. Biol. Chem.* **282**, 23878–23891 (2007).

146. Toriyama, M. *et al.* Shootin 1: A protein involved in the organization of an asymmetric signal for neuronal polarization. *J. Cell Biol.* **175**, 147–157 (2006).

147. Radmanesh, F. *et al.* Mutations in LAMB1 cause cobblestone brain malformation without muscular or ocular abnormalities. *Am. J. Hum. Genet.* **92**, 468–474 (2013).

148. Lai Xu, Mathew E. Sowa, Jing Chen, Xue Li, S. P. G. & Harper, and J. W. An FTS/Hook/p107FHIP Complex Interacts with and Promotes Endosomal Clustering by the Homotypic Vacuolar Protein Sorting Complex. *Mol. Biol. Cell* **20**, 2673–2683 (2009).

149. Hsueh, Y. S. *et al.* Nuclear KIT induces a NFKBIB-RELA-KIT autoregulatory loop in imatinib-resistant gastrointestinal stromal tumors. *Oncogene* **38**, 6550–6565 (2019).

150. Liu, T. *et al.* Phosphorylation of right open reading frame 2 (Rio2) protein kinase by polo-like kinase 1 regulates mitotic progression. *J. Biol. Chem.* **286**, 36352–36360 (2011).

151. Julian C. Lui, Youn Hee Jee, Audrey Lee, Shanna Yue, Jacob Wagner, D. E. & Donnelly, Karen S. Vogt, and J. B. QRICH1 Mutations cause a Chondrodysplasia with Developmental Delay. *J. Int. Soc. Burn Inj.* **43**, 909–932 (2017).

152. Breuss, M. W. *et al.* Mutations in LNPK, Encoding the Endoplasmic Reticulum Junction Stabilizer Lunapark, Cause a Recessive Neurodevelopmental Syndrome. *Am. J. Hum. Genet.* **103**, 296–304 (2018).

153. Coon, B. G. *et al.* The lowe syndrome protein OCRL1 is involved in primary cilia assembly. *Hum. Mol. Genet.* **21**, 1835–1847 (2012).

154. Moosa, S. *et al.* Novel IFT122 mutations in three Argentinian patients with cranioectodermal dysplasia: Expanding the mutational spectrum. *Am. J. Med. Genet. Part A* **170**, 1295–1301 (2016).

155. Tsurusakia, Y., Yonezawab, R., Furuyac, M., Nishimurad, G., Poohe, R. K., Nakashimaa, M., Saitsua, H., Miyakea, N., Saitob, S., N. M. Whole exome sequencing revealed biallelic IFT122 mutations in a family with CED1 and recurrent pregnancy loss. 592–594 (2014) doi:10.1111/cge.12215.

156. Chuang, Y. *et al.* Regulation of synaptojanin 2 5'-phosphatase activity by Src. *Cell Adhes. Migr.* **6**, 518–525 (2012).

157. Yanguas, F. & Valdivieso, M. H. *Analysis of the SNARE Stx8 recycling reveals that the retromer-sorting motif has undergone evolutionary divergence*. *PLoS Genetics* vol. 17 (2021).

158. Jin, X. *et al.* SMG9 Serves as an Oncogene to Promote the Tumor Progression via EMT and Wnt/β-Catenin Signaling Pathway in Hepatocellular Carcinoma. *Front. Pharmacol.* **12**, 1–14 (2021).

159. Wiche, G. Role of plectin in cytoskeleton organization and dynamics. *J. Cell Sci.* **111**, 2477–2486 (1998).

160. Starokadomskyy, P. *et al.* DNA polymerase-alpha regulates type I interferon activation through cytosolic RNA:DNA synthesis. *Nat Immunol.* **17(5)**, 495–504 (2016).

161. Biebl, M. M. *et al.* NudC guides client transfer between the Hsp40/70 and Hsp90 chaperone systems. *Mol. Cell* **82**, 555-569.e7 (2022).

162. Khan, A. O., Bolz, H. J. & Bergmann, C. Early-onset severe retinal dystrophy as the initial presentation of IFT140-related skeletal ciliopathy. *J. AAPOS* **18**, (2014).

163. Xu, M. *et al.* Mutations in human IFT140 cause non-syndromic retinal degeneration. *Hum. Genet.* **134**, 1069–1078 (2015).

164. Hoffmann, F. *et al.* TTC30A and TTC30B Redundancy Protects IFT Complex B Integrity and Its Pivotal Role in Ciliogenesis. *Genes (Basel).* **13**, (2022).

165. Cameron, D. A., Pennimpede, T. & Petkovich, M. Tulp3 is a critical repressor of Mouse hedgehog signaling. *Dev. Dyn.* **238**, 1140–1149 (2009).

166. Kobayashi, T., Ishida, Y., Hirano, T., Katoh, Y. & Nakayama, K. Cooperation of the IFT-A complex with the IFT-B complex is required for ciliary retrograde protein trafficking and GPCR import. *Mol. Biol. Cell* **32**, 45–56 (2021).

167. Jordan, M. A., Diener, D. R., Stepanek, L. & Pigino, G. The cryo-EM structure of intraflagellar transport trains reveals how dynein is inactivated to ensure unidirectional anterograde movement in cilia. *Nat. Cell Biol.* **20**, 1250–1255 (2018).

168. Ocbina, P. J. R., Tuson, M. & Anderson, K. V. Primary cilia are not required for normal canonical Wnt signaling in the mouse embryo. *PLoS One* **4**, 1–8 (2009).

169. Scholey, J. M. & Anderson, K. V. Intraflagellar Transport and Cilium-Based Signaling. *Cell* **125**, 439–442 (2006).

170. Sugiyama, N., Tsukiyama, T., Yamaguchi, T. P. & Yokoyama, T. The canonical Wnt signaling pathway is not involved in renal cyst development in the kidneys of inv mutant mice. *Kidney Int.* **79**, 957–965 (2011).

171. Huang, P. & Schier, A. F. Dampened Hedgehog signaling but normal Wnt signaling in zebrafish without cilia. *Development* **136**, 3089–3098 (2009).

172. Lee, K. H. Involvement of Wnt signaling in primary cilia assembly and disassembly. *FEBS J.* **287**, 5027–5038 (2020).

173. Simons, M. *et al.* Inversin, the gene product mutated in nephronophthisis type II, functions as a molecular switch between Wnt signaling pathways. *Nat. Genet.* **37**, 537–543 (2005).

174. Wheway, G. *et al.* An siRNA-based functional genomics screen for the identification of regulators of ciliogenesis and ciliopathy genes. *Nat. Cell Biol.* **17**, 1074–1087 (2015).

175. Lin, F. *et al.* Kidney-specific inactivation of the KIF3A subunit of kinesin-II inhibits renal ciliogenesis and produces polycystic kidney disease. *Proc. Natl. Acad. Sci. U. S. A.* **100**, 5286–5291 (2003).

176. Jones, C. *et al.* Ciliary proteins link basal body polarization to planar cell polarity regulation. *Nat. Genet.* **40**, 69–77 (2008).

177. Carvajal-Gonzalez, J. M., Roman, A. C. & Mlodzik, M. Positioning of centrioles is a conserved readout of Frizzled planar cell polarity signalling. *Nat. Commun.* **7**, (2016).

178. Gómez-Orte, E., Sáenz-Narciso, B., Moreno, S. & Cabello, J. Multiple functions of the noncanonical Wnt pathway. *Trends Genet.* **29**, 545–553 (2013).

179. Beyer, T. *et al.* CRISPR/Cas9-mediated genomic editing of Cluap1/IFT38 reveals a new role in actin arrangement. *Mol. Cell. Proteomics* **17**, 1285–1294 (2018).

180. Rassoolzadeh, H. *et al.* Overexpression of the scaffold WD40 protein WRAP53B enhances the repair of and cell survival from DNA double-strand breaks. *Cell Death Dis.* **7**, 1–9 (2016).

181. Jain, B. P. & Pandey, S. WD40 Repeat Proteins: Signalling Scaffold with Diverse Functions. *Protein J.* **37**, 391–406 (2018).

182. Jiang, M. *et al.* Human IFT-A complex structures provide molecular insights into ciliary transport. 1–11 (2023) doi:10.1038/s41422-023-00778-3.

183. Lambert, J. P., Tucholska, M., Go, C., Knight, J. D. R. & Gingras, A. C. Proximity biotinylation and affinity purification are complementary approaches for the interactome mapping of chromatin-associated protein complexes. *J. Proteomics* **118**, 81–94 (2015).

184. Gerace, E. & Moazed, D. Affinity Pull-Down of Proteins Using Anti-FLAG M2 Agarose Beads. *Methods Enzymol.* **559**, 99–110 (2015).

185. Pazour, G. J., Wilkerson, C. G. & Witman, G. B. A dynein light chain is essential for the retrograde particle movement of intraflagellar transport (IFT). *J. Cell Biol.* **141**, 979–992 (1998).

186. Del-Toro, N. *et al.* Capturing variation impact on molecular interactions in the IMEx Consortium mutations data set. *Nat. Commun.* **10**, 1–14 (2019).

187. Jayasena, T. *et al.* Application of Targeted Mass Spectrometry for the Quantification of Sirtuins in the Central Nervous System. *Sci. Rep.* **6**, 1–11 (2016).

188. Han, S. *et al.* TULP3 is required for localization of membrane-associated proteins ARL13B and INPP5E to primary cilia. *Biochem. Biophys. Res. Commun.* **509**, 227–234 (2019).

189. Lai, C. K. *et al.* Functional characterization of putative cilia genes by high-content analysis. *Mol. Biol. Cell* **22**, 1104–1119 (2011).

190. Yampolsky, L. Y. & Stoltzfus, A. The exchangeability of amino acids in proteins. *Genetics* **170**, 1459–1472 (2005).

191. Galvin, J. A., Fishman, G. A., Stone, E. M. & Koenekoop, R. K. Clinical phenotypes in carriers of Leber congenital amaurosis mutations. *Ophthalmology* **112**, 349–356 (2005).

192. Hua, K. & Ferland, R. J. Fixation methods can differentially affect ciliary protein immunolabeling. *Cilia* **6**, 1–17 (2017).

193. Forcioli-Conti, N., Estève, D., Bouloumié, A., Dani, C. & Peraldi, P. The size of the primary cilium and acetylated tubulin are modulated during adipocyte differentiation: Analysis of HDAC6 functions in these processes. *Biochimie* **124**, 112–123 (2016).

194. Mujić, M. Bosnian journal of basic medical sciences. Editorial. *Bosn. J. Basic Med. Sci.* **9**, 173 (2009).

195. Tran, P. V. *et al.* THM1 negatively modulates mouse sonic hedgehog signal transduction and affects retrograde intraflagellar transport in cilia. *Nat. Genet.* **40**, 403–410 (2008).

Appendix

MaxQuant parameters for label-free quanitfication

Parameter	Value
Version	1.6.1.0
Fixed modifications	Carbamidomethyl (C)
Include contaminants	True
PSM FDR	0.01
XPSM FDR	0.01
Protein FDR	0.01
Site FDR	0.01
Use Normalized Ratios For Occupancy	True
Min. peptide Length	7
Min. score for unmodified peptides	0
Min. score for modified peptides	40
Min. delta score for unmodified peptides	0
Min. delta score for modified peptides	6
Min. unique peptides	1
Min. razor peptides	2
Min. peptides	2
Use only unmodified peptides and	False
Peptides used for protein quantification	Razor
Discard unmodified counterpart peptides	True
Label min. ratio count	2
Use delta score	False
iBAQ	False
iBAQ log fit	False
Match between runs	True
Matching time window [min]	0.7
Alignment time window [min]	20
Find dependent peptides	False
Decoy mode	revert
Include contaminants	True
Advanced ratios	True
Second peptides	False
Stabilize large LFQ ratios	True
Separate LFQ in parameter groups	False
Require MS/MS for LFQ comparisons	False
Calculate peak properties	False
Main search max. combinations	200
Advanced site intensities	True
LFQ norm for sites and peptides	False
Write msScans table	True
Write msmsScans table	True
Write ms3Scans table	False
Write allPeptides table	True
Write mzRange table	False

Write pasefMsmsScans table	False
Write accumulatedPasefMsmsScans table	False
Max. peptide mass [Da]	4600
Min. peptide length for unspecific search	8
Max. peptide length for unspecific search	25
Razor protein FDR	True
Disable MD5	True
Max mods in site table	3
Match unidentified features	True
MS/MS tol. (FTMS)	20 ppm
Top MS/MS peaks per Da interval. (FTMS)	12
Da interval. (FTMS)	100
MS/MS deisotoping (FTMS)	True
MS/MS deisotoping tolerance (FTMS)	7
MS/MS deisotoping tolerance unit (FTMS)	ppm
MS/MS higher charges (FTMS)	True
MS/MS water loss (FTMS)	True
MS/MS ammonia loss (FTMS)	True
MS/MS dependent losses (FTMS)	True
MS/MS recalibration (FTMS)	False
MS/MS tol. (ITMS)	0.5 Da
Top MS/MS peaks per Da interval. (ITMS)	8
Da interval. (ITMS)	100
MS/MS deisotoping (ITMS)	False
MS/MS deisotoping tolerance (ITMS)	0.15
MS/MS deisotoping tolerance unit (ITMS)	Da
MS/MS higher charges (ITMS)	True
MS/MS water loss (ITMS)	True
MS/MS ammonia loss (ITMS)	True
MS/MS dependent losses (ITMS)	True
MS/MS recalibration (ITMS)	False
MS/MS tol. (TOF)	40 ppm
Top MS/MS peaks per Da interval. (TOF)	10
Da interval. (TOF)	100
MS/MS deisotoping (TOF)	True
MS/MS deisotoping tolerance (TOF)	0.01
MS/MS deisotoping tolerance unit (TOF)	Da
MS/MS higher charges (TOF)	True
MS/MS water loss (TOF)	True
MS/MS ammonia loss (TOF)	True
MS/MS dependent losses (TOF)	True
MS/MS recalibration (TOF)	False
MS/MS tol. (Unknown)	0.5 Da
Top MS/MS peaks per Da interval. (Unknown)	8
Da interval. (Unknown)	100
MS/MS deisotoping (Unknown)	False

MS/MS deisotoping tolerance (Unknown)	0.15
MS/MS deisotoping tolerance unit (Unknown)	Da
MS/MS higher charges (Unknown)	True
MS/MS water loss (Unknown)	True
MS/MS ammonia loss (Unknown)	True
MS/MS dependent losses (Unknown)	True
MS/MS recalibration (Unknown)	False

Log_2 ratios (mutant/wildtype) from labelfree quantification for missense mutations in IFT43

Mutation in IFT43

Gene name	W179R
IFT43	0.80
IFT144	-3.54
IFT140	-2.71
IFT122	-3.37
IFT121	-4.26
IFT139	-3.20
DCTN5	-0.09
PIP30	0.18
STXBP1	1.61
SYPL1	0.28
TCEAL1	-0.73
TULP3	-26.81
TYK2	-0.16
USP11	-0.44

Log_2 ratios (mutant/wildtype) from labelfree quantification for missense mutations in IFT121

Gene name	Mutation in IFT121			
	S168R	**D841V**	**Y971C***	**W1153C***
IFT121	-1.79	-3.11	-1.13	-1.36
IFT139	-4.41	-7.21	-3.36	-2.58
IFT43	-4.05	-6.87	-2.05	-1.99
IFT122	-25.29	-25.29	-4.46	-2.99
IFT140	-5.59	-25.46	-5.18	-3.57
IFT144	-2.59	-5.39	-24.89	-4.06
ARHGDIA	-0.02	-0.01	0.06	-0.24
ARPC5	0.27	0.14	-20.38	0.14
CAMK2D	-0.26	-19.06	-19.06	-19.06
CDC123	-20.95	-20.95	-20.95	-1.08
ERLIN1	-19.28	-19.28	-19.28	-19.28
GMPR2	-19.36	-0.12	-0.14	0.26
MAGED1	-1.20	-1.65	-1.02	-21.10
MANF	-19.00	-0.18	-19.00	-19.00
NCAM1	-0.21	-19.31	-19.31	-1.48
NUDC	-0.29	-0.91	-0.30	-0.50
PLIN3	-0.70	-19.77	0.08	-0.03
PURB	-20.82	-20.82	-1.04	-20.82
SMAD3	-21.14	-21.14	-1.56	-1.36
TM9SF3	-19.60	-0.97	-19.60	-0.51

Log_2 ratios (mutant/wildtype) from labelfree quantification for missense mutations in IFT122

Gene name	Mutation in IFT122							
	W7C	**S373F***	**V442L**	**G546R**	**V553G***	**F621C**	**G623V***	**L763P**
IFT122	1.30	-3.32	-0.03	-0.33	-0.17	-3.92	0.93	-0.01
IFT140	2.43	-4.14	2.01	-0.13	2.12	-27.03	2.05	-1.02
IFT144	2.56	-3.90	2.53	0.01	1.56	-27.73	2.16	-0.32
IFT139	-2.12	-8.79	-6.45	-6.20	-5.13	-7.27	-5.00	-2.61
IFT121	-0.86	-10.93	-9.41	-8.51	-7.66	-31.01	-7.14	-2.85
IFT43	-1.06	-28.81	-8.43	-9.44	-6.84	-28.81	-5.68	-2.91
IFT27	-24.00	0.14	-0.16	-0.35	-0.36	-0.56	-0.24	-0.31
CTNNB1	-22.96	-0.30	-1.22	-1.35	-0.59	-22.96	-0.20	-22.96
CHD8	-0.78	0.10	-1.09	-0.05	0.24	-0.02	-1.38	0.26
NCAM1	-0.42	-0.22	-23.77	-0.71	-0.82	0.03	-0.52	-0.19
RALDH2	-0.19	-1.01	-24.13	-24.13	-24.13	0.29	-0.30	0.15
MTOR	-0.02	-0.29	0.03	0.15	0.08	-23.83	0.15	-1.24
EXOC2	0.18	-0.50	-0.14	-0.01	-0.40	-0.07	-1.70	0.12
EXOC6	2.15	-20.71	-1.15	-20.71	-20.71	1.85	-20.71	1.88
EXOC8	0.17	-0.20	-0.11	-0.12	-1.36	-0.90	-0.11	-22.50
STXBP3	-22.66	-0.19	-0.09	-0.03	-0.03	0.08	0.22	0.23
VAC14	-23.10	-23.10	-23.10	-23.10	-23.10	-23.10	-23.10	-23.10
DOCK7	-1.12	-23.45	0.33	0.07	-1.11	0.23	-0.12	0.19
HSPA14	-1.50	-0.36	-0.38	-0.20	-0.39	-24.21	-0.42	-0.21
HSPA2	1.74	-23.00	-23.00	-23.00	-23.00	-23.00	0.23	0.90
BAG5	1.12	-1.99	-0.76	-0.28	-0.70	-2.52	0.44	0.16
TTC4	0.55	-0.30	-0.13	0.29	0.27	-24.01	0.63	-0.16
SKI6	-23.04	0.32	0.29	0.31	0.37	0.59	-0.05	0.02
NUDC	1.38	0.22	0.43	0.71	1.26	-2.39	1.47	0.02
RIOK2	-23.13	-23.13	-23.13	-1.16	-0.30	-23.13	0.21	-1.00
SHTN1	-0.11	0.04	0.07	-0.11	-0.17	0.54	0.05	-0.02
NFKBIB	-23.42	0.11	0.06	0.10	0.20	-23.42	-0.04	-1.68
LNP	-22.76	-1.64	-0.52	-22.76	-0.91	0.06	-1.60	0.21
LAMB1	-23.78	-1.94	-23.78	-0.82	-1.03	-23.78	-23.78	-23.78
MRT3	-0.02	0.00	-0.47	-0.57	-0.12	0.05	-0.02	0.03
OCRL	-21.94	0.57	-21.94	-21.94	-21.94	0.29	-2.28	-21.94
WDR11	-22.51	-0.03	0.36	0.09	0.29	-22.51	0.32	-22.51
WDR44	-22.60	0.26	0.11	-1.10	-22.60	0.82	-0.26	-22.60
HOOK1	0.08	-0.51	-2.27	-1.03	-0.54	0.42	-0.20	0.15
IRTKS	-23.24	-23.24	-1.61	-23.24	-2.80	-23.24	-1.16	-0.95
QRICH1	-0.19	-0.20	0.02	0.18	0.27	0.07	0.06	0.33

Log_2 ratios (mutant/wildtype) from labelfree quantification for missense mutations in IFT140

	Gene name														
	IFT140	**IFT122**	**IFT144**	**IFT121**	**IFT139**	**IFT43**	**WDR33**	**TULP3**	**SYNJ2**	**NUDC**	**PLEC**	**POLA1**	**STX8**	**SMG9**	**SPAG7**
P71L	0.12	1.57	1.52	1.79	1.53	1.61	NA	NA	-26	-0.5	23.2	1.22	NA	NA	NA
V108M	-0.8	-3.1	-2.9	-3.1	-3.1	-2.5	-1.2	-23	-0.5	1.2	-0.2	-0.2	0.21	-0.1	-0.2
G140R	-0.4	-2.4	-2.4	-2.5	-2.5	-2.1	-1	-23	-0.7	1	-0.6	-0.7	0.4	-0.5	0.2
G212R	1.52	0.3	0.28	-0.2	-0	-0.1	0.7	0.5	1.1	1.36	-0.7	-0.4	NA	0.1	-0.1
I233M*	-1.5	-1.3	-1.2	-1.5	-1.3	-1.3	NA	NA	NA	0.07	-0.7	-0.6	-0	-24	NA
E267G	0.01	-0.3	-0.3	-0.4	-0.3	-0.1	-0	-23	-0.1	0.56	-0.4	-0	NA	-0.2	-1.1
V292M	0.76	-1.1	-1	-1.3	-1.1	-1	-1.1	-23	0.87	1.05	-1.2	-0.1	0.95	0.53	0.1
Y311C	2.28	-0.7	-0.6	-0.8	-0.4	-1.4	0.4	0.31	NA	2.09	-1.8	-2.4	-25	-25	NA
C329R	-0.6	-1.2	-1.1	-1.2	-1.2	-0.9	-0.4	-1.1	0.24	0.42	-1.6	0.09	0.99	0.51	0.11
C333Y*	1.71	-0.9	-0.7	-1.1	-0.4	-0.9	-1	-1.1	27.5	1.42	-1.6	-0.6	-25	-1.9	NA
A341T	0.14	-2.1	-2	-2.8	-1.7	-2.1	0.18	-24	NA	0.67	-1.8	-1.5	0.28	-2.2	NA
A418P	-0.9	2.42	2.73	3.87	2.87	3.11	NA	NA	NA	-0.9	3.68	1.43	NA	NA	NA
L440P	-0.4	2.76	2.56	4.26	2.89	4.62	NA	NA	NA	-0.8	23.2	1.3	NA	NA	NA
T484M*	0.05	4.1	3.98	5.8	3.64	25.8	NA	NA	NA	-1	23.2	0.98	NA	NA	NA
G522E	0.89	-6.1	-5.6	-5.9	-4.4	-27	NA	NA	27.7	0.56	-4.1	-1	-1	-1.4	NA
E664K*	-0.6	-6.5	-5.2	-29	-5.5	-27	1.39	NA	NA	-0.6	-0.9	-2.1	NA	NA	NA
C663W	1.61	-2.8	-3.6	-4.3	-2.1	-26	0.44	-24	28	1.59	-2.3	-1.4	-2.7	-25	NA
E790K	2.93	1.26	1.15	1.28	1.27	1.66	NA	NA	NA	0.85	0.13	-1.1	-25	NA	-24
R871C	-1.3	-2	-2.1	-2.4	-1.8	-1.7	0.64	NA	NA	-0.4	-1.2	-1.9	NA	NA	NA
S939P	0.3	-1.3	-1	-1.6	-1.6	-1	0.02	-23	-0	-0	-0.8	-0.9	0.25	-0.3	0.03
A974V	1.25	-0.4	-0.5	-0.9	-0.4	-1.1	NA	NA	25.6	0.62	-1.4	-1.1	-25	-24	NA
E1065K	2.88	0.83	0.78	1.04	0.61	1.86	NA	NA	NA	0.46	-0.4	-1.7	-25	NA	-1.9
C1360R	0.21	1.42	1.26	1.42	1.27	1.57	NA	NA	NA	-0	23.2	1.38	NA	NA	NA
L1399P	-3.8	-5.8	-5.5	-4.4	-4.3	-27	NA	NA	NA	-0.2	-0.5	-0.4	-0.9	-0.1	1.39